DOE/ET-0065/3

RECEIVED
D. G. DORAN
MAR 18 '80
File
Action
Return To
Circulate/Xerox to

Damage Analysis and Fundamantal Studies

Quarterly Progress Report
January-March. 1978

May 1979

U.S. Department of Energy
Assistant Secretary for Energy Technology
Office of Fusion Energy

DOE/ET-0065/3
uc-20. 20c

Damage Analysis and Fundamantal Studies

Quarterly Progress Report
January-March, 1978

May 1979

U.S. Department of Energy
Assistant Secretary for Energy Technology
Office of Fusion Energy
Washington, DC 20545

Available from:

National Technical Information Service (NTIS)
U.S. Departwnt of Commerce
5285 Port Royal Road
Springfield, Virginia 22161

Price: Printed Copy: $ 9.50
Microfiche: $ 3.00

FOREWORD

This report is the third in a series of Quarterly Technical Progress Reports on *"Damage Analysis and Fundamental Studies"* (DAFS) which is one element of the Fusion Reactor Materials Program, conducted in support of the Magnetic Fusion Energy Program of the U. S. Department of Energy. Other elements of the Materials Program are:

- *Alloy Development for Irradiation Performance (ADIP)*
- *Plasma-Materials Interaction (PMI)*
- *Special Purpose Materials (SPM)*

The DAFS program element *is* a national effort composed of contributions from a number of national laboratories and other government laboratories, universities, and industrial laboratories. It was organized by the Materials and Radiation Effects Branch, Office of Fusion Energy, DOE, and a Task Group on *Damage Analysis and Fundamental Studies* which operates under the auspices of that Branch. The purpose of this series of reports is to provide a working technical record of that effort for the use of the program participants, for the fusion energy program in general, and for the Department of Energy.

This report is organized along topical lines in parallel to Section II, Damage Analysis and Fundamental Studies (DOE/ET-0032/2), of the Fusion Reactor Materials Program Plan so that activities and accomplishments may be followed readily relative to that Program Plan. Thus, the work of a given laboratory may appear throughout the report. Chapters 1 and 2 report topics which are generic to all of the DAFS Program: DAFS Task Group Activities and Irradiation Test Facilities, respectively. Chapters 3, 4, and 5 report the work that is specific to each of the subtasks around which the program is structured: A. Environmental Characterization, B. Damage Production and C. Damage Microstructure Evolution and Mechanical Behavior. The Table of Contents is annotated for the convenience *of* the reader.

This report has been compiled and edited under the guidance of the Chairman *of* the Task Group on *Damage Analysis and Fundamental Studies,* D. G. Doran, Hanford Engineering Development Laboratory, and his efforts, those of the supporting staff of HEDL and the many persons who made technical contributions are gratefully acknowledged. T. C. Reuther, Materials and Radiation Effects Branch, is the Department of Energy counterpart to the Task Group Chairman and has responsibility for the DAFS Program within DOE.

Klaus M. Zwilsky, Chief
Materials and Radiation
Effects Branch
Office of Fusion Energy

CONTENTS

	Page
FOREWORD	iii
FIGURES	xi
TABLES	xvii
CHAPTER 1. DAFS TASK GROUP ACTIVITIES	1

Task Group activities included review of plans for neutron field characterization of FMIT, formulation of plans for neutron field characterization of RTNS-11, implementation of the microstructural evolution program, and initiating a fundamental mechanical behavior program. The DAFS Program Plan was published.

CHAPTER 2. IRRADIATION TEST FACILITIES	7

The RTNS-11 Utilization Plan was completed, printed, and is currently being distributed.

CHAPTER 3. SUBTASK A: ENVIRONMENTAL CHARACTERIZATION	11
Experiments at ORR (ANL)	13

The first MFE irradiation in ORR was completed and the second irradiation was started in September. A low power spectral measurement is scheduled for October 1978.

Experiments at U.C. Davis, Be (d,n), E_d = 40 MeV (ANL)	16

Flux-spectra, including uncertainties, are presented for two locations in the E_d = 40 MeV, Be(d,n) field at the U.C. Davis cyclotron.

Helium Analyses of Be(d,n)-Irradiated Pure Elements (RI)	25

Helium analyses have been completed for 23 additional pure element (Al, Fe, Ni, Cu, and Au) helium accumulation dosimetry ring segments irradiated in a Be(d,n) neutron field using 30-MeV deuterons.

CONTENTS (cont'd)

Flux-Spectral Definition in FMIT (BNL) 29

The MORSE transport code was used to calculate the neutron flux distribution in a block of iron irradiated in a high density concrete cave with a Be(d,n) source. The damage energy resulting from primary knock-on atoms of aluminum in Al_2O_3 was calculated.

FMIT Damage Parameter Sensitivity Study (HEDL) 42

The microscopic neutron yield model used in the perturbed and unperturbed flux and spectrum calculations has been improved; as a result, the spatial variations in damage parameters are much greater than those presented previously.

Extrapolation of Damage Cross Sections for Copper (ANL) 48

Displacement cross sections and recoil spectra for copper have been calculated for neutron energies up to 100 MeV for use at Be(d,n) and spallation sources; examples are given for a Be(d,n) irradiation at E_d = 40 MeV and for the expected IPNS-I spectrum.

Boron Doping of Stainless Steel by Rapid Quenching (MIT) 53

Initial microstructural characterization has been performed of a roll-quenched Fe-Ni-Cr alloy.
New flux measurements in the MITR-11 irradiation facility give a peak flux of 5 X 10^{13} n/cm^2-s (E>1 MeV).

Dosimetry Cross Section File (ANL) 65

An ANL report has been written describing 31 activation cross sections extrapolated to 44 MeV for dosimetry at Be(d,n) sources; a summary of integral testing is given.

CHAPTER 4. DAMAGE PRODUCTION 71

Displacement Functions for Multicomponent Systems (LASL, U. of Alabama) 73

The influence of mass difference on the distribution of displacements among atom types is illustrated for TaO.

CONTENTS (cont'd)

Page

A Methodology for the Computer Simulation of Low Energy Radiation Damage Experiments (CSU, HEDL) 77

A methodology is presented for the computer simulation of low energy radiation damage experiments using the quasi-dynamical computer code ADDES.

Tne Application of Dynamical Computer Models to the Simulation of High Energy Cascades (CSU, HEDL) a7

The simulation of high energy displacement cascades is being carried out using the quasi-dynamical code ADDES as a bridge between the dynamical code COMENT and the binary collision code MARLOWE.

CHAPTER 5. SUBTASK C: DAMAGE MICROSTRUCTURE EVOLUTION AND MECHANICAL BEHAVIOR 93

Microstructural Evolution Under Irradiation (UCSB) 97

Progress has been made in developing physical models of microstructural development and property changes under irradiation; some success has been achieved in initial applications to the data base for 300 series stainless steel.

DAFS Test Matrix for the EBR-II Reactor Experiment (NRL, HEDL) 130

Electron microscopy foils of a series of titanium alloys and tensile specimens of a series of iron-nickel-chromium ternary alloys were inserted in an irradiation assembly in the EBR-11 reactor.

Microstructure of Irradiated Fusion Reactor First-Wall Materials (ANL) 137

Single and dual-ion irradiations of Ti-64 resulted in profuse precipitation of 8-platelets and the occurrence of helium induced cavities on grain boundaries.

CONTENTS (cont'd)

Page

Helium Mobility and Distribution (W-R&D) 146

Work was initiated to determine the feasibility of using the $^3He(d,p)\alpha$ nuclear reaction technique to study the effects of momentum transfer, detrapping and radiation-enhanced diffusion of helium in ion-bombarded molybdenum.

In-Situ HVEM Studies of Helium Irradiated Stainless Steel (U. of Virginia) 150

In-situ HVEM observations of helium-ion-irradiated AISI 316 stainless steel showed black spot damage, bubble nucleation and growth, and finally blistering and exfoliation of the surface.

Displacement Damage Studies (PNL) 158

The ratio of the number of Be(d,n) to T(d,n) neutrons to cause a given increase in yield strength in nickel and niobium was found to be one and five, respectively.

In-Reactor Fatique Cracking Experiment (MIT) 163

Detailed design of an in-reactor fatigue cracking experiment is complete and installation begun.

Effects of Bombarding Ions on the Void Swelling Profile in Nickel (U. of Wisconsin) 166

The swelling behavior of high purity nickel bombarded with C and Al ions is similar to that observed with self-ions.

Light Particle Irradiations (W-R&D) 190

Tensile tests of AISI 316 stainless steel are being performed using foils several microns thick for comparison with conventional tests.

Damage Correlation (ANL) 192

Installation and checkout of the torsional-creep apparatus at the ANL Cyclotron is complete; thermal and proton-beam creep data for 20% CW Type 316 stainless steel are reported.

CONTENTS (cont'd)

Effects of Hot Pre-Implantation and Simultaneous Helium Injection on Microstructural Evolution in 316 SS (W-R&D) 197

The mode of heliym injection was shown to influence strongly the nucleation and growth of the damage microstructure in 316 stainless steel irradiated with 28 MeV Si ions.

FIGURES

Page

CHAPTER 3

Experiments at U.C. Davis, Be(d,n), E_d 40 MeV

FIGURE 1. Be(d,n) Spectrum Unfolded at the U.C. Davis Cyclotron for PNL 20

FIGURE 2. Be(d,n) Spectrum Unfolded at the U.C. Davis Cyclotron for PNL 21

FIGURE 3. Radial Activity Map for ^{58}Ni(n,p) Strips Measuring about 1.8 mm Square Cut from Larger Strips about 1.8 mm by 9 mm 22

Flux-Spectral Definition in FMIT

FIGURE 1. Geometry Used for Computing Neutron Spectra within a 30x20x20 cm^3 Test Sample of Iron Located in a 5'x6'x8' Irradiation Cave 38

FIGURE 2. Comparison of Neutron Spectra Obtained from RSIC 100 Group Cross Sections and the Alsmiller and Barish 47 Group Cross Sections 39

FIGURE 3. Comparison of the Uncollided Spectrum with the Total Spectrum at the Point (0, 0, 1) within a 30x20x20 cm^3 Block of Iron Located within an Irradiation Cave Having Walls of High Density Concrete 40

FIGURE 4. Dependence of Damage Energy per Incident Neutron upon the Depth in a 30x20x20 cm^3 Block of Iron Located in an Irradiation Cave Having Walls of High Density Concrete 41

FMIT Damage Parameter Sensitivity Study

FIGURE 1. Calculated Neutron Spectra at Two Positions within the FMIT Irradiation Cell 44

FIGURES (cont'd)

Page

Boron Doping of Stainless Steel by Rapid Quenching

FIGURE 1. Optical Micrograph of Splat Cooled Type 316 Stainless Steel 56

FIGURE 2. Optical Micrograph of Splat Cooled Type 316 Stainless Steel 57

FIGURE 3. Fast Neutron Flux in the CTRF 61

FIGURE 4. 2200 m/s Thermal Neutron Flux in the CTRF 62

CHAPTER 4

A Methodology for the Computer Simulation of Low Energy Radiation Damage Experiments

FIGURE 1. Procedure for Choosing a Potential 81

FIGURE 2. Procedure for Optimizing Parameter Settings 83

CHAPTER 5

Microstructural Evolution Under Irradiation

FIGURE 1. Comparison of Predicted Reductions in Void Nucleation Rates Using Correlation and Numerical Calculations 101

FIGURE 2. Predicted Void Densities from Bubble Nucleation and Growth-Void Formation Model 103

FIGURE 3. Model Prediction-Experiment Comparisons of Swelling Parameters for (a) 304 and (b) Pure 316 Stainless Steels 106

FIGURE 4. Swelling Rate Curves for 316 Stainless Steel from Various References 107

FIGURE 5. Illustrations of MPS Maps 109

FIGURE 6. Predicted (a) Total Dislocation and (b) Faulted Dislocation Loop Densities 113

FIGURES (cont'd)

		Page
FIGURE 7.	Predicted Total Dislocation Density and Swelling for Solution Annealed and Cold-Worked Stainless Steels	114
FIGURE 8.	Illustration of Composite Model Calculation Results	119
FIGURE 9.	Examples of Parametric Models Used in Mechanical Property-Microstructure Correlation Study	122
FIGURE 10.	Model Prediction-Experiment Comparisons for the Yield Stress of Solution Annealed Stainless Steel	123
FIGURE 11.	Model Prediction-Experiment Comparison for the Yield Stress of 20% Cold Worked 316 Stainless Steel	125
FIGURE 12.	Comparison of Predicted and Measured Yield Stresses for a Range of Temperatures and Neutron Fluences	126

Microstructure of Irradiated Fusion Reactor First-Wall Materials

FIGURE 1.	Single-Ion Irradiated Ti64	143
FIGURE 2.	Dual-Ion Irradiated Ti64	144
FIGURE 3.	Preferential Formation of Cavities at Grain Boundary in Ti64 Dual-Ion Irradiated at 624°C	145

In-Situ HVEM Studies of Helium Irradiated Stainless Steel

FIGURE 1.	Transmission Electron Micrograph Showing Grain Boundary Bubble Enlargement in a 316 SS Sample Irradiated with 80 KeV Helium Ions with an Ion Flux of 1.5 x 10^{15} ions/cm^2 sec and a Sample Temperature of 650°C to a Total Ion Dose of 7 x 10^{17} ions/cm^2	155
FIGURE 2.	Transmission Electron Micrograph Showing Grain Boundary Bubble Enlargement in a 316 SS Sample Irradiated with 80 KeV Helium Ions with an Ion Flux of 6 x 10^{14} ions/cm^2 sec and a Fluence of 3 x 10^{17} ions/cm^2	155

FIGURES (cont'd)

		Page
FIGURE 3.	400 kV Transmission Electron Micrograph of Blisters on a 316 SS Sample Irradiated at a High Temperature and a High Flux	156
FIGURE 4.	Transmission Electron Micrograph of an Exfoliated Area of a Sample Irradiated at a Lower Flux and Temperature Than the Sample Shown in Figure 3	156

Displacement Damage Studies

FIGURE 1.	Yield Strength Increase Versus Particle Fluence for Neutron and Proton Irradiated Nickel	161
FIGURE 2.	Yield Strength Increase Versus Particle Fluence for Neutron and Proton Irradiated Niobium	162

Effects of Bombarding Ions on the Void Swelling Profile in Nickel

FIGURE 1.	The Calculated Displacement Curves for Carbon, Aluminum and Nickel Ions Incident on a Nickel Target	167
FIGURE 2.	Nickel Irradiated at 525°C (798°K) with 8.1 MeV Aluminum Ions *to* Four Fluence Levels	169
FIGURE 3a.	Average Void Diameter $\bar{d}$, Void Density N_v, and Void Volume Fraction $\Delta V/V$ Measured as a Function of Depth in Nickel Irradiated with Aluminum Ions	171
FIGURE 3b.	Average Void Diameter $\bar{d}$, Void Density N_v, and Void Volume Fraction $\Delta V/V$ Measured as a Function of Depth in Nickel Irradiated with Aluminum Ions	172
FIGURE 4.	Void Size Distributions at Two Depths in Nickel Irradiated with Aluminum Ions to Two Fluence Levels	173
FIGURE 5.	Nickel Irradiated at 525°C (798°K) with 5 MeV Carbon Ions to Two Fluence Levels	174
FIGURE 6a.	Average Void Diameter, Void Density, and Void Volume Fraction as a Function of Depth in Nickel Irradiated with Carbon Ions to 1.5 x 10^{16} cm^{-2}	176

FIGURES (cont'd)

Page

FIGURE 6b. Average Void Diameter, Void Density, and Void Volume Fraction as a Function of Depth in Nickel Irradiated with Carbon Ions to 9.2 x 10^{16} cm^{-2} 177

FIGURE 7. Dislocation Structure Development in Ion Irradiated Nickel 178

FIGURE 8. A Comparison of Nickel Specimens Irradiated at 525°C (798°K) with Three Different Ions to Fluence Levels Giving Similar Peak Damage Levels 180

FIGURE 9. Average Void Diameter, Void Density, and Void Volumne Fraction as a Function of Depth in Nickel Irradiated with 14 MeV Nickel Ions at 525°C (798°K) to a Fluence Level of 1.3x10^{16} ions/cm2 181

FIGURE 10. The Primary Recoil Energy Spectra for the Three Ions Incident on Nickel

Damage Correlation

FIGURE 1. Thermal and 11 MeV-Proton Irradiation Creep Rates for 20% CW Type 316 Stainless Steel 195

The Effects of Hot Pre-Implantation and Simultaneous Helium Injection on Microstructural Evolution in 316 SS

FIGURE 1. The Effect of Time, Temperature and Mode of Helium Implantation on Carbide ($M_{23}C_6$) Precipitation in 20% Cold-Rolled 316 SS 204

FIGURE 2. Changes in Cavity Size and Density Across a Grain Boundary as a *Result of* Partial Recrystallization 205

FIGURE 3. Cavities Appear Mostly in Cell Interiors, Not Associated with Cell Wall Dislocation Tangles 206

FIGURE 4. Heterogeneous Cavity Formation on Rod-Shaped Precipitates in Grain Interiors 207

FIGURE 5. Effects of the Mode of Helium Implantation on Cavity Formation in 20% Cold-Worked 316 SS 208

FIGURE 6. Effects of the Mode of Helium Implantation on Cavity Formation in Solution Annealed 316 SS 209

FIGURES (cont'd)

Page

FIGURE 7. Effects of the Mode of Helium Implantation on Interstitial Dislocation Loop Formation in Solution Annealed 316 SS 210

TABLES

Page

CHAPTER 3

Experiments at U.C. Davis, Be(d,n), E_d = 40 MeV

TABLE 1. Unfolded Flux for Styris 4 (40 MeV) 18

TABLE 2. Unfolded Flux for Styris 3 (40 MeV) 19

Helium Analyses of Be(d,n)-Irradiated Pure Elements

TABLE 1. Additional Measurements of Helium Concentrations in Be(d,n)-Irradiated Pure Element Ring Segments 26

Flux Damage Parameter Sensitivity Study

TABLE 1. Spectral-Averaged Damage Parameters for Cu and Nb 45

Extrapolation of Damage Cross Sections for Copper

TABLE 1. Spectral Averaged Damage Parameters for Copper 50

Boron Doping of Stainless Steel by Rapid Quenching

TABLE 1. Cross Sections Used in Flux Measurements 59

Dosimetry Cross Section File

TABLE 1. Integral Cross Section Tests 67

CHAPTER 4

Displacement Functions for Multicomponent Systems

TABLE 1. Fraction of Type j Displacements Produced by an Initial Recoil Atom of Type i in TaO 74

CHAPTER 5

DAFS Test Matrix for the EBR-II Reactor Experiment

TABLE 1. Atomic Misfits of Alloying Elements in Ti 132

TABLE 2. Composition Matrix of Fe-Ni-Cr Tensile Specimens 134

CHAPTER 1

DAFS TASK GROUP ACTIVITIES

I. PROGRAM

Title: Irradiation Effects Analysis
Principal Investigator: D. G. Doran
Affiliation: Hanford Engineering Development Laboratory

II. OBJECTIVE

The objective of this work is to coordinate the activities of the DAFS Task Group.

III. RELEVANT DAFS PROGRAM PLAN TASK/SUBTASK

All tasks

IV. SUMMARY

Task Group activities included review of plans for neutron field characterization of FMIT, formulation of plans for neutron field characterization of RTNS-II, implementation of the microstructural evolution program, and initiating a fundamental mechanical behavior program. The DAFS Program Plan was published.

V. ACCOMPLISHMENTS AND STATUS

The DAFS Program Plan was published and is available from the National Technical Information Service (address on front cover) as U. S. Department of Energy Report DOE/ET-0032/2, July 1978.

Several Subtask Group meetings have been held this quarter (see below). A full Task Group meeting is scheduled for October 30-31, 1973 in Germantown, Maryland.

SUBTASK GROUP ACTIVITIES

Subtask Group A -- Environmental Characterization (L. R. Greenwood, ANL, Chairman)

The Fusion Materials Irradiation Test facility (FMIT) is now being designed at HEDL for operation in 1983. A 100 mA deuteron beam at E_d = 35 MeV will be stopped in a flowing, liquid lithium target to produce a flux of about 10^{15} n/cm^2-s near the source. The FMIT Dosimetry Plan was reviewed by the Subtask Group at ANL in March and at HEDL in May. Additional discussions were held during June and July, especially during the ASTM meeting in Richland, Washington, July 10-11, 1978. The dosimetry plan emphasizes the need for passive in-situ dosimetry, with active and calculational techniques used to augment the measurements and to provide a time history for irradiations. Initial FMIT characterization will include active measurements performed via various service plugs or directly inside the test cell at low beam currents.

Discussions are now being held to plan the dosimetry characterization of RTNS-II, a T(d,n) source nearly completed at LLL with an expected flux of about 10^{13} n/cm^2-s. Initial characterization will be done by LLL, principally using the ^{93}Nb(n,2n)^{92m}Nb reaction to map flux contours. More detailed mapping using a variety of reactions and helium monitors will be conducted once the facility reaches a stable configuration, mainly by L. Greenwood (ANL), M. Guinan (LLL), and H. Farrar, IV (AI). Later measurements will include room return spectra, the flux-spectra far from the source, and cross-section testing.

Subtask Group C -- Correlation Methodology (G. R. Odette, UCSB, Chairman)

Subtask Group C, consultants and guests, met on July 13 and 14, 1978 in Richland,. Washington in conjunction with the 9th ASTM International Symposium on the Effect of Irradiation on Structural Metals. The purpose

of the meeting was to 1) review the status of the microstructural evolution program and initiate implementation of the next critical steps; and 2) finalize plans for and begin implementation of a fundamental mechanical behavior program.

R. W. Powell chaired the subgroup on correlation methodology for microstructure. Topics considered at the meeting included: disposition of the MFE-I test specimens with recommendations to be forthcoming from an ad hoc committee (MFE-I was discharged in July 1978), review of the dual-ion program and further planning of an intercorrelation experiment, a review of "hot" helium preinjection capabilities to soon be in place at ANL, and discussion of a workshop on microstructural examination techniques to take place within the next year. Future fission reactor test matrices and materials were also discussed. Finally, an indication of upcoming issues, including the utilization of RTNS-II and a scoping test matrix for FMIT were noted.

J. J. Holmes chaired the subgroup on mechanical properties. Following up on an informal meeting in San Francisco on April 21, 1978, a general strategy and initial assignments for the Fundamental Mechanical Behavior Program were developed. Assignments included developing mechanical property maps for Path A, B and C alloys; initial review of hydrogen effects; a review of potential stress state effects on failure; initial scoping of a surface analysis-helium embrittlement facility for DAFS; and appropriate mechanical test procedures. The RTNS-II Utilization Plan and the need for a scoping test matrix for FMIT were briefly discussed. Finally the critical need for reactor tests was re-emphasized and a preliminary recommendation formulated on general space and test specimen requirements. Specifically, it was recommended that about 20% of reactor space from ADIP irradiations be made available to DAFS to build an inventory of irradiated mechanical test specimens.

Other DAFS activities during the quarter include a preliminary formulation of a materials bank and an experimental test matrix policy for DAFS

which will be circulated for review. The MFE-II test aimed at studying helium effects was inserted into ORR and the subtask group and its representatives continued to participate in various MFE planning activities.

CHAPTER 2

IRRADIATION TEST FACILITIES

I. PROGRAM

Title: Irradiation Effects Analysis
Principal Investigator: D. G. Doran
Affiliation: Hanford Engineering Development Laboratory

II. OBJECTIVE

The objective of this work is to develop a national program plan for the effective utilization of the RTNS-II and other high energy neutron facilities.

III. RELEVANT DAFS PROGRAM PLAN TASK/SUBTASKS

All tasks are relevant in that the utilization of high energy neutron sources is an integral part of the DAFS Program strategy. The tasks expected to be affected most directly are:

TASK II.A.2 High Energy Neutron Dosimetry
II.A.4 Gas Generation Rates
II.A.5 Dosimetry Technique Development
II.B.3 Experimental Characterization of Primary Damage State
II.B.4 Damage Production in Insulators
II.C.1 Effect of Material Parameters on Microstructure
II.C.2 Effect of Helium on Microstructure
II.C.6 Effect of Damage Rate and Cascade Structure Microstructure
II.C.7 Effect of Helium and Displacements on Flow
II.C.8 Effect of Helium and Displacements on Fracture
II.C.11 Effects of Cascades and Flux on Flow
II.C.18 Relating Low and High Exposure Microstructures

IV. SUMMARY

The RTNS-II Utilization Plan was completed, printed, and is currently being distributed.[1]

V. REFERENCES

1. RTNS-II Utilization Plan, U. S. Department of Energy Report DOE/ET-0066, September 1978.

CHAPTER 3

SUBTASK A: ENVIRONMENTAL CHARACTERIZATION

I. PROGRAM

Title: Dosimetry and Damage Analysis
Principal Investigator: L. R. Greenwood
Affiliation: Argonne National Laboratory

II. OBJECTIVE

To determine the flux-spectrum at various locations in the Oak Ridge Research Reactor (ORR) and to provide dosimetry and damage analysis for MFE irradiation effects experimenters.

III. RELEVANT OAFS PROGRAM TASK/SUBTASK

SUBTASK II. A.l.l Flux-spectral definition in a tailored fission reactor.

IV. SUMMARY

The first MFE irradiation in DRR (MFE1) was completed in July, 1978. The second run (MFE2) was started in September and should continue for about one year. A low power irradiation is scheduled in October in the same location as MFE2 to measure the flux-spectrum. All irradiations contain dosimetry materials from ANL and Atomics International (AI).

V. ACCOMPLISHMENTS AND STATUS

Experiments at ORR -- L. R. Greenwood and R. R. Heinrich

Dosimetry has been provided for three irradiations in the Oak Ridge Research Reactor (ORR). ORR-MFE1 in core position C3 started in February and ended in July. The capsules included dosimetry wires and helium

monitors from Atomics International (AI). Due to gamma heating problems the irradiation was ended prematurely. The capsules were allowed to cool at ORNL and were disassembled in September. Dosimetry materials are now being shipped to ANL and AI for analysis.

A second irradiation (ORR-MFE2) was started in core position E7 in September and should continue for about 1 year. Dosimetry wires (Fe, Ni, Co-Al, and Ti) in small packages measuring about 0.050" in diameter by 0.25" long were included with each of the 16 heaters used to keep a variety of tensile specimens at constant temperatures between 250-550°C. Additional wires and helium capsules were placed in aluminum tubes running the entire length of the irradiation capsule.

A low power spectral mapping study has also been planned, and should be done the week of October 23. The test was originally scheduled for July but had to be postponed due to unforeseen problems at ORR. The spectral test will be in core position E7, thus necessitating the temporary removal of the ORR-MFE2 capsule. Dummy graphite cylinders are also being made to mock-up a nearby experiment which should perturb the spectrum. This will guarantee that the measured spectrum is identical to that seen by ORR-MFE2; however, the spectrum may be significantly different from that seen by ORR-MFE1.

The spectral test requires low power (~ 3 kW) so that cadmium covers and fissile monitors can be safely included; ^{10}B and ^{6}Li helium monitors are also included. We plan to disassemble the capsule at ORNL shortly after the irradiation so that samples with short half-lives can be counted quickly at ANL.

VI. REFERENCES

None

VII. FUTURE WORK

Analysis of the dosimetry samples by ANL and AI will continue into FY 1980. Plans for irradiation of MFE3 are now being formulated.

VIII. PUBLICATIONS

None

I. PROGRAM

Title: Dosimetry and Damage Analysis
Principal Investigator: L. R. Greenwood
Affiliation: Argonne National Laboratory

II. OBJECTIVE

To develop dosimetry techniques and provide dosimetry and damage analysis for MFE experimenters in Be(d,n) irradiation facilities.

III. RELEVANT DAFS PROGRAM PLAN TASK/SUBTASK

SUBTASK II. A.2.1 Flux-spectral definition in Be(d,n) field.

IV. SUMMARY

Results are presented for irradiations conducted for Battelle Pacific Northwest Laboratories (PNL) at the U. C. Davis cyclotron using the Be(d,n) field at E_d = 40 MeV during February, 1978. Additional irradiations were also conducted during September, 1978.

V. ACCOMPLISHMENTS AND STATUS

Experiments at U. C. Davis, Be(d,n), E_d = 40 MeV -- L. R. Greenwood and R. R. Heinrich

Two irradiations were conducted for O. Styris and R. Jones (PNL) at the U. C. Davis cyclotron using the Be(d,n) reaction at E_d = 40 MeV. A large number of tensile specimens (10 mil wires) and dosimetry foils were irradiated at two locations, about 6 and 26 mm from the estimated center of the neutron source.

The first run was conducted in February with a total charge of 2.1 coulombs over about 23 hours. The dosimetry packets, labeled 3 and 4, consisted of Ni, Co, Nb, Au, Fe, In, and Al foils measuring about 8 mm x 13 mm. The Al and In foils were sent to Livermore (LLL) for counting, however, the In foils could not be shipped in time due to the high residual activity in the target room at U. C. Davis. The remaining foils were counted at ANL. Nickel foils were placed on the front and rear of the packets to measure geometry and absorption effects. As expected, in close geometry (6 mm), the geometric effect is nearly $1/R$, whereas further from the source (26 mm) the effect is about $1/R^2$.

The foils were cut into six strips (A-G) about 1.5-2.0 mm wide and about 8 mm long with the tensile specimens parallel to the longer dimension. The average flux-spectrum on a given foil is thus about the same as that on the wires, although the flux-spectrum varies significantly along a given wire. Activation data for eleven reactions for each of the six strips was used to unfold the flux-spectrum using the SANDII and SANDANL codes. The results, including a Monte Carlo error analysis, are given in Tables I and II. Spectra representing the highest flux regions at the two distances from the source are shown in Figures 1 and 2. Preliminary damage calculations have also been performed for this run using a newly developed computer library. The results are given in the contribution for Subtask II.A.3.1.

In order to further investigate the flux-spectral gradients, three of the nickel foils (F, E, and A) at the 6 mm position were further subdivided into five pieces, each piece being less than 2 mm square. A computer program was then written to calculate the average radial displacement of each sub-section from the beam axis. Since the neutron field is cylindrically symmetric, the results should fall on a smooth curve defining the radial flux-spectral gradient within the limits of our resolution. The results are shown in Figure 3. As can be seen, the

Table I: Unfolded flux for Styris 4 (40 MeV)

$\Phi \times 10^{12}$ n/cm^2-sec, $\bar{I}$ = 25.3 μA, ≤mm

	Average Width, mm	G 4.0		F 1.8		E 1.3		A 2.2		B 1.8		C 1.5	
			±%		±%		±%		±%		±%		±%
ota		1.53	10	3.00	6	3.55	5	2.86	6	1.74	8	1.13	10
>.1		1.50	10	2.96	5	3.51	5	2.82	6	1.71	8	1.10	[illegible]
>.5		1.40	7	2.83	5	3.38	5	2.70	5	1.61	6	1.03	7
> 1		1.30	6	2.73	3	3.26	5	2.60	5	1.52	6	0.96	6
> 4		0.96	5	2.26	3	2.76	5	2.14	5	1.15	5	0.69	5
>10		0.58	4	1.49	4	1.90	4	1.42	4	0.68	4	0.38	4
>14		0.38	8	1.05	3	1.36	7	1.00	8	0.47	8	0.23	9
>20		0.18	10	0.51	10	0.64	10	0.49	10	0.22	10	0.11	10
>25		0.11	13	0.27	11	0.35	12	0.27	11	0.12	11	0.057	10
>30		0.06	21	0.14	20	0.20	22	0.13	25	0.06≤	24	0.024	28
>35		0.02≤	48	0.054	5≤	0.080	50	0.052	59	0.02≤	55	0.009	68
		0.23	47	0.27	4[illegible]	0.23	48	0.27	47	0.22	47	0.17	47
		0.57	26	0.74	1[illegible]	0.73	17	0.73	19	0.≤4	21	0.44	24
	. (%)	7 7		5 0		3 3		5 ≤		5 2		3 2	

Table II: Unfolded flux for Styris 3 (40 MeV)

$\Phi \times 10^{11}$ n/cm^2-sec, $\bar{I}$ = 25.3 μA, 26 mm

E (MeV)	Average Width, mm	G 3.5	±%	F 1.6	±%	E 1.[illegible]	±%	A 1.6	±%	B 1.3	±%	C 3.5	±%
Total		4.92	5	5.91	4	5.[illegible]7	4	5.10	4	4.25	5	3.07	6
>.1		4.87	5	5.87	4	5.[illegible]3	4	5.06	4	4.21	5	3.02	6
>.5		4.74	5	5.73	4	5.50	4	4.93	5	4.06	5	2.88	5
> 1		4.62	6	5.61	5	5.[illegible]8	5	4.81	5	3.93	5	2.75	5
> 4		4.11	6	5.12	5	4.[illegible]1	5	4.34	5	3.44	5	2.29	5
>10		3.21	6	4.14	4	3.[illegible]8	4	3.43	4	2.64	4	1.64	4
>14		2.36	8	3.11	8	2.[illegible]9	8	2.56	8	1.97	7	1.19	8
>20		1.26	12	1.54	10	1.[illegible]9	10	1.36	10	1.05	10	0.67	10
>25		0.54	23	0.62	12	0.59	12	0.56	11	0.46	11	0.31	11
>30		0.21	53	0.25	25	0.22	26	0.19	27	1.17	27	0.13	26
>35		0.082	86	0.088	51	0.[illegible]7[illegible]	53	0.067	57	0.059	57	0.044	56
< 1		0.30	50	0.3[illegible]	4[illegible]	0.2[illegible]	4[illegible]	0.29	49	0.[illegible]	[illegible]	0.32	48
< 4		0.80	1[illegible]	0.7[illegible]	1[illegible]	0.7[illegible]	1[illegible]	0.76	16	0.[illegible]	[illegible]9	0.78	22
[illegible]td D[illegible]V (%)		10.4		[illegible]		[illegible]7		7.[illegible]		[illegible]		[illegible]7	

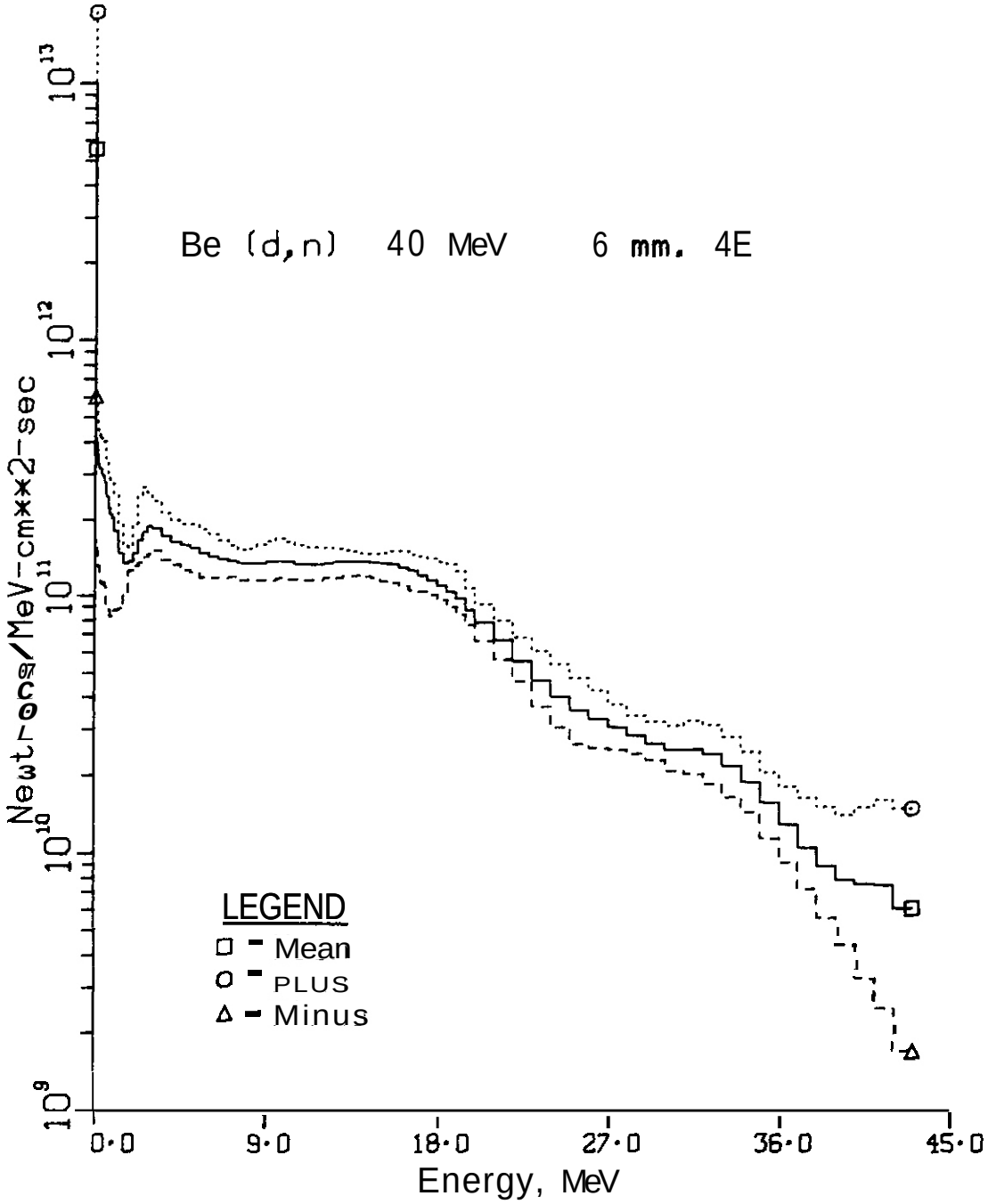

FIGURE 1. Be(d,n) spectrum unfolded at the U. C. Davis cyclotron for PNL. The dashed and dotted lines represent plus and minus one standard deviation. The foils measured about 1.8 mm by 9 mm and were located on the beam axis about 6 mm from the neutron source.

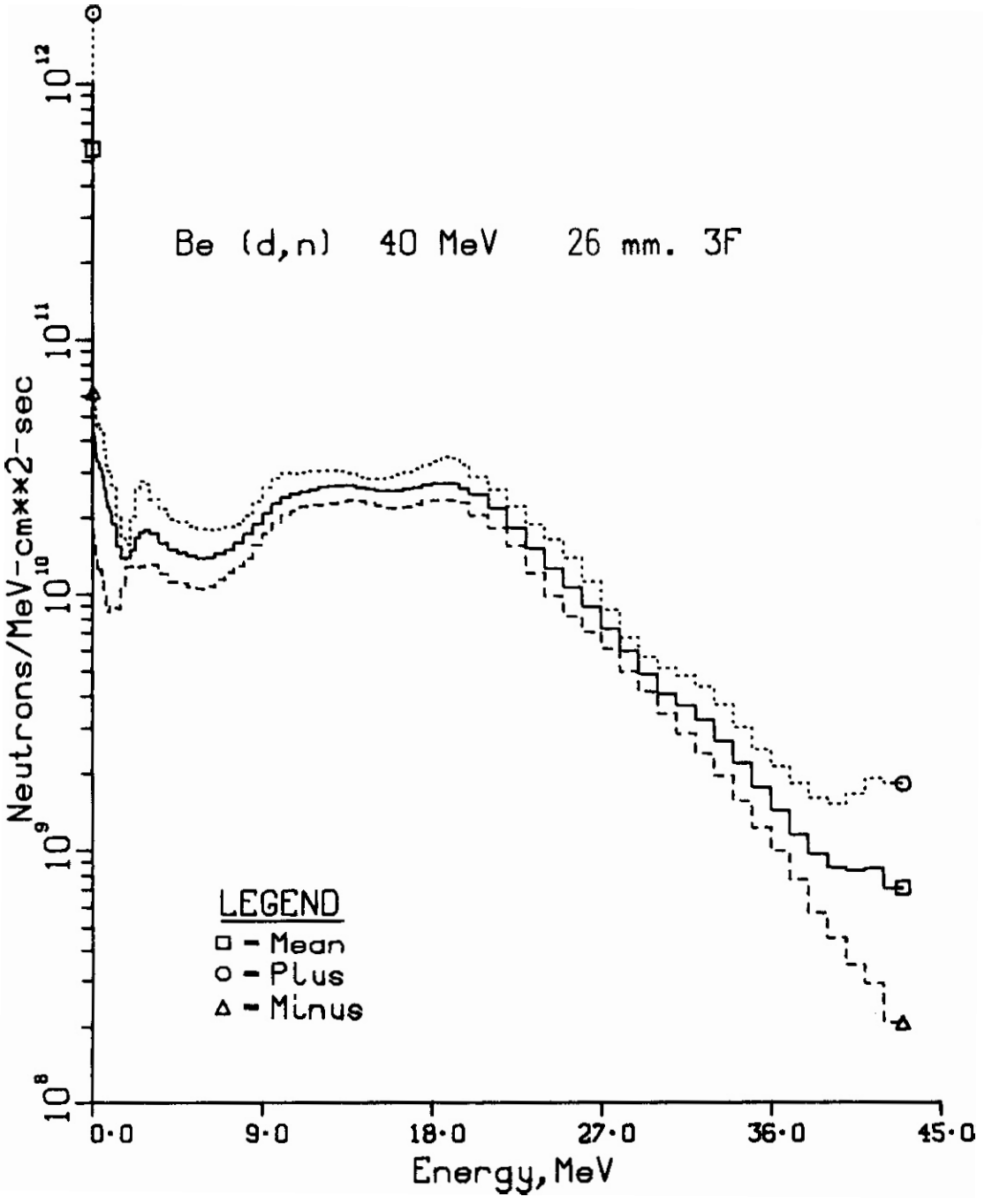

FIGURE 2. Be(d,n) spectrum unfolded at the U. C. Davis cyclotron for PNL. The dashed and dotted lines represent plus and minus one standard deviation. The foils measured about 1.6 mm by 8 mm and were located about 26 mm from the neutron source.

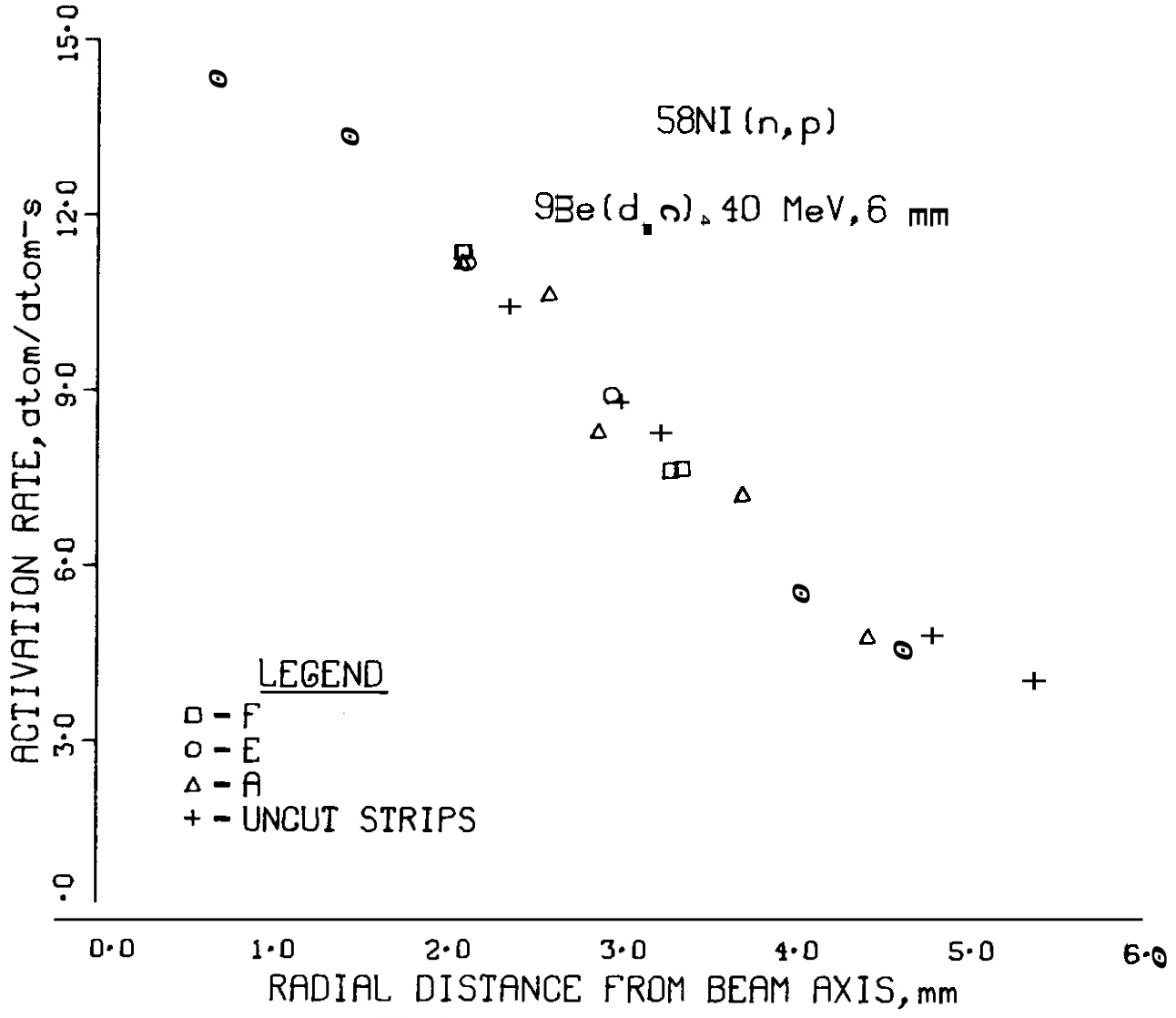

FIGURE 3. Radial activity map for $^{58}Ni(n,p)$ strips measuring about 1.8 mm square cut from larger strips about 1.8 mm by 9 mm. As can be seen, the flux-spectral gradients are quite steep and show cylindrical symmetry about the beam axis.

field is indeed cylindrically symmetric about the beam axis and the beam center can be easily located to within about ± 0.2 mm by this technique.

The second irradiation for PNL was conducted in September and activation foils are now being counted at ANL and LLL. Two dosimetry packets, labeled 5 and 6, were placed at about 6 and 26 mm from the source and consisted of Ni, Co, Nb, Au, Zr, and Al foils. The Fe and In were omitted and Zr was added this time. Indium cannot be retrieved in time from the cyclotron vault and Fe reaction cross-sections are known to have large errors from our integral testing program.

We should also note that results given previously (DOE/ET-0065/1) for PNL (Run 2) were also at E_d = 40 MeV, not 30 MeV as stated. The flux results from that run are about 78% higher than Run 4 (given in Table I) due to slight differences in positioning and beam spot diameter. This enormous difference underscores the fact that passive in-situ dosimetry is a necessity in these close geometry irradiations.

VI. REFERENCES

None

VII. FUTURE WORK

Analysis of the dosimetry for the PNL irradiation in September should be completed during the first quarter of FY 1979.

VIII. PUBLICATIONS

An abstract concerning this work has been accepted and a paper will be presented at the First Topical Meeting on Fusion Reactor Materials, January 29-31, 1979, in Miami Beach, Florida.

I. PROGRAM

Title: Helium Generation in Fusion Reactor Materials
Principal Investigators: D. W. Kneff, Harry Farrar IV
Affiliation: Energy Systems Group, Rockwell International

II. OBJECTIVE

The objectives of this work are to measure helium generation rates of materials for Magnetic fusion Reactor applications in the broad-band Be(d,n) neutron environment, to characterize the Be(d,n) neutron fluence and neutron energy distributions as a function of position relative to the neutron source, particularly in the high-flux region, and to develop helium accumulation fluence monitors for neutron fluence and energy spectrum dosimetry for fusion-program neutron irradiations.

111. RELEVANT DAFS PROGRAM PLAN TASK/SUBTASK

SUBTASK II.A.2.1	Flux-Spectral Definition in the Be(d,n) Field
SUBTASK II.A.4.3	Be(d,n) Helium Gas Production Data
SUBTASK II.A.5.1	Helium Accumulation Monitor Development

IV. SUMMARY

Helium analyses have been completed for 23 additional pure element specimens irradiated in the Be(d,n) neutron field using 30-MeV deuterons. These specimens are from the eleven Al, Fe, Ni, Cu, and Au wire rings incorporated in the experiment for both cross section and helium accumulation neutron dosimetry applications. The weighing of the ~300 radiometrically-counted dosimetry foil segments from the irradiation capsule has also been initiated.

V. ACCOMPLISHMENTS AND STATUS

Helium Analyses of Be(d,n)-Irradiated Pure Elements -- D. W. Kneff, Harry Farrar IV, and M. M. Nakata (Energy Systems Group, Rockwell International)

The analysis is continuing of the pure element wire rings irradiated in the Be(d,n) neutron environment using 30-MeV deuterons. The primary objectives of this irradiation experiment were to measure the spectrum-integrated helium-generation cross sections of a large number of pure elements, separated isotopes, and alloys of potential fusion reactor design interest; to characterize the position-sensitive neutron fluence and energy spectra of the Be(d,n) neutron environment in detail; and to evaluate and use helium accumulation materials as neutron fluence and energy dosimeters. The experiment was undertaken jointly with personnel from Argonne National Laboratory (ANL) and Lawrence Livermore Laboratory (LLL). The experiment and the initial analysis results have been described in detail in previous Rockwell International reports.[1,2]

During the report period, helium analyses were completed for 23 additional pure element specimens from the eleven Al, Fe, Ni, Cu, and Au wire rings incorporated in the experiment for both cross section and helium accumulation dosimetry applications. The analyses were made using the Rockwell International high-sensitivity gas mass spectrometer system. The results, presented in Table 1, bring the total number of Be(d,n) helium analyses to date to 52. The analyzed segments represent various locations around seven of the eleven helium dosimetry rings, whose irradiation geometry is shown schematically in the previous DAFS quarterly progress report.[2] The smooth variation in the helium concentration results for each dosimetry ring corresponds to the non-symmetric ring orientation relative to the neutron source axis, and thus to the changing neutron fluence with source angle. The effective application of helium

TABLE 1

ADDITIONAL MEASUREMENTS OF
HELIUM CONCENTRATIONS IN Be(d,n)-IRRADIATED PURE ELEMENT RING SEGMENTS

Dosimetry Ring	Segment Number	Angular Orientation*	Segment Mass (mg)	Measured Number of ^{4}He Atoms	Helium Concentration (appb)†
Al Layer 3	GAL-W2A	72°	1.0271	2.935×10^{11}	12.80
	GAL-W2C	12°	0.7912	2.310×10^{11}	13.08
	GAL-W2E	312°	0.9454	3.277×10^{11}	15.53
	GAL-W2G	255°	1.0994	4.887×10^{11}	19.91
	GAL-W2I	194°	1.2745	5.919×10^{11}	20.80
	GAL-W2K	134°	1.322	5.093×10^{11}	17.26
Ni Layer 3	GNI-W2C	46°	3.080	4.345×10^{11}	13.75
	GNI-W2G	348°	2.631	4.052×10^{11}	15.01
	GNI-W2W	122°	2.173	3.776×10^{11}	16.94
Cu Layer 2	GCU-W1A	83°	2.946	7.277×10^{10}	2.61
	GCU-W1C	53°	2.471	5.710×10^{10}	2.44
	GCU-W1K	287°	3.039	1.020×10^{11}	3.54
	GCU-W1M	253°	3.381	1.302×10^{11}	4.07
	GCU-W1S	162°	2.458	8.811×10^{10}	3.78
Outer Cu Layer 3	GCU-W2A	75°	2.173	8.126×10^{10}	3.95
	GCU-W2C	360°	2.134	7.578×10^{10}	3.75
	GCU-W2E	353°	2.737	9.956×10^{10}	3.84
	GCU-W2G	312°	3.054	1.396×10^{11}	4.82
	GCU-W2I	273°	2.490	1.343×10^{11}	5.69
	GCU-W2K	230°	2.819	1.684×10^{11}	6.30
	GCU-W2M	189°	2.702	1.619×10^{11}	6.32
	GCU-W20	148°	2.676	1.311×10^{11}	5.17
	GCU-W2Q	113°	1.660	5.603×10^{10}	3.56

*Average angular orientation of segment about the irradiation capsule axis in the plane of the ring.

†Helium concentrations in atomic parts per billion (10^{-9} atom fraction). The variation in the results for each ring reflects the neutron fluence variation with source angle (see text).

accumulation dosimetry to the detailed fluence mapping of an irradiation experiment was demonstrated recently for the T(d,n) neutron environment.[3,4]

The weighing of the Be(d,n) radiometric dosimetry foil segments counted by LLL was also initiated during the report period. The weighing procedure used for both the foil and helium analysis segments, which provides absolute mass values to <0.5 μg (–0.02%), uses a substitution weighing scheme with mass standards traceable to the National Bureau of Standards.

VI. REFERENCES

1. D. W. Kneff and H. Farrar IV, Helium Generation in Fusion Reactor Materials, Technical Progress Report for Period April - September 1977, AI-DOE-13219, Atomics International, Canoga Park, CA, January 1978.

2. D. W. Kneff. H. Farrar IV, and M. M. Nakata, "Helium Generation in Fusion Reactor Materials," in Damage Analysis and Fundamental Studies, Quarterly Progress Report April-June 1978, U.S. Department of Energy (in press).

3. H. Farrar IV, D. W. Kneff, R. A. Britten, and R. R. Heinrich, "Fluence Mapping of RTNS-I bv Helium Accumulation and Foil Activation Methods," Proc. Simp. on Neutron Cross-Sections from 10 to 40 MeV, M. R. Bhat and S. Pearlstein, eds., pp. 175-184, Brookhaven National Laboratory, NY, July 1977.

4. D. W. Kneff and H. Farrar IV, "Helium Generation in Fusion Reactor Materials," in Damage Analysis and Fundamental Studies, Quarterly Proqress Report January-March 1978, DOE/ET-0065/1, U.S. Department of Energy, August 1978.

VII. FUTURE WORK

The helium analyses of the pure element wire ring segments will continue. The results will be combined with the radiometric foil results to map the Be(d,n) neutron fluence and energy profiles as a function of

position in the high-flux region of the Be(d,n) neutron environment. The other pure elements, alloys, and separated isotopes irradiated in this experiment will be analyzed for helium, and the results will be combined with the neutron mapping results to determine the helium-generation cross sections for this neutron environment. The results of the combined Rockwell-ANL-LLL neutron dosimetry for this experiment will have significant impact on the dosimetry techniques to **be** applied to the Li(d,n)-based Fusion Materials Irradiation Test Facility (FMIT), now in the design stages at the Hanford Engineering Development Laboratory (HEDL).

VIII. PUBLICATIONS

Two papers have been accepted for presentation at the First Topical Meeting on Fusion Reactor Materials, to be held at Miami Beach, Florida in January 1979:

1. D. W. Kneff and Harry Farrar IV, "Helium Accumulation Fluence Dosimetry for Fusion Reactor Materials Irradiations."
2. F. W Wiffen, E. J. Allen (ORNL), Harry Farrar IV (Rockwell), E. E. Bloom, T. A. Gabriel, H. T. Kerr, and F. G. Perey (ORNL), "The Production Rate of Helium During Irradiation of Nickel in Thermal Spectrum Fission Reactors."

I. PROGRAM

Title: Damage Analysis and Dosimetry Radiation Damage Analysis
Principal Investigator: A. N. Goland
Affiliation: Brookhaven National Laboratory

II. OBJECTIVE

Radiation damage analysis studies associated with the use of electrical insulators in fusion reactors.

III. RELEVANT DAFS PROGRAM PLAN TASK/SUBTASK

SUBTASK II.A.2.4 Flux Spectral Definition in FMIT.

SUBTASK II.B.l Calculation of Displacement Cross Sections.

IV. SUMMARY

The neutron flux produced in an FMIT facility will vary rapidly with position in the high flux region near the lithium target. In addition, introduction of test samples will alter the flux distribution as will neutron scattering within the walls of the irradiation cave. As a preliminary to estimating damage in materials that could be used as insulators in fusion reactors, calculations are being made to characterize the energy and spatial dependence of the neutron flux in a typical irradiation cave containing test samples.

Neutrons are generated by a Monte Carlo source subroutine and are transported using the MORSE transport code having probabilistic flux estimators. The total flux, consisting of the uncollided and collided contributions, is used as input to the damage program DON developed at Brookhaven!') In this way the damage induced by primary knock-on atoms of

aluminum in Al_2O_3 has been evaluated. It is found that the uncollided flux is dominant in producing damage near the lithium target but that it decreases in relative importance as the depth within the test sample increases. It is also found that the flux of neutrons scattered from the walls of the cave is unimportant in producing damage within the test material.

V. ACCOMPLISHMENTS AND STATUS

A computer subroutine that generates neutrons arising from (d,n) reactions in lithium has been written for use with the neutron transport code MORSE. Both stripping and compound nucleus reactions are included in the source routine. The energy of a neutron emerging from the target is determined by combining the momentum of the neutron due to the translational motion of the deuteron with the momentum of the neutron resulting either from internal motion within the deuteron or from the evaporation of a neutron from the compound nucleus.

At present the total reaction cross section for deuterons in lithium is assumed to be independent of deuteron energy. The probability of interaction is thus uniform with depth in the target. A depth of interaction is selected randomly along the range of the deuteron, and the corresponding deuteron energy at that depth is determined from the range-energy relation.

The velocity of the deuteron at the point of interaction is assumed to be parallel to the beam axis; scattering of the deuteron prior to the (d,n) interaction is ignored. Similarly it is assumed that the neutron leaves the target without being scattered. The source routine is set to cut off emission for neutrons having energies less than 1 MeV.

The type of interaction, stripping or compound nucleus, is selected randomly, event by event, with the ratio of 70% stripping and 30% compound

nucleus. This ratio, though probably not optimum, gives a reasonable fit with experimental data.

Stripping Reactions

When the stripping reaction is selected, a value of the neutron's momentum within the deuteron is selected randomly from the momentum probability distribution as determined from Serber's transparent nucleus model.[2] The orientation within the deuteron of this internal momentum is assumed to be isotropic, so the polar angle θ relative to the direction of motion of the deuteron is selected uniformly with solid angle. The azimuthal angle ϕ is selected uniformly in the interval $0 \leq \phi \leq 2\pi$. The energy and direction of the emerging neutron are determined by combining the momentum of the neutron due to the motion of the incident deuteron and the momentum of the neutron within the deuteron.

Compound Nucleus Reactions

For evaporation reactions an energy of the evaporated neutron is selected randomly in accordance with the distribution:[3]

$$N(E)dE = CEe^{-E/\theta}\, dE,$$

with θ being the temperature of the residual nucleus evaluated at its maximum residual excitation energy. Emission of the neutron in the frame of the compound nucleus is assumed to be isotropic. The direction of the emitted neutron in the compound nucleus frame is selected randomly, and its momentum is combined with the momentum due to the translational motion of the incident deuteron to give the energy and angle of the emitted neutron in the lab frame.

In the following calculations the lithium target has dimensions of 10 cm x 1 cm x R_d, with R_d, the target thickness, being the range of the

deuteron in lithium. The deuteron energy used is 30 MeV, and R_d is 1.15 cm.

The intensity of the deuteron beam is assumed to be constant along the 10 cm width of the target, and it approximates a Gaussian distribution across the 1 cm height of the target.[4]

Probabilistic Flux Estimators

Due to the small probability that a given neutron will hit a given detector, a probabilistic approach has been used to estimate the neutron flux at each detector position. The total flux is the sum of the uncollided flux and the collided flux. The uncollided flux is estimated by determining the probability that a neutron from the lithium target will reach a given detector on its first flight. Included in the estimate is the non-absorption probability of the neutron as it passes from the source point to the detector as well as the angular distribution information of the stripping reaction. The statistical weight of each source neutron is set equal to one.

The collided flux is determined at each collision point by computing the probability that the neutron on its next flight could reach a particular detector. Exceedingly large contributions resulting from collisions close to a test point are avoided by testing each flux contribution and by limiting its maximum value to the weight of the neutron - i.e. to the probability that the neutron exists. The statistical weight of the neutron is reduced after each flight by a factor equal to the non-absorption probability for that flight. After many flights the neutron weight becomes small, and its contribution to the collided flux tends towards zero. Included in the collided flux determination is the neutron weight, the non-absorption probability, and the scattering angular distribution. The present calculations include cross sections through the P_3 term.

As mentioned above, the total flux is the sum of the collided and uncollided fluxes. A test of the probabilistic approach was made by comparing the probabilistic results from MORSE with the analytic results from ANISN for the problem of determining the radial dependence of the neutron flux in a long graphite cylinder having an isotropic line source along its axis. The results obtained with the two programs showed good agreement. This agreement is taken as support for the validity of the probabilistic approach used in MORSE.

Neutron Spectra

Neutron spectra were determined by using MORSE to transport neutrons generated in the Li(d,n) target. The typical irradiation cave studied had dimensions of 5'x6'x8' and had one meter thick walls of high density concrete. Neutron spectra were calculated for the case of an empty cave as well as for the case of a typical sample volume with 30x20x20 cm^3 dimensions located in the cave adjacent to the lithium target, Fig. 1. Neutron spectra were determined at seven points within an empty cave, at seven points within a 30x20x20 cm^3 block of graphite located within a cave, at 34 points within a 30x20x20 cm^3 block of iron located within a cave, and at seven points within 30x20x20 cm^3 blocks of graphite and of iron located in a void. The collided and uncollided fluxes were determined separately and were then combined to yield the total flux. With the geometries used and with the separation of collided and uncollided fluxes, the relative importance of the uncollided flux from the target, of the collided flux from the test sample, and of the collided flux from the cave can be determined.

Cross Sections

The initial runs of MORSE were made using 100 group neutron cross sections in ANISN format as supplied by the Radiation Shielding Information Center at Oak Ridge National Laboratory. For these runs the walls of

the irradiation cave were either graphite or iron. Neutrons having energy greater than 14.92 MeV were assigned that energy.

Recently cross sections consisting of ENDF/B-IV information below 20 MeV and of theoretical estimates between 20 and 60 MeV have been compiled for several materials, including high density concrete, by Alsmiller and Barish[5]. These cross sections are now being used with MORSE. The material comprising the walls of the cave has been changed to high density concrete. Use of the Alsmiller-Barish cross sections permits the transport of all neutrons produced by 30 MeV deuterons on a thick lithium target.

A comparison of the collided spectra obtained at a point within an empty cave having graphite walls when the RSIC 100 group cross sections are used and when the 47 group cross sections of Alsmiller and Barish are used is made in Fig. 2. For the calculation with the RSIC cross sections, all neutrons having energy greater than 14.92 MeV were assigned that energy. This distorts the 100 group spectrum in this region. With this exception the two sets of cross sections yield similar spectra.

In Fig. 3 the uncollided neutron spectrum is compared with the total neutron spectrum at a point within a 30x20x20 cm^3 block of iron. The solid line represents a spline fit to the total flux in each neutron group, while the uncollided flux is indicated by points. The difference between the uncollided and total flux in the interval 1 to 6 MeV results from collided flux from within the sample block and not from the walls of the cave.

Damage Calculations

Damage energy and damage cross sections have been evaluated using the program DON incorporating a Lindhard damage energy function of the Robinson type but having coefficients appropriate for a primary knock-on atom of Al in Al_2O_3 as evaluated by Coulter and Parkin.[6] Unlike MORSE,

cross sections used in DON are obtained from the ENDF/B data files. For energies above 20 MeV the cross sections in DON have been equated to the values at 20 MeV.

The cross sections evaluated above 20 MeV by Alsmiller did not include oxygen, and thus it was not possible to use MORSE to determine the influence on the neutron spectra in a large test block of Al_2O_3. Instead, the flux determinations were made for a test volume filled either with iron or graphite. The damage produced by an aluminum primary knock-on atom in a small sample of Al_2O_3 located within the test sample of iron or graphite was then determined by using the ENDF/B cross sections with DON.

The dependence of the damage energy/source neutron upon the depth within the sample volume is shown in Fig. 4. The uncollided flux is dominant near the lithium target but decreases in relative importance as the depth within the sample is increased. The damage is seen to increase at first with increasing depth, This is thought to result from the forward peaked angular distribution of the stripping reaction. For positions near the target only a limited portion of the target contributes to the flux. As the depth in the test block increases, neutrons from a larger portion of the target can contribute to the flux.

It is found that the neutron flux from the walls of the cave contributes practically nothing to the damage energy (less than 1%). These neutrons have a spectrum that is peaked at low energies. In the present calculations using DON, a low energy cutoff of 22.5 eV has been placed on the recoil energy. Since the maximum recoil energy T_{max} arising from a neutron of energy E interacting with an atom having mass M is:

$$= 4ME \quad ,$$

a neutron must have an energy greater than 160 eV before it can transfer

22.5 eV of energy to an aluminum atom. Hence most of the neutron flux originating from the walls of the cave cannot produce displacements in the sample material. Since by far the largest portion of the computer time is spent following neutrons within the walls of the cave, these findings suggest that flux determinations can be greatly simplified by treating the problem of the test material in a void.

VI. REFERENCES

1. D. M. Parkin and A. N. Goland, A Computational Method for the Evaluation of Radiation Effects Produced by CTR-Related Neutron Spectra, BNL-50434, Sept. 1974.

2. R. Serber, Phys. Rev. 72, p. 1008 (1947).

3. R. D. Evans, The Atomic Nucleus, (McGraw-Hill, New York, 1955), p. 403.

4. P. Grand, Proposal for an Accelerator-based Neutron Generator, BNL-20159, p. 97.

5. R. G. Alsmiller, Jr. and J. Barish, Neutron-Photon Multigroup Cross Sections for Neutron Energies $\leq$ 60 MeV., ORNL/TM-6486, Aug. 1978.

6. D. M. Parkin and C. A. Coulter, Transactions of the American Nuclear Society. 1977 Winter Meeting, San Francisco, Ca. 27, 318 (1977).

VII. FUTURE WORK

Future work in this study will include:

1. refining certain assumptions such as that of assuming the (d,n) reaction in lithium to be independent of energy,

2. completing the necessary processing of ENDF/B-IV cross sections needed for use with the damage program DON,

3. including gamma ray generation in MORSE-(MORSE has been run successfully for gamma rays only, but runs with coupled neutrons and gama rays have been prohibitively long. Selection of appropriate energy cut-offs should improve the situation.),

4. continuing the work on formulating a method of estimating damage induced in insulators by fluxes of neutrons and gama rays.

VIII. PUBLICATIONS

A paper entitled "Radiation Damage in CTR Insulators" has been accepted for presentation at the First Topical Meeting on Fusion Reactor Materials, Miami Beach, Fla., January 1979.

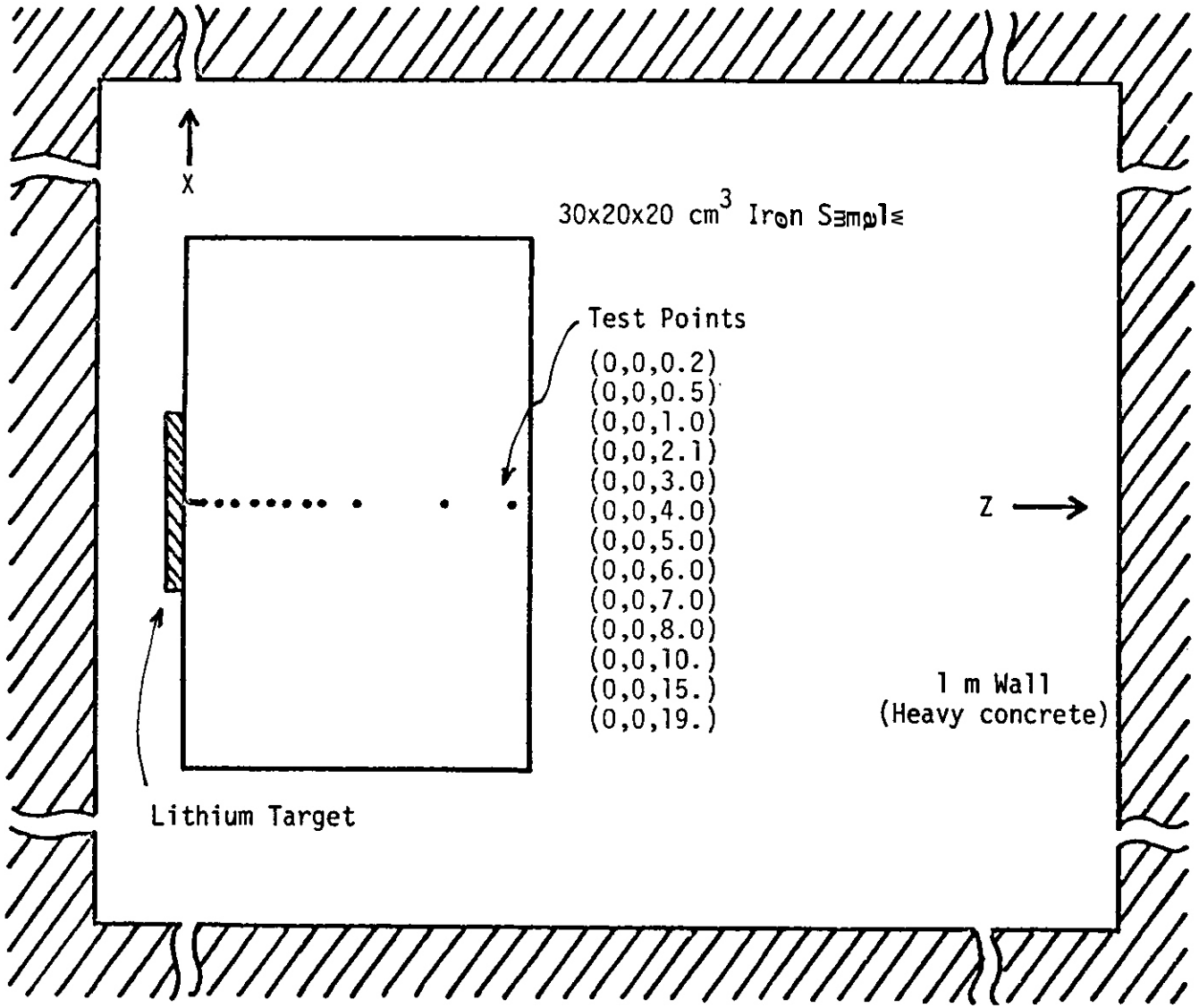

FIGURE 1 Geometry Used for Computing Neutron Spectra Within a 30x20x20 cm^3 Test Sample of Iron Located in a 6'x6'x8' Irradiation Cave.

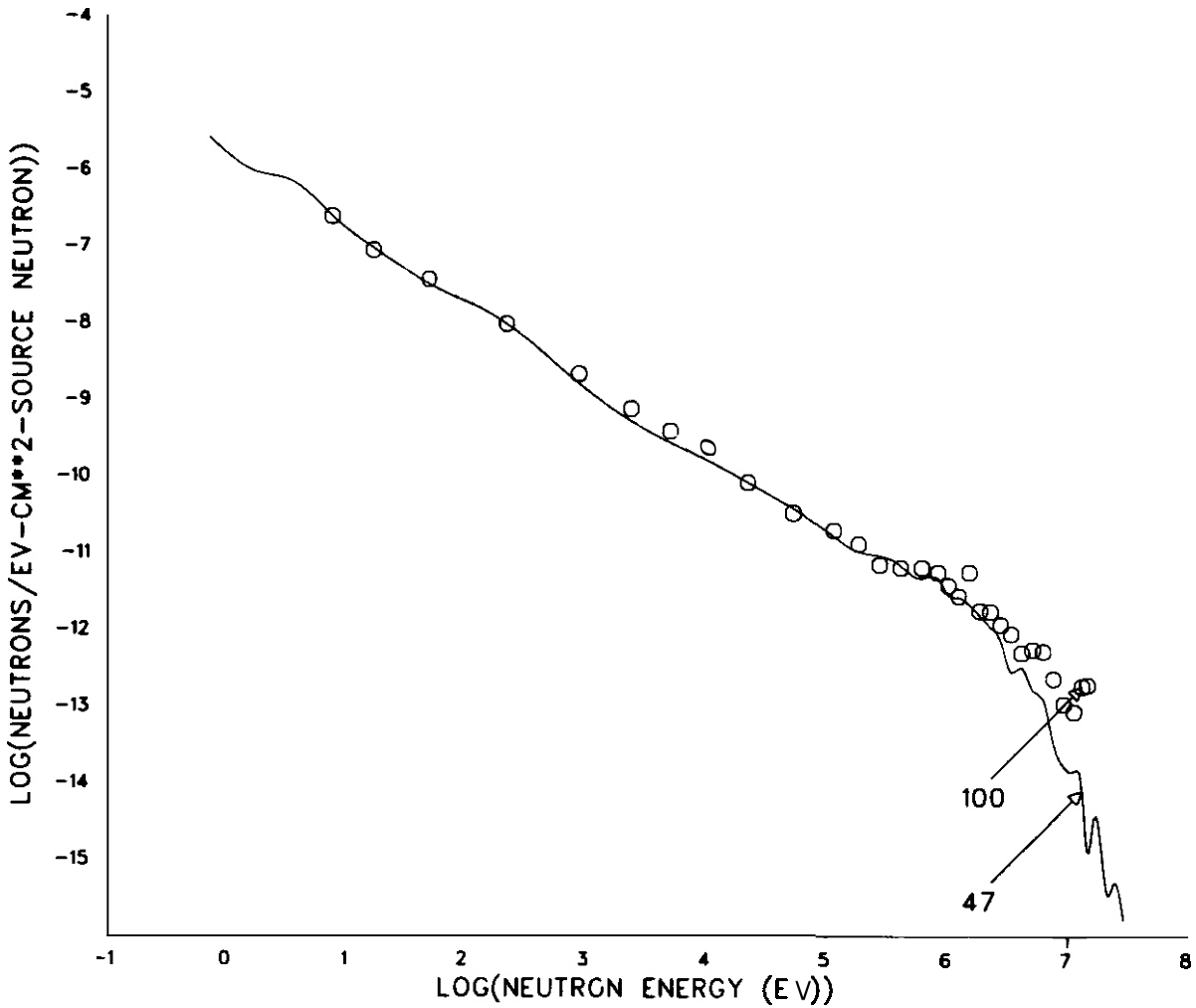

FIGURE 2 Comparison of Neutron Spectra Obtained from RSIC 100 Group Cross Sections and the Alsmiller and Barish 47 Group Cross Sections. Collided Flux within an Empty Cave Having Graphite Walls.

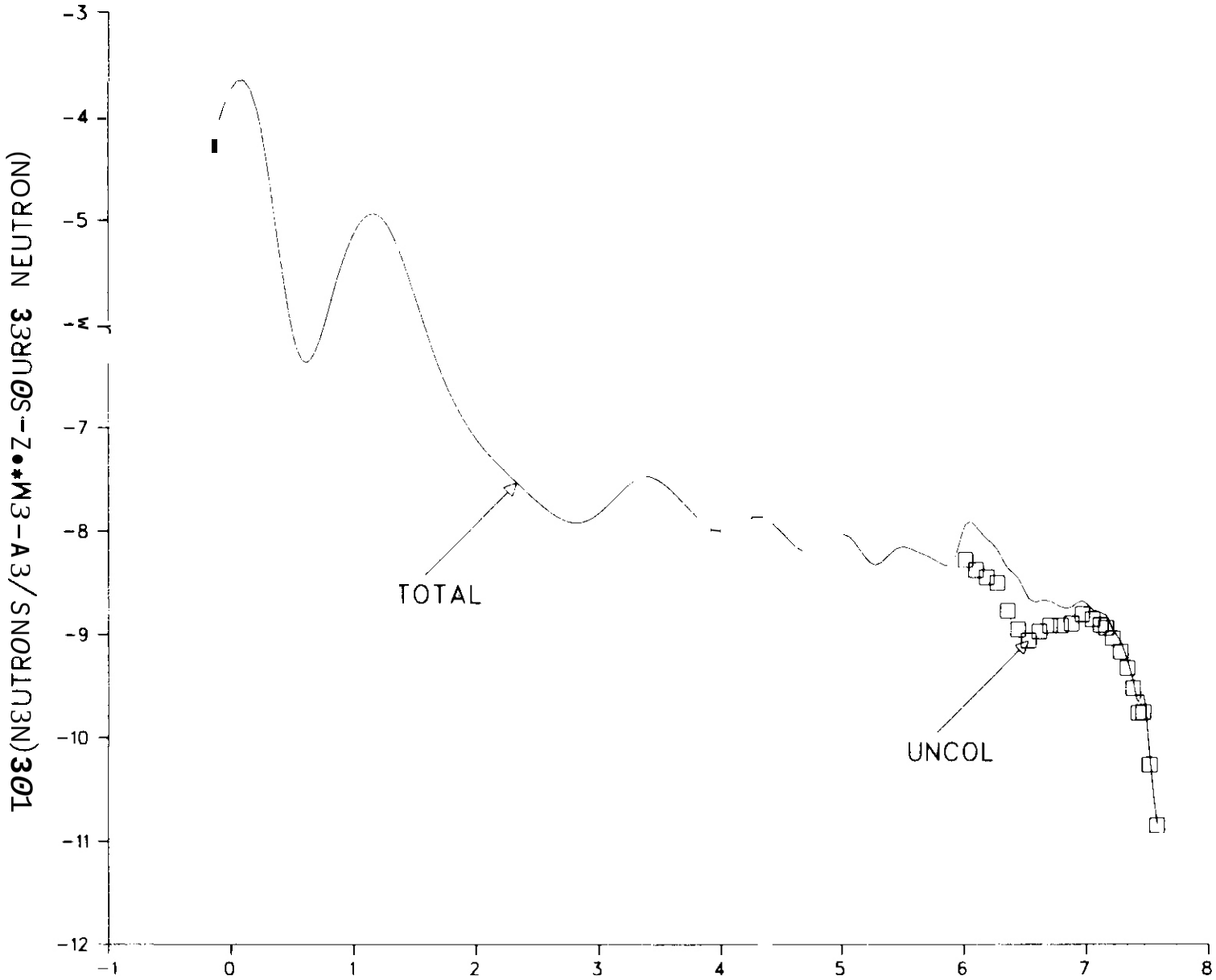

FIGURE 3 Comparison of the Uncollided Spectrum with the Total Spectrum at the Point (0,0,1) within a 30x20x20 cm^3 Block of Iron Located within an Irradiation Cave Having Walls of High Density Concrete.

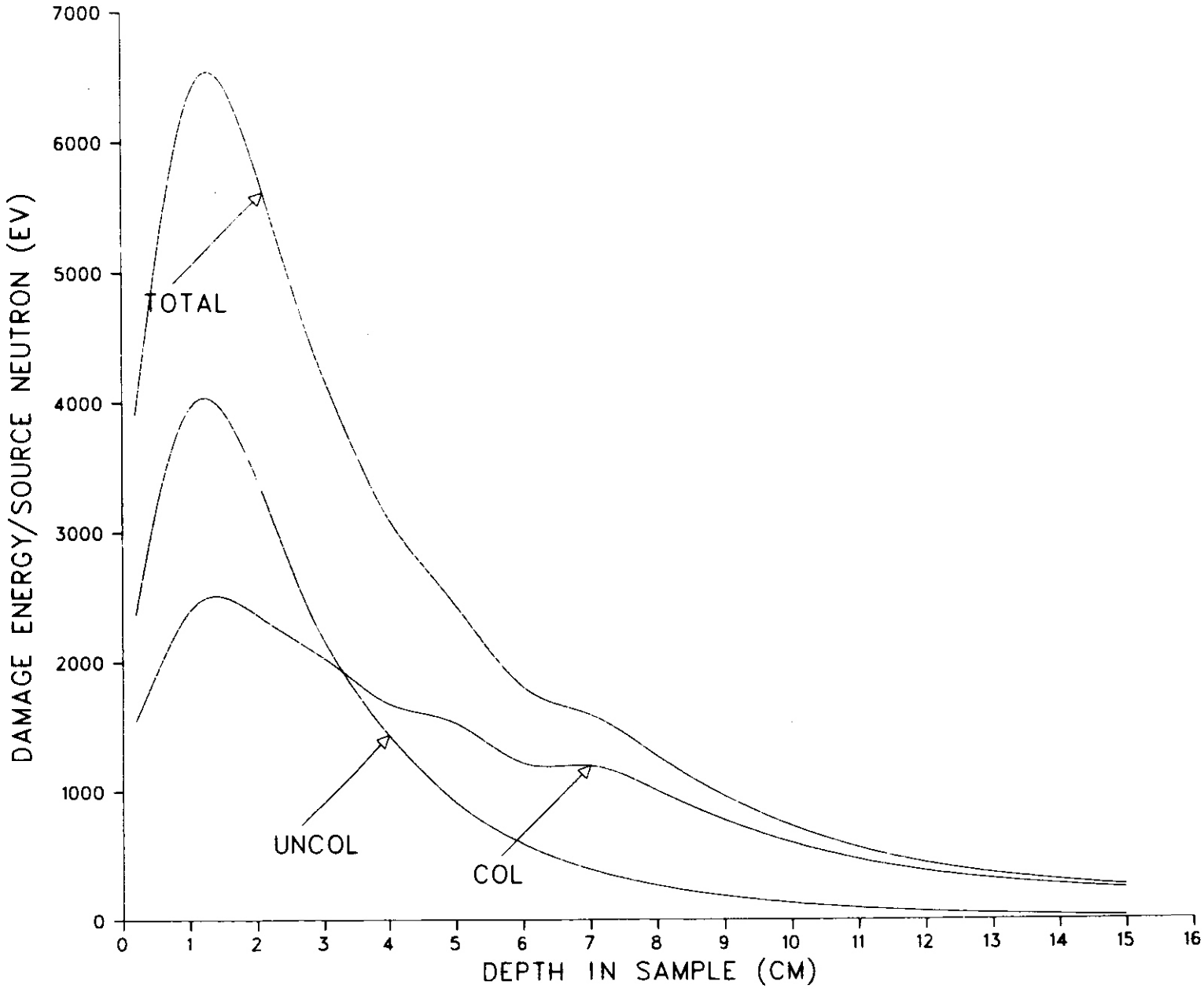

Figure 4. Dependence of Damage Energy per Incident Neutron upon the Depth in a 30x20x20 cm^3 Block of Iron Located in an Irradiation Cave Having walls of High Density Concrete

I. PROGRAM

Title: Irradistion Effects Analysis (WH011)
Principal Investigator: D. G. Doran
Affiliation: Hanford Engineering Development Laboratory

II OBJECTIVE

The objective of this work is to predict the spatial variations of radiation damage parameters within the test volume of the Fusion Materials Irradiation Test (FMIT) facility, and the sensitivity of these parameters to cross section and spectrum uncertainties.

III. RELEVANT DAFS PROGRAM PLAN TASK/SUBTASK

SUBTASK II.A.2.4 Flux Spectrum Definition in FMIT
SUBTASK II.B.1.5 Calculation of Displacement Cross Sections

IV. SUMMARY

The microscopic neutron yield model used in the perturbed and unperturbed flux and spectrum calculations has been improved to better agree with measured spectral shapes, as well as with recently obtained data from a HEDL-UC Davis d-Li neutron yield experiment. As a result, the spatial variations in damage parameters are much greater than those presented previously.

V. ACCOMPLISHMENTS AND STATUS

A. FMIT Damage Parameter Sensitivity Study - J. O. Schiffgens, R. L. Simons, F. M. Mann, and L. L. Carter.

1. Results

In order to provide guidance for facility design, an FMIT damage parameter sensitivity study is in progress. This report reviews the status of efforts aimed at improving the modeling codes used to predict neutron spectra and flux maps within the irradiation cell.

The microscopic neutron yield model used in the unperturbed flux and spectrum calculations of Mann[1,2] and as the source term in the perturbed and unperturbed flux and spectrum calculations of Carter[2] has been improved to better agree with measured spectral shapes, as well as with recently obtained data from a HEDL-UC Davis d-Li neutron yield experiment. By fitting to the ORNL time-of-flight data rather than using the ORNL dosimetrv-weiohted results.[3] the aqreement between calculated and measured neutron yields, integrated over energies greater than 2 MeV, is better than 30 percent at most of the angles considered by ORNL (E_d = 40 MeV) and HEDL (E_d = 35 MeV).

Figure 1 shows spectra with the improved model, for a deuteron energy of 35 MeV, at two positions in the irradiation cell, where the origin of the coordinate system is at the center of the back surface of the source. The spectra at these positions represent approximately the hardest and softest spectra in the test region for which the flux is greater than 10^{14} n/cm^2·s. Note that the neutron flux below 2 MeV is allowed to follow the evaporation model to zero. Note also that, whereas previous calculations were for uniform and gaussian sources 10 cm wide, these calculations are for a uniform 3 cm wide source. Preparations are in progress to make detailed yield measurements in the neutron energy regime below 2 MeV to better fix the low energy components of the spectra and more accurately determine the total yields.

Some spectral-averaged damage parameters calculated with the improved yield model are presented in Table 1. The significant result is that the spatial variations in the damage parameters are much greater than

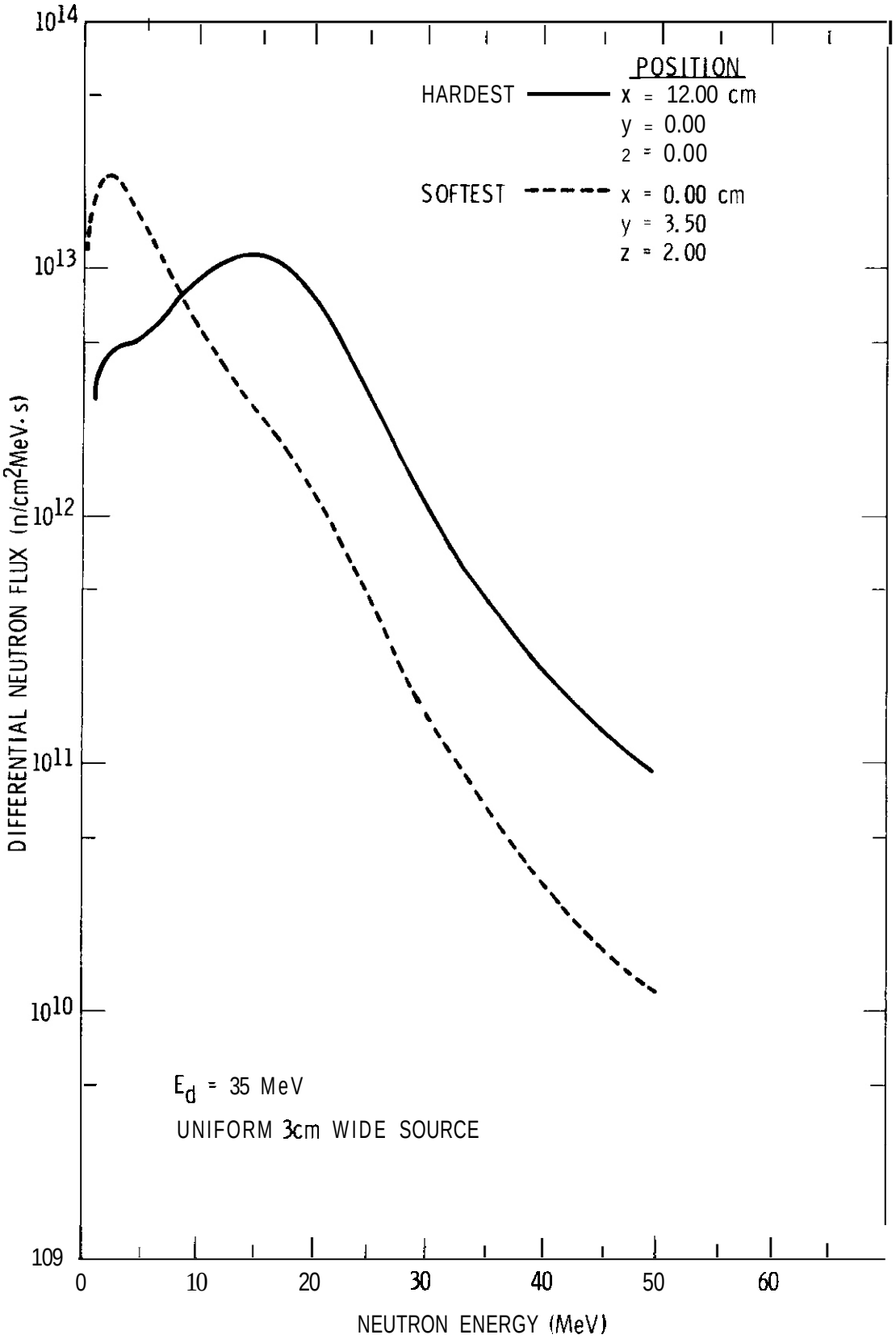

Figure 1 Calculated Neutron Spectra at Two Positions Within the FMIT Irradiation Cell.

HFDL 7810-148.1

TABLE 1

SPECTRAL-AVERAGED DAMAGE PARAMETERS FOR Cu AND Nb
3 CM WIDE UNIFORM SOURCE, E_d = 35 MeV

					COPPER			NIOBIUM		
No.	Position x (cm)	y	z	ϕ (10^{14}n/cm^2-s)	E_n (MeV)	σ_{disp} (10^3b)	σ_{He} (b)	appm He/dpa	sp b)	σ_{He} (10^{-3}b)	appm He/dpa)
1	0	0	0	27.0	12.4	3.38	.0672	19.9	2	8.59	5.64
2	0	3	0	2.31	6.62	2.27	.0292	12.9	2	2.95	2.89
3	6	0	0	.9	14.1	3.71	.0788	21.2		10.4	6.22
4	6	0	0	.1	11.2	3.15	.0591	18.8		7.38	5.20
5	6	6	0	.47	8.35	2.60	.0406	15.6		4.63	3.95
6	12	0	0	.02	14.3	3.75	.0802	21.4		10.6	6.28
7	12	3	0	.35	11.0	3.11	.0579	18.6		7.13	5.13
8	6	0	2	.55	11.9	3.29	.0639	19.4	8	8.07	5.46
9	6	3	2	.786	10.2	2.96	.0525	17.8	3	6.39	4.80
10	6	6	2	.384	8.16	2.57	.0383	15.3	5	4.44	3.85
11	12	0	2.5	.732	12.8	3.47	.0702	20.2	6	9.03	5.78
12	12	5	2.5	.238	10.5	3.02	.0548	18.1	6	6.73	4.95
13	6	0	2	.40	7.21	2.38	.0330	13.8	7	3.50	3.26
14	0	3.5	2	.71	6.37	2.22	.0275	12.4		2.71	2.71
15	0	7	2	.52	6.00	2.14	.0251	11.7		2.39	2.47

those presented previously.[3,4]) For example, while the spectral-averaged helium-to-dpa ratios for copper and niobium were previously calculated to vary by less than 7 and 11 percent, respectively, current calculations predict variations as large as 85 and 150 percent.

In addition, work is continuing on the Monte Carlo model which is to be used to generate unperturbed and perturbed neutron spectra and flux maps throughout the irradiation cell. With thismodel, spatial detail is obtained by tallying the scalar flux on small surface elements and using an interpolation scheme in an auxiliary program to determine the flux at any point within the empty or assembly-filled test region. The energy dependence of the flux is calculated in a similar manner except that a coarser mesh of surface elements is necessary in order to obtain acceptable statistical precision with a reasonable expenditure of computer resources. In the calculations reported previously, however, the mesh for, the energy dependence was too coarse and this led to some downshift in the predicted spectra. A technique is now being incorporated which will provide flexibility in the choice of an adequate grid for the neutron energy dependence.

VI. REFERENCES

1. J. O. Schiffgens, R. L. Simons and F. M. Mann, Damage Analysis and Fundamental Studies Quarterly Technical Progress Report, January - March 1978, DOE/ET-0065/1, p. 43.

2. J. O. Schiffgens, R. L. Simons, F. M. Mann and L. L. Carter, Damage Analysis and Fundamental Studies Quarterly Technical Progress Report, April - June 1978, p. 39.

3. M. J. Saltmarsh, C. A. Ludeman, C. B. Fuller and R. C. Styles, "Neutron Yields and Dosimetry for Be(d,n) and Li(d,n) Neutron Sources at E_d = 40 MeV," NBSIR 77-1279, 24, National Bureau of Standards (1977). ORNL TM-5696, Oak Ridge National Laboratory.

VII. FUTURE WORK

Calculations to define the effect of data uncertainties for FMIT will be continued, including analyses of spectral-averaged damage parameters for

stainless steel. A paper on this work will be prepared for presentation at the First Topical Meeting on Fusion Reactor Materials, Miami Beach, Florida, January 29–31, 1979.

VIII. PUBLICATIONS

None.

I. PROGRAM

Title: Dosimetry and Damage Analysis
Principal Investigator: L. R. Greenwood
Affiliation: Argonne National Laboratory

II. OBJECTIVE

To determine damage parameters and their sensitivity to uncertainties in the neutron flux-spectra in various neutron fields.

111. RELEVANT DAFS PROGRAM TASK/SUBTASK

SUBTASK 11. A.3.1 Evaluate damage parameter sensitivity to flux/spectra uncertainties.

TASK II. B.I Calculation of defect production cross sections.

IV. SUMMARY

The ANL damage cross section files have been extended to 44 MeV for copper using nuclear cross sections calculated at ORNL up to 32 MeV. Damage parameters for copper can now be computed in Be(d,n) fields up to E_d = 40 MeV with a complete error analysis due to uncertainties in the flux-spectrum from foil activation dosimetry. The copper file was further extrapolated to 100 MeV to permit calculations for spallation neutron sources. Examples are given for a dosimetry run for PNL at U. C. Davis (Be(d,n), 40 MeV) and the IPNS-I facility being designed at ANL.

V. ACCOMPLISHMENTS AND STATUS

Extrapolation of Damage Cross Sections for Copper -- L. R. Greenwood

We have previously developed the computer codes DISCS, SPECTER, and SANDANL to provide routine damage analysis for DMFE experimenters. Damage parameters such as displacements-per-atom (DPA), primary knock-on atom (PKA) distributions, and gas and transmutant production rates can be computed for 21 different elements for any neutron spectrum (E_n < 20 MeV). If we have measured the spectrum by multiple foil dosimetry, then a complete error analysis is also provided giving the errors in the damage parameters due to dosimetric uncertainties.

The major limitation of our codes at present is that neutron cross sections are unknown above 20 MeV since they are taken from ENDF/B-IV. Experimenters at Be(d,n) and spallation sources have expressed interest in extending these calculations. Consequently, we have started to extend our files.

Cross sections for copper have been calculated by C. Y. Fu and F. G. Perey[1] up to 32 MeV neutron energy. These calculations were extrapolated smoothly to 44 MeV for use at Be(d,n) sources and a few broad groups were added up to 100 MeV for spallation sources. A calculation using this data is shown for a Be(d,n) spectrum measured at E_d = 40 MeV at the U. C. Davis cyclotron for D. Styris and R. Jones (PNL), as presented elsewhere in this report. Table I gives the spectral averaged damage parameters. The results are found to agree quite well with values in the literature, except that our spectrum extends downwards to thermal energies whereas all literature calculations cut-off in the 2-4 MeV range. Damage rates, obtained by multiplying the spectral averaged quantities times the flux, do not depend on the cut-off very much since neutrons below 100 keV cause very little damage. For the data in Table I we would predict 7.9 x 10^{-9}

TABLE I: SPECTRAL AVERAGED DAMAGE PARAMETERS FOR COPPER. A LINDHARD CUT-OFF OF 40 eV WAS ASSUMED.

	Be(d,n), E_d = 40 MeV[a]	IPNS I, ANL[b]
Flux	3.53 ± 0.19 x 10^{12} n/cm^2-s	9.51 /proton
$<\sigma_D>$, b	2243 ± 81	470
$<\sigma_{DAM}>$, keV-b	224 ± 8	47
$<\sigma_H>$, mb	83.4 ± 3.4	8.2
$<\sigma_{He}>$, mb	39.4 ± 1.6	2.1
$<T_{DAM}>$, keV	69.1 ± 2.8	8.6
$<E_{RECOIL}>$, keV	116.8 ± 5.0	11.9

Primary Knock-on Atoms (PKA)

Energy, keV	% of Recoils	% of Recoils
0.04 - 0.1	0.5 ± 0.1	6.2
0.1 - 1.0	4.5 ± 1.0	29.2
1 - 5	10.9 ± 2.2	26.1
5 - 10	9.3 ± 1.3	13.2
10 - 50	29.5 ± 3.0	20.4
50 - 100	11.0 ± 0.8	2.9
100 - 200	12.5 ± 0.9	1.4
200 - 300	7.5 ± 0.4	0.3
300 - 500	8.5 ± 0.4	0.2
500 - 750	3.9 ± 0.2	0.1
750 - 1000	1.2 ± 0.1	0.05
>1 MeV	0.7 ± 0.1	0.08

[a]Spectrum measured for PNL at U. C. Davis. Errors are due to dosimetry *only* and do not include displacement cross section errors.

[b]Preliminary spectrum provided by M. Kirk (ANL).

displacements per second (6.6 x 10^{-4} total) and 1.4 x 10^{-7} appm He per second (1.2 x 10^{-2} appm He total) for copper.

Table I also includes a sample calculation for the neutron spectrum expected at the Intense Pulsed Neutron Source (IPNS I) to be built at ANL. This work was done in collaboration with M. Kirk (ANL/MSD). The calculations above 30 MeV are questionable since the cross sections are extrapolations of calculated values and neutrons above 100 MeV energy were lumped into our final group from 75-100 MeV. Nevertheless, the damage parameters are fairly reliable since less than 2% of the neutron flux or 16% of the damage is produced above 15 MeV neutron energy.

VI. REFERENCES

1. C. Y. Fu and F. G. Perey, J. Nucl. Mater. 61, 153 (1976).

VII. FUTURE WORK

We plan to include more elements in the future. Some calculations are available for niobium; however, most other elements will have to be extrapolated from the ENDF/B-IV files which end at 20 MeV. The codes can now be used to provide very accurate damage parameter sensitivity calculations using positional dosimetry data from Be(d,n) irradiations.

VIII. PUBLICATIONS

None

I. PROGRAM

Title: Synergistic Helium Production by Boron Doping of Splat Cooled Alloys

Principal Investigator: O. K. Harling

Affiliation: Nuclear Reactor Laboratory, Massachusetts Institute of Technology

11. OBJECTIVE

This work is directed toward the development of better simulation techniques for the synergistic production of helium and displacement damage in first wall structural materials.

III. RELEVANT DAFS PROGRAM PLAN TASK/SUBTASK

A number of tasks are relevant since adequate experimental simulation of fusion reactor irradiation effects is a major reason for the DAFS program. Some of the tasks/subtasks which are significantly affected are:

TASK	II.A.4	Gas Generation Rates
	II.C.2	Effects of Helium on Microstructure
	II.C.8	Effects of Helium and Displacement on Fracture
	II.C.13	Effects of Helium and Displacement on Crack Initiation and Propagation

IV. SUMMARY

During this quarter a roll quenching machine was rebuilt for use in producing larger amounts of rapidly quenched Fe-Ni-Cr alloys. Several one half-kilogram batches of rapidly solidified 316 SS were produced and some microstructurd characterization is reported here.

The neutron flux in several assemblies in the MIT Research Reactor

(MITR-II) has been measured. Results are quoted here for the flux in the so-called "Controlled Thermonuclear Reactor Facility". It is found that the flux above 1.0 Mev peaks at 5×10^{13} n/cm^2s at a position 23 cm from the bottom of the assembly and the 2200 m/s thermal flux varies between 2×10^{13} and 3×10^{13} n/cm^2s over the length of the assembly. These results indicate that the MITR-II with its easily instrumented core positions is well suited for CTR irradiation testing at low fluences.

V. ACCOMPLISHMENTS AND STATUS

A. Boron Doping of Stainless Steel by Rapid Quenching - S. West, G. Dansfield, O. Harling, and K. Russell (M. I. T.)

1. Introduction

It is generally understood that existing irradiation facilities, i.e. accelerators and fission reactors, will have to be used for the initial irradiation testing of fusion reactor (FR) structural materials. Damage rates and helium production rates should simulate the expected rates in FR's. Only fission reactors offer the required large testing volumes with fast neutron fluxes which produce damage rates which equal or exceed those expected for near term FR's. Helium production rates, with the exception of nickel alloys in mixed spectrum reactors, cannot be reproduced by direct nuclear reaction on the alloy constituents. The present studies are directed toward the development of techniques for the production of helium during fission reactor irradiations. Current efforts emphasize the doping of structural alloys with boron. To assure the uniform distribution of boron, the alloy is produced by rapid quenching from the melt. Cooling rates of 10^5 - 10^9°C/sec offer the possibility of uniform boron concentrations which are much higher than those which can be maintained without segregation during normal solidification rates. The usefulness of this approach to boron doping will also depend upon the maintenance of a uniform boron distribution during thermo-mechanical consolidation, and during the use of the consolidated material in the temperature. stress and radiation environment of the fission reactor. Further-

more, the effect of boron on the physical properties of the boron doped alloys, whether segregated to grain boundaries or uniformly distributed must be understood.

This quarterly report deals with our efforts to produce rapidly quenched alloys containing homogeneously distributed boron and summarizes the status of our work to characterize the neutron radiation fields of the MITR-II, which will be used for low fluence testing of the boron doped alloys.

2. Production of Rapidly Quenched Alloys Doped with Boron

A method of characterizing the boron distribution in stainless steel[illegible]) has been previously reported. The resolution of this technique is about 0.3 μm, making it useful for grain sizes below 2 μm. When greater resolution is required, high resolution auger electron spectroscopy will be examined. This equipment is now operating at MIT. For the techniques developed to be useful in fusion reactor materials testing, it must be demonstrated that reasonable quantities of uniform material can be produced. The primary emphasis in this area over the last quarter has been on the production of rapidly quenched alloys.

Previous work with boron doped alloys has centered on piston and anvil type splats. This method was useful because it provided a variety of cooling rates within each sample, simplifying sample preparation. However, the piston and anvil method quenches material one drop at a time. This makes it impractical for the quantity of material needed for conventional mechanical property tests. Also, the consolidated product will not be uniform. To produce large quantities of splatted material, roll quenching was investigated.

A roll quenching device was rebuilt to develop the capability of producing kilogram amounts of splatted material. The machine consists of two high-speed rolls with high thermal conductivity, through

which molten material passes and becomes solidified. Two batches of splats were made to investigate the properties of roll quenched material. Each consisted of one-half kilogram of type 316 stainless steel. The initial results are shown in Figures 1 and 2. Both figures are from the second batch of splats, and show a polished and etched surface in the rolling plane. Figure 1 is an optical micrograph from sample F1, while Figure 2 corresponds to sample F2. Both splatted foils were 0.004" thick but the microstructures are not the same. Figure 2 shows a dendritic structure with an average dendrite spacing of about 5 μm. Figure 1 shows a much larger dendritic spacing with a subgrain structure present in the dendrites. The obvious explanation for the difference is that sample F1 cooled much slower than F2. The machine is being further modified to improve cooling uniformity.

3. Neutron Flux Characterization in the MITR-II

The redesign of the MIT Research Reactor (MITR-II) was completed in 1976[2,3]. Since that time, there has been a growing interest in the development of materials testing and radiation damage capabilities to be used in conjunction with the reactor facilities currently available. Towards this end, flux measurements have been made in the central in-core irradiation facilities of the MITR-II. Before discussing these flux measurements, a brief description of the MITR-II core will be given.

When fully loaded, the MITR-II core consists of 27 fuel elements. These fuel elements have an active fuel length of 23 in. and are rhomboidal in shape (2.405 in. x 2.405 in. across the flats). Each element comprises 15 finned fuel plates consisting of Al-35 w/o U (93% enriched) fuel clad in aluminum. These elements are hexagonally arranged in three rings (A-center, B-middle, C-outside). Operating at a full power level of 5 MW_{th}, the core is light-water cooled and is surrounded by a heavy-water reflector so that the thermal flux peaks beneath the core (providing high thermal fluxes for beam port experiments) and the

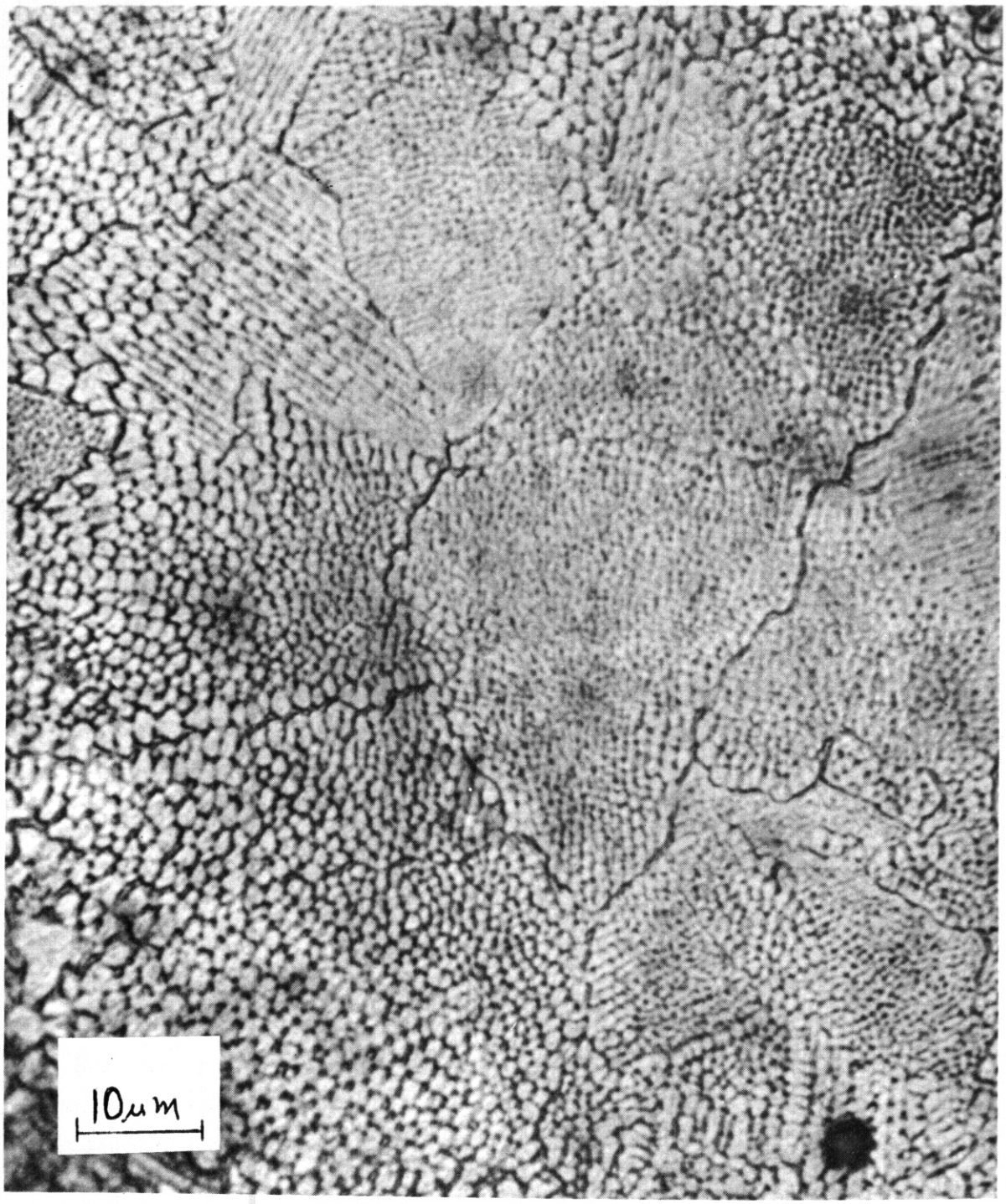

FIGURE 1. Optical Micrograph of Splat Cooled Type 316 Stainless Steel. The Figure Shows a Subgrain Structure Within the Dendrites of Sample F1 (Kalling's Reagent, 2000x).

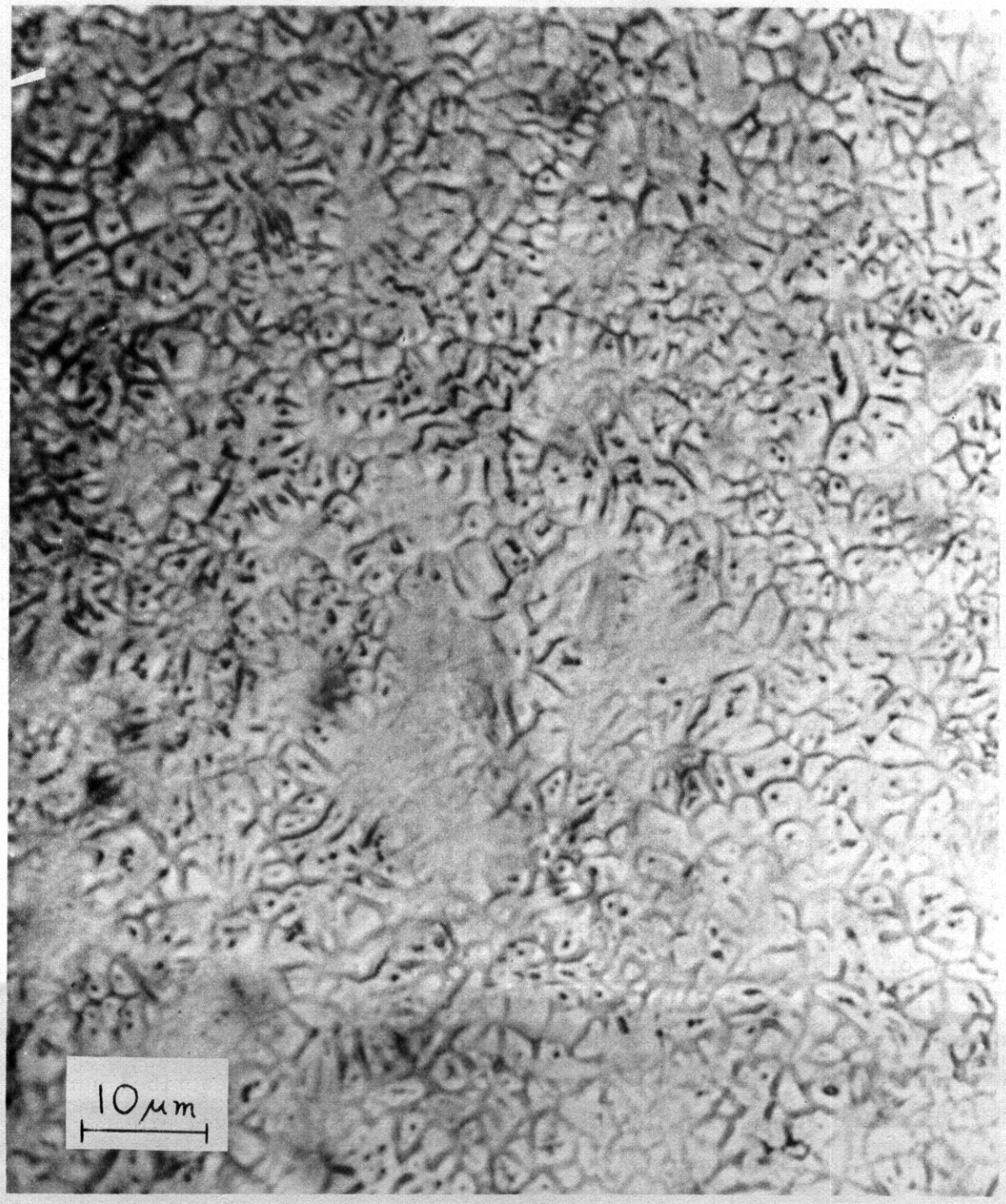

FIGURE 2. Optical Micrograph of Splat Cooled Type 316 Stainless Steel. The Figure Shows an Average Dendrite Spacing of About 5 μm In Sample F2 (Kalling's Reagent, 2000x).

neutron flux spectrum within the core is highly undermoderated. Three or four fuel assemblies can be replaced with solid aluminum dummy elements or materials irradiation facilities. A relatively large and flexible irradiation volume (approximately 0.5 l /element) is thus available for various types of radiation damage studies and general use. Easy access to these irradiation facilities is provided by aluminum thimbles which extend from the reactor top to the bottom of the core, passing though the coolant water above the core. The assemblies of greatest interest for radiation damage projects are located in the A-ring. Of the A-ring facilities, an in-core sample assembly [which has been dubbed the "Controlled Thermonuclear Reactor Facility" (CTRF)] will be used for several fusion reactor related irradiation experiments in the near future. It is for this facility that the flux spectrum results in this study are presented. (Additional flux data for A-ring facilities can be found in Reference 4.) The CTRF houses an aluminum thimble (as described above) which has an inside diameter of 1.134 in. and which facilitates the insertion and removal of irradiation specimens and the handling of thermocouples and other instrumentation in this facility. Since this facility can be made vacuum tight, irradiations in the CTRF can be conducted in an inert gas atmosphere and the temperature can be controlled accurately by regulating the gas flow within the thimble[5].

Five reactions were used to measure the flux over the length of the CTRF extending from the reactor bottom to a position approximately 4 cm above the top of the active core. The reactions and cross sections used are shown in Table 1. (Details of the flux measuring experiments can be found elsewhere[4] and so will not be described here.) For the calculations done in this study, the fission averaged cross section $\bar{\sigma}_f$ was defined as

$$\bar{\sigma}_f \equiv \frac{\int_0^\infty \sigma(E)\ \phi_f(E)\ dE}{\int_0^\infty \phi_f(E)\ dE}$$

where $\phi_f(E)$ is the fission spectrum. The effective spectrum averaged

TABLE 1. CROSS SECTIONS USED IN FLUX MEASUREMENTS

Fission Averaged and Spectrum Averaged Cross Sections

Reaction	E_i (Mev)	$\bar{\sigma}_f$ (mb)	$\bar{\sigma}_{Ei}$ (mb)	Notes
$^{58}Ni(n,p)^{58}Co$	1.0	31	46.2	(to ^{58m}Co)
	1.0	61	90.0	(to ^{58m}Co)
$^{54}Fe(n,p)^{54}Mn$	1.5	68	134	
$^{60}Ni(n,p)^{60}Co$	4.0	2.4	23.4	(total to ^{60m}Co and ^{60}Co)
$^{63}Cu(n,\alpha)^{60}Co$	6.0	0.45	17.6	(total to ^{60m}Co and ^{60}Co)

Thermal Cross Sections

Reaction	σ_{2200} (b)
$^{54}Mn(n,\gamma)$	<30
$^{58m}Co(n,\gamma)$	1.4×10^5
$^{58}Co(n,\gamma)$	1650
$^{59}Co(n,\gamma)$	37.3
$^{60m}Co(n,\gamma)$	100
$^{60}Co(n,\gamma)$	6

cross section was defined slightly differently, i.e.

$$\bar{\sigma}_{Ei} \equiv \frac{\int_0^\infty \sigma(E)\ \phi(E)\ dE}{\int_{Ei}^\infty \phi(E)\ dE}$$

where E_i is the effective threshold energy and $\phi(E)$ is the differential neutron flux (in this case taken to be the fission spectrum). The results of these fast and thermal flux measurements are shown in Figures 3 and 4. The flux above 1.0 Mev rises and falls gradually, peaking at a position approximately 27 cm above the bottom of the CTRF. The behavior of the thermal flux, on the other hand, is more complex because of the flux peaking beneath the core as mentioned above. It should also be noted that an absolute measurement of the thermal flux was not made in the CTRF; rather the flux was calculated from the measured total reaction rate in the ^{59}Co thermal flux monitor, and from the ratio of the thermal to epithermal flux as calculated by CITATION[6]. (CITATION is a reactor physics code used by the Operations Staff of the MITR-II to calculate the neutron flux and power peaking factors for various operating core configurations.) Agreement between the thermal flux as calculated from the measured total reaction rate and as calculated by CITATION is only fair, the differences becoming as large as 25% at a distance 34 cm above the bottom of the assembly. The reason for this discrepancy is not clear at this time, necessitating an absolute measurement of the thermal flux in the future to resolve this question.

Prior to the measurements in the CTRF, considerable confidence in the experimental techniques used in this study was established by an experiment run in the MITR-II A-ring facility known as the "Steel Irradiation Facility" (SIF). Fast and thermal flux measurements in this facility were made independently but concurrently with flux measurements sponsored by Dr. Henry Watson of the Naval Research Laboratory (NRL). The results of these measurements indicated close agreement (better than 10% for all reactions used) of the data from this work and from NRL. (Details of this experiment are available in Reference 4).

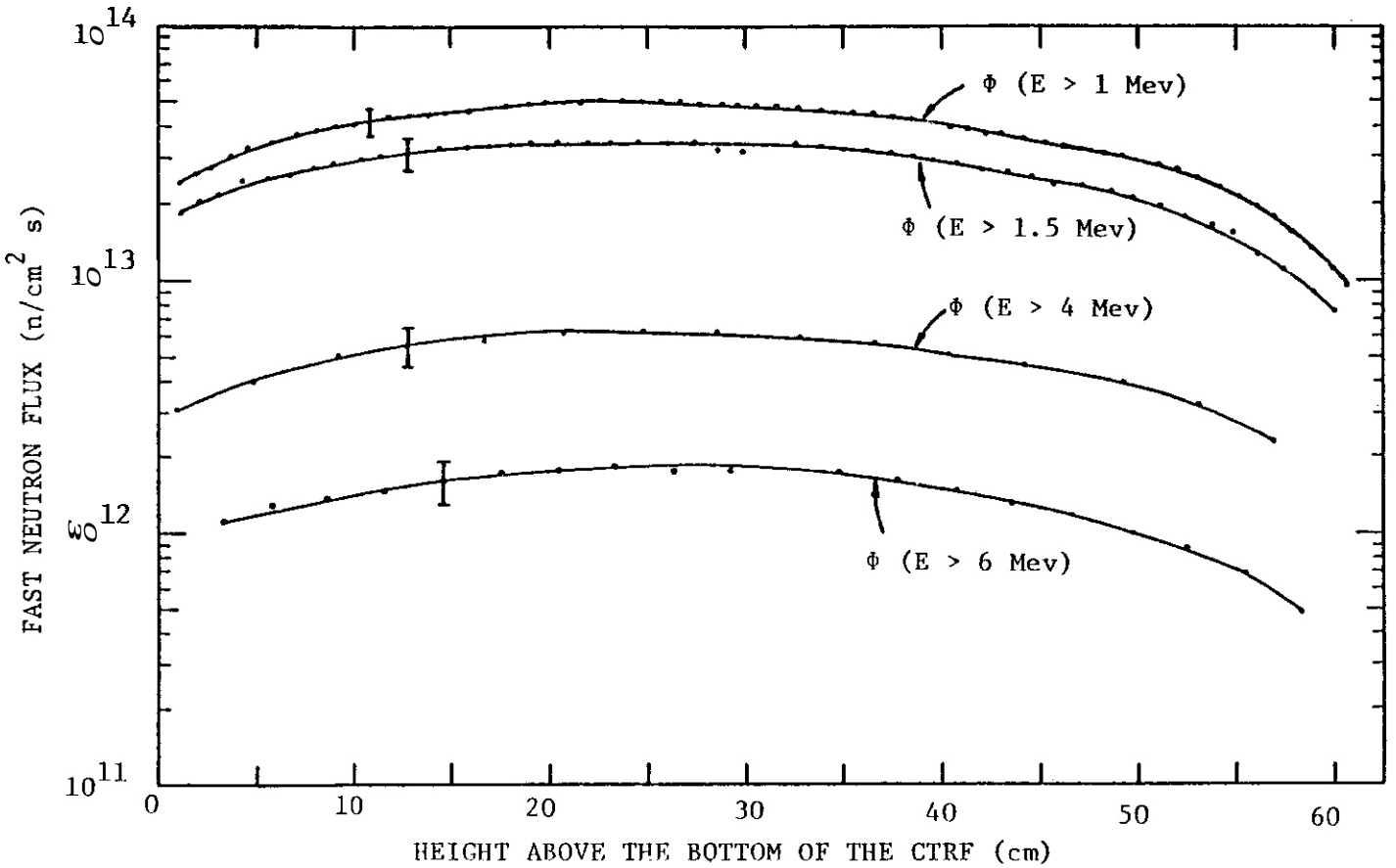

FIGURE 3 Neutron Flux in the CTRF.

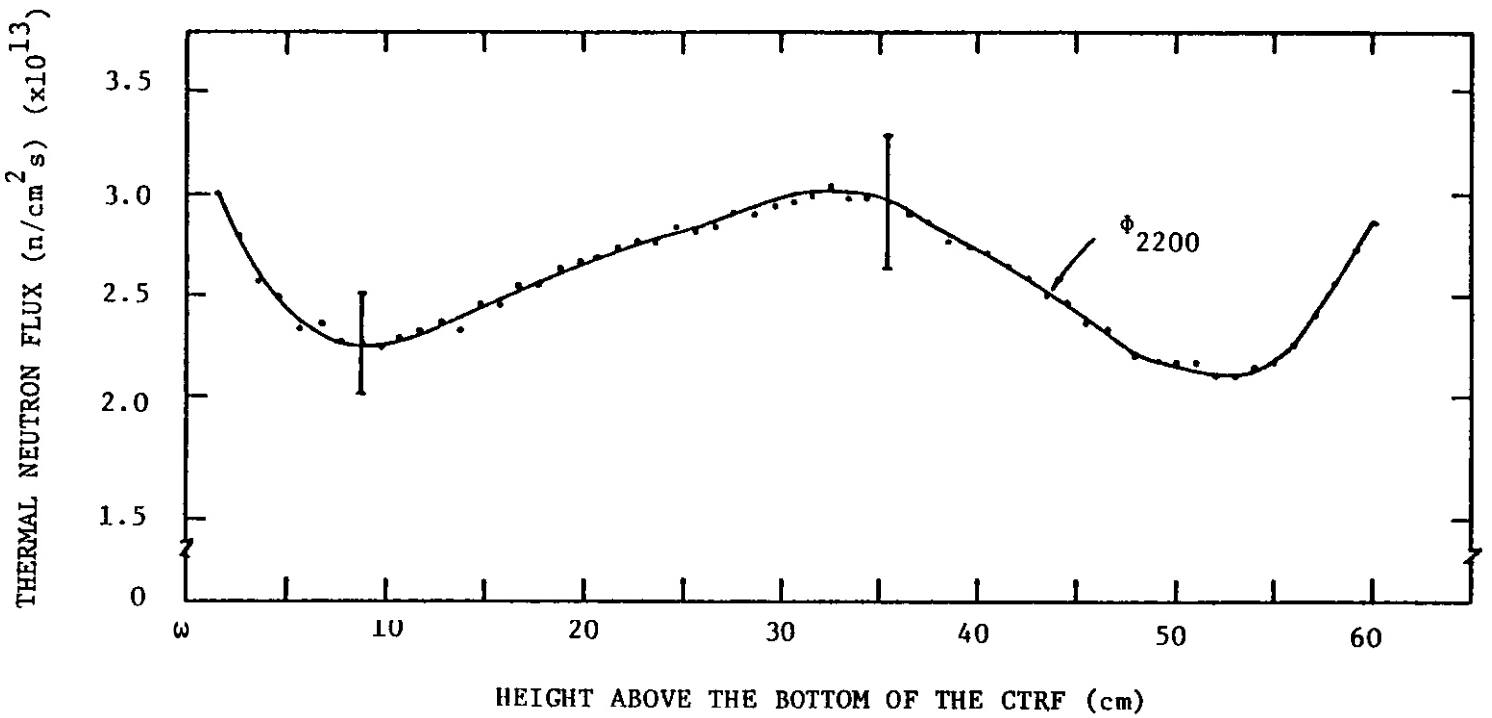

FIGURE 4 2200 n/s Thermal Neutron Flux in the CTRF.

VI. REFERENCES

1. A. Fadaai, "Determination of the 3-D Boron Distribution," A Thesis submitted in partial fulfillment of the requirements for a M.S. in Nuclear Engineering at the Massachusetts Institute of Technology, June 1978.

2. G. C. Allen, "The Reactor Engineering of the MITR-II Construction and Startup," Ph.D. Thesis, Massachusetts Institute of Technology, Department of Nuclear Engineering, MITNE-186 (1976).

3. P. C. Meagher and D. D. Lanning, "Design of Central Irradiation Facilities for the MITR-II Research Reactor," M.S. Thesis, Massachusetts Institute of Technology, Department of Nuclear Engineering, MITNE-190 (1976).

4. S. E. West, "Characterization of the MIT Research Reactor for Fusion Reactor Related Studies," M.S. Thesis, Massachusetts Institute of Technology, Department of Nuclear Engineering (To be published).

5. E. G. Daxon, "Irradiation Damage Studies of AISI Type 316 Stainless Steel,'' M.S. Thesis, Massachusetts Institute of Technology, Department of Nuclear Engineering (1978).

6. T. B. Fowler, D. R. Vondy, and G. W. Cunningham, "Nuclear Reactor Core Analysis Code: CITATION," ORNL-TM-2496 (Revision 2, 1971).

VII. FUTURE WORK (Near Term)

Future improvements are planned for the roll quench apparatus. This will be followed by production of boron doped 316 SS and characterization of the boron distribution with neutron autoradiography and scanning high resolution auger spectroscopy.

An optimum mechanical property test will be designed to determine the effects of boron in the boron doped alloys.

Displacement damage rates and helium generation rates for MITR-II will be calculated using the fast neutron flux profiles reported here.

I. PROGRAM

Title: Dosimetry and Damage Analysis
Principal Investigator: L. R. Greenwood
Affiliation: Argonne National Laboratory

II. OBJECTIVE

To establish standardized dosimetry data and procedures in order to reduce uncertainties in damage analysis and correlation studies.

III. RELEVANT DAFS PROGRAM TASK/SUBTASK

TASK II. A6 Dosimetry Standardization

IV. SUMMARY

An ANL Fusion Power Program Technical Memorandum has been completed entitled, "Extrapolated Neutron Activation Cross Sections for Dosimetry to 44 MeV". The report lists and plots 31 activation cross-sections. All cross-sections have been integrally tested in Be(d,n) fields and 25 are recommended for routine dosimetry.

A recommended practice entitled, "Procedures for Conducting Irradiations at Accelerator-Based Neutron Sources", has been revised by Task Group B of Committee E 10.08 of the ASTM.

V. ACCOMPLISHMENTS AND STATUS

1. Dosimetry Cross Section File -- L. R. Greenwood

As part of our program to integrally test dosimetry cross sections, a file of 31 activation cross-sections has been extended to 44 MeV for

Be(d,n) irradiations. An ANL Fusion Power Program Technical Memorandum has been written listing and plotting the cross sections.[1] The report also summarizes all of our integral testing,[2] as shown in Table I. Results from Be(d,n) experiments at E_d = 14, 16, and 40 MeV are listed along with the 90% energy sensitivity limits. As can be seen, 25 of the cross sections are integrally accurate to within ± 10% and should be adequate for most fusion materials irradiations. Nevertheless, it should be emphasized that the cross sections are only intended for this specific application and may have very large errors at high energies. Of course, it is hoped that further testing as well as new measurements and calculations will further reduce the errors. Meanwhile, these cross sections should permit spectral unfolding with 10-30% uncertainty in the 2-30 MeV energy range where most materials damage is produced in Be(d,n) fields. Furthermore, damage parameters can then be computed with only 5-10% errors since they are integral quantities. A paper reviewing this work will be presented at the Fusion Reactor Materials Meeting in Miami Beach in January.

2. ASTM Recommended Procedures for Accelerator Irradiation -- L. R. Greenwood

The recommended ASTM practice entitled "Procedures for Conducting Irradiations at Accelerator-Based Neutron Sources" was revised during the recent ASTM meeting at Richland, Washington, in July. This report was revised by Task Group B of Committee E 10.08, with L. Greenwood (Chairman), M. Guinan (LLL), H. Farrar (AI), R. Gold (HEDL), and D. Dierckx (LASL) in attendance. It is hoped that these recommendations will help to standardize accelerator irradiations so that damage parameters may be accurately calculated and data correlated. Copies have been circulated to interested parties for comment prior to formal ASTM review.

Table I - Integral Cross Section Tests. Cross-section errors (%) and the 90% energy sensitivity limits[a] are listed. Relative errors are ±2% and absolute errors are ±10%, except as noted.

Reaction	E_d = 14.1 MeV 90% limits[a] (MeV)	Error (%)	E_d = 40 MeV 90% limits[a] (MeV)	Error (%)
$^{45}Sc(n,\gamma)^{46}Sc$[b]	0.15 - 11.5	+3	7.6^{-3} - 25.0	-7
$^{59}Co(n,\gamma)^{60}Co$[b]	0.21 - 10.7	-3 ± 15	1.6^{-4} - 22.7	-5 ± 10
$^{197}Au(n,\gamma)^{198}Au$[b]	0.31 - 9.7	-3	2.5^{-4} - 19.5	+0
$^{238}U(n,\gamma)^{239}Np$[b]	0.19 - 5.7	-4	4.3^{-4} - 4.2	+8
$^{235}U(n,f)$	0.8 - 13.1	+7	0.6 - 29.7	+1
$^{238}U(n,f)$	2.0 - 13.2	+4	5.0 - 30.8	-1
$^{115}In(n,n')^{115m}In$	1.2 - 10.3	-1	1.8 - 23.1	-3
$Ti(n,p)^{46}Sc$	5.1 - 13.9	-7	9.0 - 33.0	-89 (+14)[c]
$Ti(n,p)^{47}Sc$	3.1 - 13.0	+2 (+12)[c]	12.0 - 33.0	-798 (+15)[c]
$^{48}Ti(n,p)^{48}Sc$	7.1 - 15.6	-7	9.9 - 26.2	+2
$Fe(n,p)^{54}Mn$	3.7 - 12.5	+6	6.0 - 33.0	-88 (+1)[c]
$^{56}Fe(n,p)^{56}Mn$	2.4 - 14.5	-2	8.6 - 23.5	-4
$^{59}Co(n,p)^{59}Fe$	5.1 - 14.3	-8	8.1 - 24.2	+8 ±15
$^{58}Ni(n,p)^{58}Co$	3.5 - 12.4	+0	4.4 - 23.4	+9
$^{60}Ni(n,p)^{60}Co$	6.2 - 13.7	+14	7.9 - 23.0	+3 ±6
$^{27}Al(n,\alpha)^{24}Na$	7.4 - 14.2	+3	9.0 - 21.5	+0
$^{45}Sc(n,\alpha)^{42}K$	2.0 - 15.5	-15	—	—
$^{54}Fe(n,\alpha)^{51}Cr$	6.4 - 15.3	-4	9.5 - 28.0	-36

Table I (cont'd)

$^{59}Co(n,\alpha)^{56}Mn$	7.1	- 15.0	-4	9.3	- 24.0	-4
$^{45}Sc(n,2n)^{44m}Sc$	12.6	- 19.0	-14	13.9	- 27.5	-1
$^{58}Ni(n,2n)^{57}Ni$	13.3	- 19.4	+10(-11)[d]	14.8	- 28.2	+14(-30)[d]
$^{59}Co(n,2n)^{58}Co$	11.5	- 18.4	+1	12.8	- 26.6	-9
$^{59}Co(n,3n)^{57}Co$		—	—	22.0	- 36.0	-28 ± 15
$Zr(n,2n)^{89}Zr$	12.6	- 18.2	+13	14.1	- 28.1	-4
$^{93}Nb(n,2n)^{92m}Nb$	9.9	- 18.3	+7	11.2	- 22.0	+6
$^{169}Tm(n,2n)^{168}Tm$		—	—	10.4	- 23.3	+7
$^{169}Tm(n,3n)^{167}Tm$		—	—	17.9	- 30.6	-9
$^{197}Au(n,2n)^{196}Au$	8.3	- 16.2	-9	10.7	- 28.5	-1
$^{197}Au(n,3n)^{195}Au$		—	—	18.0	- 28.4	+2 ± 6
$^{197}Au(n,4n)^{194}Au$		—	—	27.2	- 38.3	+1 ± 11
$^{238}U(n,2n)^{237}U$	5.[illegible]	2 - 13.0	+4	7.7	- 18.0	-11

[a] 90% of the activation integral is contained in this energy range $\sim 6^{-8}$ meV $\sim 6 \times 10^{-8}$

[b] (n,γ) ratios have a ±15% uncertainty since the TOF data stops at 0.8 - 2 MeV

[c] The value in parenthesis includes the THRESH calculations for higher mass isotopes

[d] The value in parenthesis is for the ENDF/B-IV cross section

VI. REFERENCES

1. L. R. Greenwood, "Extrapolation of Neutron Activation Cross Sections for Dosimetry to 44 MeV," Argonne National Laboratories Report ANL-FPP-TM-115, November 1978.

2. L. R. Greenwood, R. R. Heinrich, R. J. Kennerley, and R. Medrzychowski, "Development and Testing of Neutron Dosimetry Techniques for Accelerator-Based Irradiation Facilities," accepted for publication in Nuclear Technology.

VII. FUTURE WORK

Further integral testing is now being planned and it is hoped that new experiments and calculations will continue to improve the nuclear data base.

VIII. PUBLICATIONS

See Part VI.

CHAPTER 4

SUBTASK B: DAMAGE PRODUCTION

I. PROGRAM

Title: Radiation Damage Analysis and Computer Simulation
Principal Investigator: Don M. Parkin
Affiliation: Los Alamos Scientific Laboratory of the University of California

II. OBJECTIVE

The objective of this work is to develop displacement functions for polyatomic materials.

III. RELEVANT DAFS PROGRAM PLAN TASK/SUBTASK

SUBTASK	II.B.2.3	Cascade Production Methodology
	II.B.4.1	Interface with other designs and other tasks
	II.B.4.2	Develop theory of spectral and rate effects

IV. SUMMARY

The computer program DISPLC which calculates displacement functions in single element and polyatomic materials[1] has been used to study the basic behavior of displacement cascades in polyatomic materials. One of several important features that significantly effect the displacement process in polyatomic materials is discussed in this report. Effects due to displacement and capture threshold energies are observable at much higher energies in polyatomic materials than in single element materials.

V. ACCOMPLISHMENTS AND STATUS

A. Displacement Functions for Multicomponent Systems --

D. M. Parkin (LASL) and C. A. Coulter (The University of Alabama)

1. Results

Displacement cascades in polyatomic materials are subject to factors that are not present in monatomic cascades. Conditions such as different threshold energies for each element in the material, capture threshold energies for unlike atoms that differ from the displacement thresholds and large differences in mass among the constituents lead to significant changes in cascade behavior relative to the monatomic case. One characteristic behavior which is related to mass difference and the displacement threshold energy is described in this report.

The total displacement function, n_{ij}, assuming a displacement threshold energy of E_i^d = 60 eV was calculated for TaO. Results for the distribution of Ta and O displacements as a function of Ta and O recoil energies are given in Table I. Below the threshold energy for atom i

TABLE I.
FRACTION OF TYPE j DISPLACEMENTS PRODUCED BY AN INITIAL RECOIL ATOM OF TYPE i IN TaO

Energy (eV)	Ta Recoil		O Recoil	
	Ta → Ta	Ta → O	O → Ta	O → O
	%	%	%	%
100	100	0.0	0.0	100
225	99.5	0.5	0.6	99.4
544	88.5	11.5	15.1	84.9
1.02×10^3	80.8	19.2	26.4	73.6
2.46×10^3	73.8	26.2	37.8	62.2
5.24×10^3	69.6	30.4	45.7	54.3
1.12×10^4	66.8	33.2	51.5	48.5
1.07×10^5	63.3	36.7	61.3	38.7
1.03×10^6	62.8	37.2	64.3	35.7
1.00×10^7	62.9	37.1	65.4	34.6

producing a j displacement, 201 eV for this case, only i type displacements are possible. For primary recoil energies above this indirect threshold displacements on both sublattices occur.

As the recoil energy increases from the threshold region, the distribution of displacements on the two sublattices approaches a set of equilibrium values. The displacement distribution is dominated by the type of primary recoil atom at the lower energies. At low energy the energy transfer efficiency, $m_1 m_2/(m_1 + m_2)^2$, favors energy transfer to the sublattice corresponding to the recoil atom. Hence at low energies, the displacement distribution is controlled by the primary recoil atom type. At higher energies, the displacement distribution becomes nearly independent of the primary recoil atom type. Once the primary recoil atom can transfer significant amounts of energy to either sublattice, the displacement distribution is determined by the properties of the matrix in total and it loses its dependence on the primary recoil atom type.

The recoil energy range over which the displacement distribution is dependent on the primary recoil energy type is significant when one considers the characteristic recoil energies for charged particle, fission reactor and fusion reactor irradiations. For ceramics, one of the most important parameters is the displacement distribution. Because of this recoil energy dependence, the displacement distributions will be related to the relative scattering cross sections of the constituents in a more complicated way.

Once an equilibrium distribution is reached, the number of heavy element displacements is greater than for the light element. This distribution occurs in the case of equal displacement threshold energies because in the LSS theory, which is used in the calculations, it is more damage energy and displacement efficient to transfer energy to the heavier atoms.

VI. REFERENCE

1. Don M. Parkin, "Radiation Damage Analysis" in First Damage Analysis and Fundamental Studies Quarterly Progress Report, unpublished.

VII. FUTURE WORK

Future work will focus on analyzing polyatomic displacement cascades and obtaining analytical formulas for the calculated displacement functions.

I. PROGRAM

Title: Irradiation Effects Analysis (WH011)
Principal Investigator: D. G. Doran
Affiliation: Hanford Engineering Development Laboratory

II. OBJECTIVE

The objective of this work is to establish computer models for the simulation of the low energy aspects of radiation damage in order to provide a basis for the development of computer models for the simulation of high energy cascades.

III. RELEVANT OAFS PROGRAM PLAN TASK/SUBTASK

SUBTASK II.B.2.3 Cascade Production Methodology

IV. SUMMARY

A methodology is presented for the computer simulation of low energy radiation damage experiments using the quasi-dynamical computer code ADDES. The systematic procedures for selection of an interatomic potential and optimization of the code parameters are discussed. The types of experiments which may easily be simulated with ADDES are indicated, with particular attention to a simulation of forward sputtering experiments which is now in progress.

V. ACCOMPLISHMENTS AND STATUS

A. A Methodology For the Computer Simulation of Low Energy Radiation Damage Experiments -- R. G. Ariyasu (Cal. State Univ. at Northridge), D. M. Schwartz (Cal. State Univ. at Northridge), and H. L. Heinisch, (HEDL)

1. Introduction

Recent advancements in both experimental techniques and computer technology have made it possible to significantly improve the range of applicability of computer modeling to studies of crystal defects. Experimentally, advances center around techniques with high levels of resolution such as high voltage/high resolution transmission electron microscopy, Auger spectroscopy, field ion microscopy, time-of-flight mass spectroscopy, and image intensification. These experimental advances have been augmented by the development of increasingly sophisticated computers capable of handling the computations necessary for simulating large-scale phenomena. Using the developments from both areas, it is now possible to more directly establish the validity of computer simulations for the meaningful investigation of fundamental mechanisms of radiation damage in crystals.

A general approach for applying the quasi-dynamical computer code ADDES[1,2] for simulating low energy radiation damage experiments will be presented here.

ADDES has been labeled "quasi-dynamical" because it integrates the equations of motion for only the atoms which are "active" relative to a threshold energy value. ADDES operates in an effectively infinite crystal of atoms interacting via pair potentials extending to second nearest neighbors. By means of the threshold condition, it generates only as much active crystal as it needs, expanding or contracting the number of active atoms under the direction of "activation" and "freezing" parameters. The parameter EM is the minimum value of total energy an atom must have before it may move from its lattice site and become an active atom. If an active atom loses energy so that its potential energy falls below a value EC and its total energy falls below a value FEM, then it is "frozen," that is, its kinetic energy is set to zero. Thus, only atoms with significant amounts of energy (as determined by the values of EM, EC, and FEM) are allowed to be active. ADDES contains a number of other adjustable parameters which must be properly set to assure the correct dynamical behavior. For example,

there are parameters which control incrementing of the time step size during the run. The most critical parameters are EM and EC.

In principle, the parameters can be set so conservatively as to render ADDES a fully dynamical code. Thus, EM, EC and FEM could be set below the value of the minimum potential energy experienced by an atom in a crystal, making them completely ineffective. However, the usefulness of the code lies in being able to ignore as many of the interactions as possible without changing the dynamics of the event in order to minimize the computer run time. In the process of optimizing the parameter settings, runs with different sets of parameters are not compared on a collision for collision basis, but rather in terms of the following quantities: displacement threshold energy, number and length of replacement sequences, energy loss per collision in replacement and focused collision sequences, Frenkel pair production and separation, and focusing energies.

ADDES has been calibrated by comparing its results with the results of the fully dynamical computer simulation code COMENT.[1] With conservative, but effective, parameter settings for ADDES, low energy primary knock-on atoms (PKAs) in copper were simulated with both codes using the same pair potential. ADDES compared favorably with COMENT with respect to the quantities listed above.

A methodology for optimization of the ADOES parameters with respect to a given simulation problem has been devised and is reported on here.

2. Methodology

There are three main parts to the methodology: choosing a potential, optimizing parameter settings, and setting the initial conditions appropriate to the experiment to be simulated.

Most of the atomic interactions of interest in these simulations can be modeled by a pair potential extending to second neighbors. There are a number of analytical forms for relatively long range, low energy empirical potentials which can be fitted to elastic constants and other experimental crystal data. There are also several accepted forms for the shorter range, high energy, screened Coulomb interactions. The potentials chosen for our simulations[2] generally are a combination of the Moliere approximation to the Thomas-Fermi potential at short range and a set of smoothly joined polynomial functions fitted to elastic data at the longer range. The polynomials are joined to the Moliere function at a separation somewhat less than the nearest neighbor distance. The screening radius of the Moliere potential is treated as an adjustable parameter.

The minimum displacement threshold energy is the primary experimental quantity to which the model is fitted. Interatomic potential sensitivity studies[2] indicate that the dynamics of low energy events are very similar for different potentials which give the same displacement threshold. The displacement threshold energy is sensitive to the potential in the region where the short range and long range portions are joined. Hence, adjustment of the screening radius, which changes the value and slope in this region, has a profound effect on the displacement threshold.

Since widely varying forms of the polynomial representation of the long range portion of the potential may be equally well fitted to the elastic data, it is possible to change the displacement threshold by using a different long range portion rather than adjusting the screening radius.

Figure 1 illustrates the procedure by which the potential is chosen. A good starting point for the screening radius is the Firsov value. The parameters of ADDES are then set at conservative values: EM is set marginally above the value at which spontaneous activation of the first neighbors would occur, i.e., the value of the potential at the first neighbor distance; EC and FEM are set so that no atoms are frozen. Runs

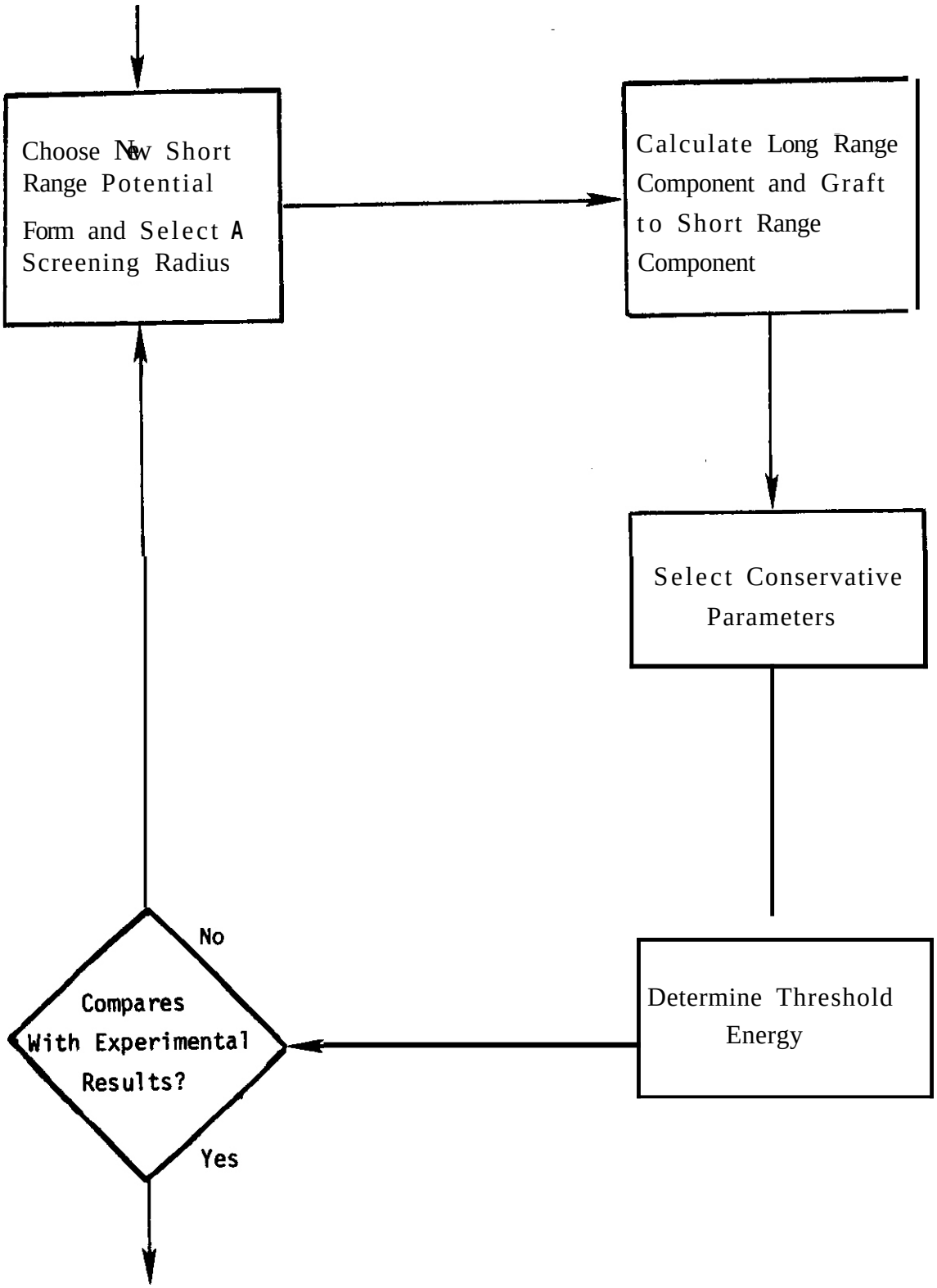

Figure 1. Procedure for Choosinq a Potential.

are made for PKAs along the direction of the minimum threshold (actually they are slightly off the exact direction to spoil the symmetry). The energy is varied until the threshold value is determined. The threshold in ADDES is defined as the energy at which a Frenkel pair is created, which has a separation of at least 1-1/2 lattice constants. This threshold definition compares favorably with the results of the dynamical code COMENT for copper. For some materials the direction of the minimum threshold energy is not well known experimentally. In fcc metals it is usually the <110> direction, but in gold the experiments are inconclusive,[3] and the threshold has been shown by modeling work[3] to be in the <100> direction.

If the threshold value does not compare well with experimental values, then the screening radius is adjusted, and the procedure is repeated.

The procedure for optimizing parameter settings is diagrammed in Figure 2. One starts with the conservative values used in the potential determination. Runs are performed for a PKA slightly off a close-packed direction with an energy perhaps several times the threshold (high enough to produce some damage, but low enough to keep run times small). The value of EM is increased in increments on the order of tenths of eVs, until the resulting cascade is dynamically different from the baseline run, as characterized by replacements, pair production, focusing, etc. The number of replacements seems to be the quantity most sensitive to the value of EM.

Using the highest acceptable value of EM, EC is varied until the dynamical behavior is affected. FEM is maintained at 1 eV greater than EC by an empirically determined rule of thumb. The focusing energy seems to be the parameter most sensitive to the value of EC. The highest acceptable value of EC is retained.

As the PKA energies of events to be simulated increase, even with the optimized parameters, the limitations of computer time and size are soon reached. This limit for ADDES is on the order of 1 keV in copper.

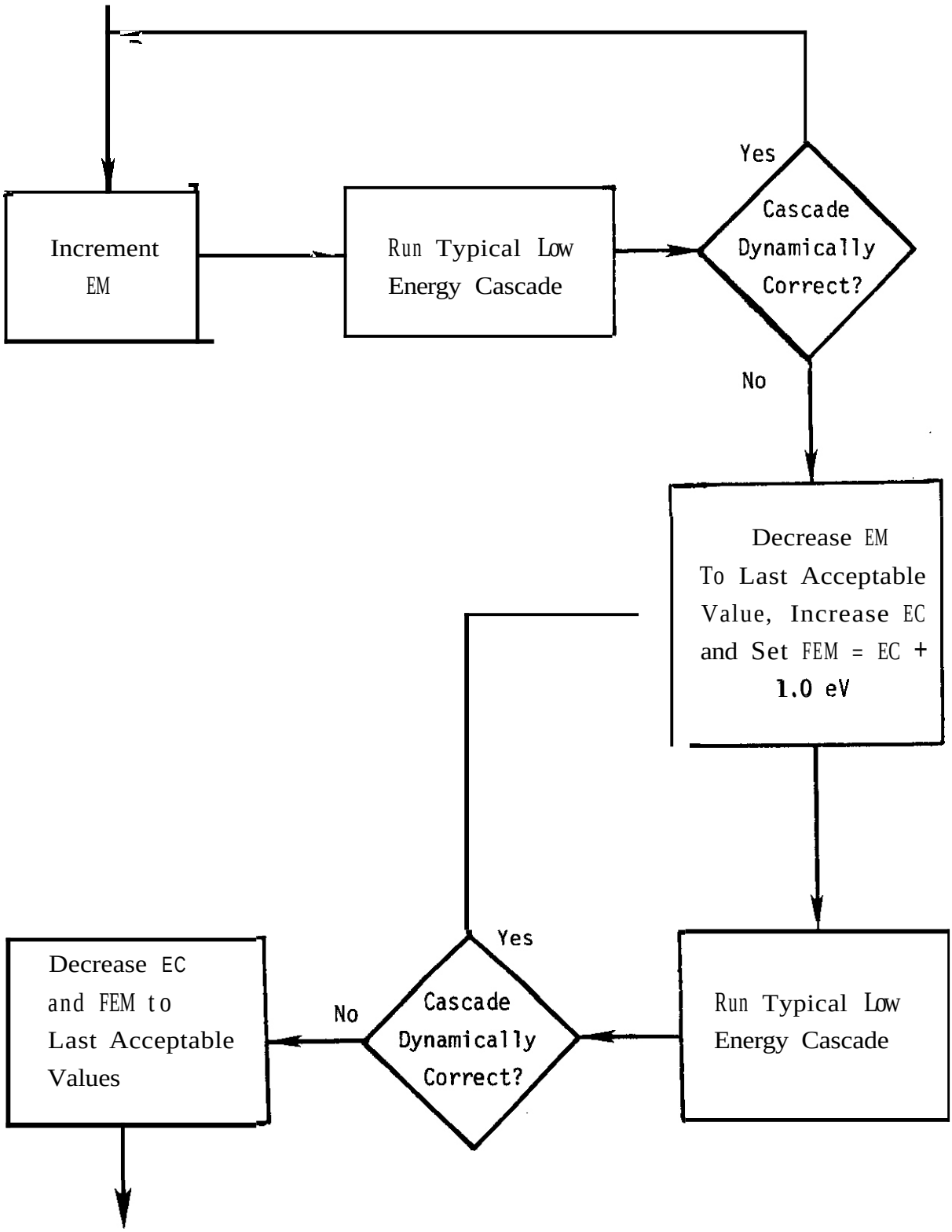

Figure 2. Procedure for Optimizing Parameter Settings.

Depending on the information sought, it may be possible to model higher energy events on a piecemeal basis. For example, in our recent simulation of transmission sputtering by 700 eV Xe^+ ions on gold (to be reported on later), the phenomenon of interest is the transmission of energy by very long focusons. To study this economically, a few long focusons were generated and their energy loss per collision determined. The sputteringq events themselves were run only unti1 wel1-developed focusons appeared; their lengths were extrapolated from the energy loss information.

Initial conditions must be set according to the phenomenon to be simulated. In principle ADDES will model PKAs of any energy in any direction. Computer time and size limits determine whether an event can be run to a point where all atoms have below-threshold energies. There is no mechanism for inelastic energy losses in ADDES at this time since the code was designed for low energy applications. At present only fcc or bcc metals may be modeled.

When choosing PKA directions it is important that high symmetry directions be treated carefully. This is especially important in codes like ADDES which have no provision for thermally induced atom displacements. Because symmetry can often be responsible for extraordinary events, high symmetry directions should be avoided in any statistical analysis with respect to direction. Spoiling symmetry somewhat by aiming PKAs slightly off the high symmetry directions eliminates singular behavior.

It is within the scope of ADDES to allow more than one species of atom to occupy the lattice sites, hence to model radiation effects in alloys and effects caused by impurities. There is also the capability to introduce pre-existing lattice defects or a complete surface on which ions of any species can impinge at any angle or energy. This permits the modeling of back-sputtering, transmission sputtering or ion ranges. The reliability of simulations of such events depends, of course, on the validity of the necessary interaction potentials, knowledge of the surface characteristics, etc. It also depends on the degree to which these quantities affect

the measurable quantities being simulated.

ADDES has been used with success to investigate many aspects of damage production due to low energy PKAs in copper.[1,2] A study of replacement sequences in nickel-aluminum alloys has also been done.[4] The results of the recent simulation of transmission sputtering in gold also show effects of back-sputtering as well as channeling.

Within the uncertainty of interatomic potentials, the systematic approach outlined here can result in simulations of experimentally observable events which are soundly based physically as well as being computationally tractable.

VI. REFERENCES

1. D. M. Schwartz, J. 0. Schiffgens, D. G. Doran, G. R. Odette, and R. G. Arivasu. "A Comoarison of Manv-Bodied and Binary Collision Cascade-Models up to 1 keV," Computer Simulation for Materials Applications, NBS, 1, 75 (1976).
2. J. 0. Schiffgens, D. M. Schwartz, R. G. Ariyasu and S. E. Cascadden, "Computer Simulation of Replacement Sequences in Copper," Damage Analysis and Fundamental Studies Quarterly Technical Progress Report, January - March 1978, DOE/ET-0065/1, p. 88.
3. W. Bauer, A. I. Anderman, and A. Sosin, "Atomic Displacement Process in Gold," Physical Review, 185, 870 (1969).
4. J. H. Gerson, Computer Simulation of Radiation Damage in a Nickel-Aluminum Alloy, M. S. Thesis, California State University at Northridge (1976).

VII. FUTURE WORK

A computer simulation of transmission sputtering in gold is being completed. Other work with ADDES in the near future is aimed at simulating high energy cascades (up to 100 keV). Documentation of the code is in progress;

VIII. PUBLICATIONS

None.

I. PROGRAM

Title: Irradiation Effects Analysis (WH011)
Principal Investigator: D. G. Doran
Affiliation: Hanford Engineering Development Laboratory

II. OBJECTIVE

The objective of this work is to develop computer models for the simulation of high energy cascades which will be used to generate defect production functions for correlation analyses of radiation effects.

III. RELEVANT DAFS PROGRAM TASK/SUBTASK

SUBTASK II.B.2.3 Cascade Production Methodology

IV. SUMMARY

The quasi-dynamical computer code AOOES is used for the simulation of high energy cascades in copper in a two-stage process. In the first stage, cascades of up to 100 keV are allowed to develop until no atom is above about 500 eV in energy. In the second stage the damage produced by the residual energetic atoms is evaluated from previous low energy simulations. The binary collision code MARLOWE will be calibrated against the ADDES results and used for generating statistically significant numbers of cascades. First stage runs of ADDES were performed for 10 keV and 80 keV PKAs in copper. Methods for analyzing and comparing high energy cascades are being developed.

V. ACCOMPLISHMENTS AND STATUS

A. The Application of Dynamical Computer Models to the Simulation of High Energy Cascades - H. L. Heinisch (HEDL), D. M. Schwartz (California State University at Northridge), and J. O. Schiffgens (HEDL).

1. Introduction

Computer simulations are essential elements in the study of radiation damage in fusion reactor materials. Computer models can provide damage parameters for correlating and extrapolating experimental data, and phenomenology for guiding and analyzing experiments. Techniques for computer simulation of radiation damage have been under development for the past twenty years, primarily for the purpose of addressing the radiation damage problems of materials in various types of fission reactors. A major difference between fission and fusion reactor material environments is the considerable component of high energy neutrons at the fusion reactor first wall. Thus, it is important to be able to model the damage produced by the high energy primary knock-on atoms (PKAs) generated in the material by these neutrons.

Within the limitations of our knowledge of interatomic potentials, dynamical computer models provide the most realistic simulations of radiation damage phenomena. However, because of the limitations of computational time and computer size, they have been limited to simulating low energy events. The dynamical code COMENT[1] has been used to simulate damage due to PKAs of not more than about 500 eV.

Application of the binary collision approximation, valid at the higher energies, has resulted in a computer code MARLOWE[2] which can treat high energy PKAs. However, since MARLOWE employs the binary collision approximation, it is not clear that it can accurately model the lower energy aspects of the cascade in which many-body interactions are important. Because it is fast, statistically meaningful numbers of runs can be made.

Lying between these two codes in concept is the computer code ADDES,[3] often labeled a "quasi-dynamical" code. It treats many-body interactions, but, by proper parameter selection, it can be made to ignore all but the most important interactions in the crystal. AODES has been carefully calibrated with COMENT for low energy PKAs in copper,[3] but until now it has not been applied to high energy events.

It is possible to do realistic modeling of high energy events with these existing computer codes if care is taken to build properly from the most realistic basis: dynamical codes applied at low energies. The dynamical code COMENT is based on our best knowledge of atomic interactions within the context of molecular dynamics modeling. The quasi-dynamical code ADDES has been calibrated against COMENT and is capable of going to much higher energies where the binary collision approximation is valid. The basic strategy of the present work is to carefully push ADDES to higher energies (up to 100 keV) and to compare it to the results of MARLOWE at these energies. If necessary, adjustments can be made to MARLOWE so that it is consistent with ADDES. ADDES and MARLOWE will be compared at lower and lower energies until they diverge. Thus, MARLOWE will be calibrated against a dynamical code and its lower limit of validity will be established. MARLOWE, with appropriate adjustments or additions to account for the low energy aspects of the cascade, can then be used to study the effects of high energy cascades. Since it is very fast, it will be possible to generate cascades in large numbers for statistical analyses or as starting points for annealing simulations.

2. The Model

The higher energies are being approached in a two-stage modeling process. Using ADDES, the cascade is allowed to develop until no atom has more than a relatively high cut-off energy (approximately 500 eV). As energetic atoms fall below the cut-off energy, they are tagged and removed from consideration during the remainder of the development of this first stage. In this way the gross features of the cascade are obtained without having to monitor the activities of every atom involved in each time step (a computationally intractable feat even for ADDES). The second stage of the model is the evaluation of the damage produced by the energetic atoms tagged in the first stage. Comparison of ADDES and MARLOWE begins with the first stage.

ADDES has been calibrated at low energies in copper with a modified Moliere-Englert potential.[4] The first stage of the high energy cascade modeling is being done using cnly the repulsive Moliere potential with the same screening radius (.00738 nm) as in the low energy simulations. Inelastic energy losses in MARLOWE are turned off so that they will not have to be included in ADDES. Effects of inelastic losses will be examined using MARLOWE.

We have demonstrated that this approach to modeling high energy cascades is feasible by modeling cascades of up to 80 keV with both MARLOWE and ADDES. To get to the higher energies in reasonable times without affecting the dynamics, some changes had to be made in ADDES. In particular, throughout the event the time step size is scaled by a fractional power of the instantaneous kinetic energy of the most energetic atom. Care was taken to allow energetic atoms to be "frozen" in such a way as to not affect the dynamics of major collisions. If an atom has less than 500 eV, it is frozen, i.e., its position and velocity are noted, and its equations of motion are no longer integrated. This may only happen if the atom has been active for a minimum number of iterations, has reached a maximum in its kinetic energy, and has less than a prescribed cut-off value of potential energy.

3., Results

First stage runs of ADDES have been done for PKAs of 10 keV and 80 keV in several directions in copper. Because minute differences in initial conditions (energy, direction, freezing parameters, time step, etc.) at these energies can make major differences on the atomic level in the resulting cascades, it is impossible to compare cascades individually even for parameter optimization. At very small energies the symmetry of the crystal lattice will force slightly different PKAs to produce very similar results, but the lattice has little effect on high energy collisions. The comparison of high energy cascades can only be done on some statistical basis. This can be accomplished by comparing cascades with respect to only

some gross feature of the cascades, such as the total number of defects produced. Or, one can choose a set of initial conditions which are different, but are considered equivalent, such as randomly oriented (or nearly equal) PKA directions, over which to average the more specific features of the cascades.

Early indications are that high energy PKAs are nearly isotropic with respect to defect production. Other indications are that the 80 keV cascades can be interpreted in terms of a series of sub-cascades.

VI. REFERENCES

1. J. O. Schiffgens and R. D. Bourquin, J. Nucl. Mat., 69, 790 (1978)
2. M. T. Robinson and I. M. Torrens, Phys. Rev., 9, 5008 (1974).
3. D. M. Schwartz, J. O. Schiffgens, D. G. Doran, G. R. Odette and R. G. Ariyasu, Computer Simulation for Materials Applications, NBS, 1, 75 (1976).
4. J. O. Schiffgens, D. M. Schwartz, R. G. Ariyasu and S. E. Cascadden, Damage Analysis and Fundamental Studies Quarterly Technical Progress Report, January - March 1978, DOE/ET-0065/1, p. 88.

VII. FUTURE WORK

The first stage comparisons of ADDES and MARLOWE will be completed, with some emphasis on the spatial distribution of the damage. The synthesis of the first and second stage aspects of the damage will be developed, and a systematic study of defect production by high energy PKAs will be done.

VIII. PUBLICATIONS

This work will be reported at the First Topical Meeting on Fusion Reactor Materials, January 29-31, 1979, Miami Beach, Florida.

CHAPTER 5

SUBTASK C: DAMAGE MICROSTRUCTURE EVOLUTION AND MECHANICAL BEHAVIOR

I. PROGRAM

Title: Fundamental Studies of Radiation Damage Analysis

Principal Investigator: G.R. Odette

Affiliation: University of California, Santa Barbara

II. OBJECTIVE

The object of this work is to develop physical models describing the influence of metallurgical and irradiation variables on the evolution of damage microstructure and the alteration of mechanical properties. These models will be used to correlate available data, to plan and analyze new experiments and, ultimately, to extrapolate to fusion reactor conditions.

III. RELEVANT DAFS PROGRAM PLAN TASK/SUBTASK

SUBTASK II.C.1.2 Effect of Material Parameters on Microstructure-Modeling and Analysis

SUBTASK II.C.2.4 Effect of Helium on Microstructure-Modeling and Analysis

SUBTASK II.C.5.3 Effects of Cycling on Microstructure-Modeling and Analysis

SUBTASK II.C.6.2 Effects of Damage Rate and Cascade Structure on Microstructure-Modeling and Analysis

SUBTASK II.C.14.1 Modeling of Flow and Fracture Under Irradiation-Modeled Development

SUBTASK II.C.16.1 Composite Correlation Models and Experiments-Correlation Model Development

SUBTASK II.C.18.3 Relating Low - and High Exposure Microstructures-Modeling and Analysis

IV. SUMMARY

A. Microstructural Evolution

Several rate theory models have been developed to study the influence of irradiation and material parameters on the evolution of damage microstructure. Nucleation models have been used to begin to scope the combined effects of helium and displacements and, alternately, irradiation pulsing on void formation. Void growth models have been used to map out broad regions of mechanism - parameter space which are consistent with experimental observations of swelling in neutron-irradiated, 300 series austenitic stainless steels. In addition, these models have provided important clues about the fundamental source of the large variability observed in the swelling data and the sensitivity of swelling to micro-chemical variations. A model of dislocation microstructural evolution has been developed and combined with the void growth model illustrating the very strong correlation between the development of various microstructural features. Finally, a more comprehensive and detailed composite nucleation and growth model is under continued development.

B. Mechanical Properties

Some preliminary results of applying micromechanical models relating microstructure to flow and failure are available for irradiated 300 series austenitic stainless steels. It has been found that fluence and temperature dependent changes in the yield stress can be correlated to the development of cavity, loop and dislocation microstructures using simple dislocation hardening models.

IV. ACCOMPLISHMENTS AND STATUS

A. Microstructural Evolution Under Irradiation -- G.R. Odette, D. Frey, P. Lombrozo, L. Parme, S. Schwartz and R. Stoller (University of California, Santa Barbara)

1. Introduction

The evolution of microstructural features characteristic of irradiated materials - network and loop dislocations, voids, bubbles, precipitate structure, and regions of alloy constituent or impurity segregation or depletion - is certainly an exceedingly complex phenomena involving numerous interacting solid state mechanisms, many of which are not well defined or understood. Further, damage response is known to be sensitive to the particular set of damage variables describing the irradiation environment - temperature, stress, flux spectra, the chemical media, the time history of these variables and the initial microstructure and microchemistry-composition, dislocation structure, solute distribution and precipitate morphology. Clearly, pure empiricism cannot lead to understanding of microstructural evolution sufficient for the needs of the fusion materials program.

The proper goal of the modeling is then to identify those combinations of mechanisms and parameters which are consistent with experiment. In practice this means extensive mapping of mechanism-parameter space (MPS) and comparing the predicted microstructural responses with the broad range of empirical observations. Since the numerous combinations of mechanisms and parameters may fit particular sets of data, and since the data is itself highly scattered, an efficient strategy must be developed to limit the regions of MPS which are thought to be physically significant.

Therefore, it is necessary to use models which vary in detail and complexity and which are tailored to a particular application. Simpler models are used to broadly scope regions of MPS. The understanding gained from the simpler models is used to refine mechanisms and define parameters for the more comprehensive composite models. Ultimately, the composite models will be used for correlation of available data and extrapolation to fusion reactor conditions.

Models developed in this work include:

a. the effect of irradiation pulsing on nucleation of extended defects;

b. bubble nucleation and growth, and formation of voids on bubbles which have exceeded the critical size for continuous vacancy driven growth;

c. void growth models with direct or parametric treatment of numerous mechanisms which have been postulated to influence swelling;

d. dislocation structure evolution;

e. composite models of the nucleation and growth of various microstructural features.

The following sections will summarize briefly the status of the modeling efforts with illustrative examples. No attempt is made, however, to provide significant details; a more complete progress report on these topics is under preparation and will be issued separately in the near future.

2. Microstructural Evolution Models

a. Effect of Pulsing of Irradiation Parameters on Void and Loop Nucleation

Limited experimental [1] and theoretical [2] evidence indicates that pulsing of irradiation parameters (flux, temperature and stress) can have a strong influence on the evolution of damage microstructure. Numerous direct and indirect mechanisms may be postulated to explain such an effect; however, preliminary analysis suggests that nucleation of extended defects, particularly voids for which there are significant kinetic barriers (i.e. large critical sizes and low nucleation rates), would be particularly sensitive to irradiation pulsing.

Results of an initial study of the effects of irradiation pulsing on void nucleation have been reported previously [2]. In that work, the set of differential - difference equations describing classical void or loop nucleation (i.e. the Master Equation for this process) was numerically integrated to derive the mean nucleation rate during an irradiation pulse period as a function of temperature, supersaturation, effective bias, irradiation pulse on/off-times and material and defect parameters (e.g. point defect migration and formation energies, surface energy and the like).

The major drawback to this approach was the mathematical and computational complexity; in particular, large critical void nucleus sizes, characteristic of neutron irradiation conditions, require very large sets of differential-difference equations. Attempts to provide more physics in the models or to carry out necessary model sensitivity studies would result in prohibitive computational costs.

Therefore an alternative approach has been pursued based on correlating the results of the numerical calculations using easily

calculated dimensionless pulsing parameters. These parameters are defined as follows: a pulse buildup parameter $P_b = t_b/\tau_b$ where t_b is the pulse on-time and τ_b the time constant for reaching the steady state nucleation rate or steady state concentration of embryos; a decay parameter $P_d = \tau_d/t_d$ where t_d is the interval between pulses and τ_d a relaxation time characteristic of decay of the embryo distribution. Fig. (1) shows the result of such a correlation, expressed in terms of a comparison of correlation predictions versus numerically integrated values of the ratio ($R \leq 1$) of the average nucleation rate during an irradiation pulse divided by the steady state nucleation rate for uninterrupted irradiations. While the agreement is clearly not perfect both the correct trends and correct order-of-magnitude numerical estimation of R are predicted over large variations in the dimensionless pulse parameters and their combinations. This level of precision is probably far better than the inherent uncertainties due to limitations in the physical models.

Now instead of solving the system of equations with each new set of parameters or added level of physical complexity, which may be computationally prohibitive, it is only necessary to recalculate the parameters to crudely approximate the behavior of a pulsed system. Additional physical factors such as temperature and stress cycling, heterogeneous nucleation on helium bubbles and the like can be included easily in calculating the parameters. Further, the simple analytical expression derived for R can be incorporated routinely in composite nucleation and growth models.

Before leaving the subject it is important to note that several other mechanisms and phenomena not specifically discussed might be affected by pulsing. These are under study and will be discussed in future reports. Finally, the general applicability of rate theory to either periodically pulsed or steady-state environments which introduce damage randomly and inhomogeneously in space and time has been questioned [3]. However, reexamination of the statistical mechanical basis

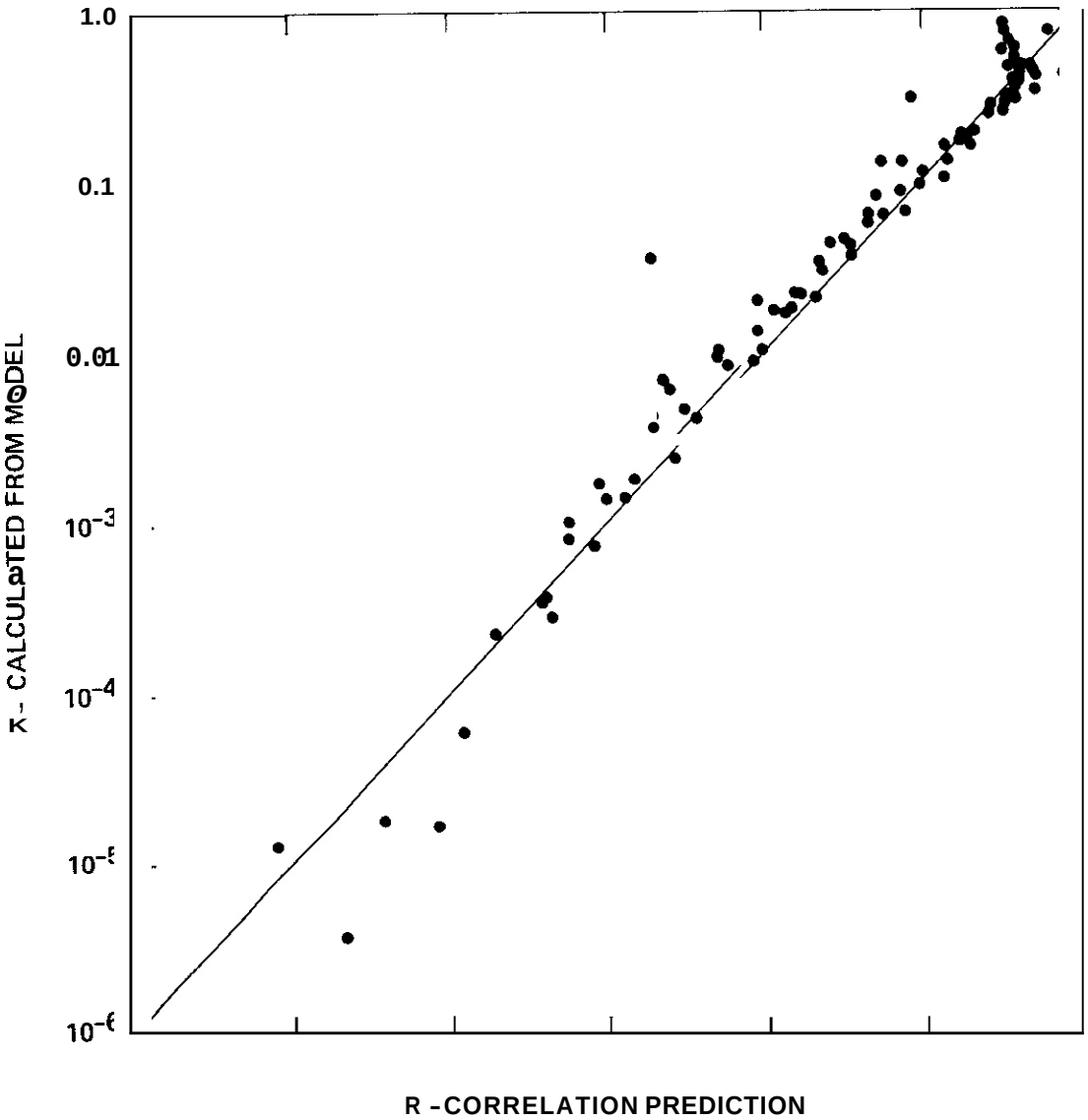

FIGURE 1. Comparison of Predicted Reductions in Void Nucleation Rates Using Correlation and Numerical Calculations.

of rate theory describing population behavior with implicit averaging processes indicates that rate theory can be used in' these circumstances. However, the specific forms based on linear averaging of individual coefficients characteristic *of* current rate theory models may not always be appropriate to treating non-linear and coupled phenomena; further, the assumption of local equilibrium may not be valid in all circumstances. The possible importance of these effects is, however, amenable to systematic study.

b. Bubble Nucleation-Void Formation Model

There is strong evidence of an association between helium and helium bubbles and microstructural evolution, particularly void formation. Numerous helium-displacement interaction mechanisms, ranging from stabilization of three dimensional vacancy clusters to altered defect diffusivities, have been proposed [4,5]. The relative importance and combined effect of these mechanisms is not understood. However, a basic feature of the problem seems clear. The scale (i.e. the spatial distribution and density of extended defects) of microstructural development, and other implications which derive from such scale, are in large part governed by the scale upon which helium bubbles precipitate and grow since they are a precursor to other microstructural features. This, in turn, implies a strong dependence on the mobility of helium and mechanisms which influence the formation and growth of stable helium bubbles.

The bubble nucleation-void formation model was derived as follows. The rate equations for bubble nucleation and growth to a size beyond which void growth occurs are solved. Mechanisms directly considered include: helium diffusion, including irradiation enhanced mobility; collisional coalescence of bubbles; helium resolutioning from bubbles; and net vacancy fluxes as a function of damage rate and micro-

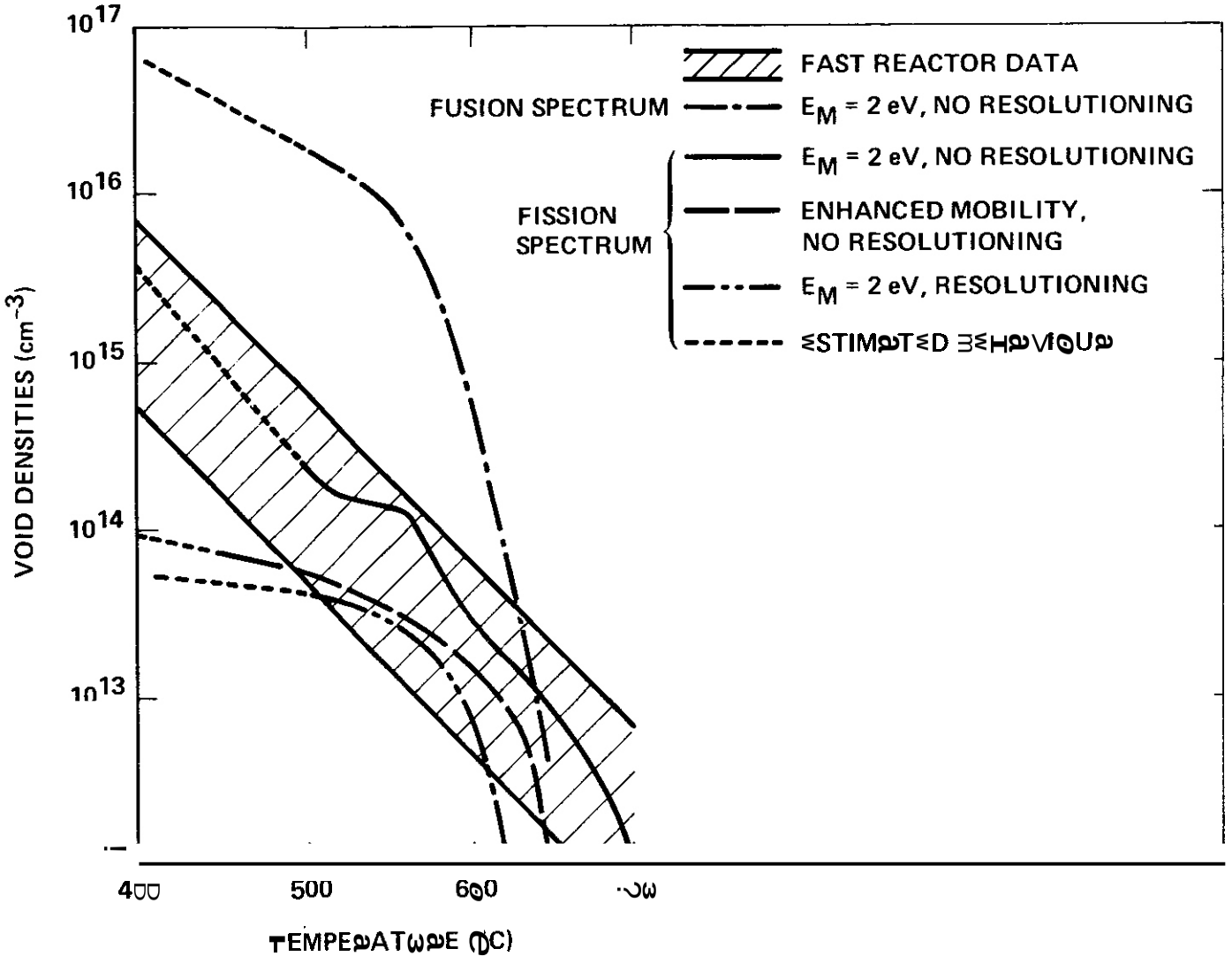

FIGURE 2 Predicted Void Densities from Bubble Nucleation and Growth - Void Formation Model

structure. Dislocation evolution and void growth are treated parametrically. Statistical void nucleation is not modeled. Some typical model calculations are shown in Fig. (2) for the temperature dependence of void densities at a dose of 30 dpa and at various helium concentrations. Ancillary values such as defect mobilities, surface energies, and bias factors were chosen to be consistent with observed post-incubation swelling rates in fast reactors. The fast reactor data trend band is shown as a cross hatched area along with the results of various models. The best results are apparently for a model with approximately nominal helium mobility and no resolutioning. The radiation enhanced mobility results deviate from the data at low temperature (<500°C) predicting lower void densities and a somewhat lower temperature dependence than are generally observed. The resolutioning case indicated a lower concentration of voids at high temperatures than is generally observed. The low temperature behavior of the nominal mobility and resolutioning cases are not determinate, since statistical nucleation is not included in the model but would probably occur readily on available precritical bubbles (crudely estimated behavior in this temperature regime based on existence of such bubble populations is shown as dashed lines; however, this must be viewed as highly approximate).

While these results are not conclusive, since the model is approximate and MPS has not yet been extensively mapped, the nominal mobility, no-resolutioning case, which provided a reasonable fit to the data, was used to estimate the behavior in a fusion reactor environment. The results show that for a factor of 100 increase in helium generation rate void densities increase by factors of approximately 50 to 10 in the temperature range of 500 to 600°C, decreasing to $\lesssim 1$ above 600°C. These results are somewhat different than would be estimated on the basis of simple bimolecular approximations; the reasons for this behavior are under investigation.

c. Void Growth Model

The most extensive mapping of MPS has been carried out using a modified void growth model. The basic rate theory model has been reported previously and is patterned after that derived by Brailsford and Bullough,[6] now ubiquitous to the theoretical swelling literature. Significant modifications have been made to the basic model, however, to allow approximate treatment of a number of mechanisms which have been postulated to influence swelling. These mechanisms include: solute trapping, enhanced diffusion, segregation and precipitation; sink-sink interactions, variable efficience and rate controlling processes; initial microstructures and gas bubbles; cascade vacancy loops; dislocation microstructures; ~~and~~ intercorrelations among the evolution of various microstructural features. Modeling of these mechanisms is simply parametric in some cases, based on analytical expressions in others, and makes use of detailed submodels in still others.

Fig. (3) shows, as an example, temperature dependent incubation doses and the post-incubation dose swelling rates; Fig. (3a) shows calculations where parameters have been selected to fit data for 304 stainless steel; and Fig. (3b), with the model fit to pure stainless steel[7]

Model prediction-experiment comparisons are not, however, generally as simple as these examples would indicate. First, other sets of mechanisms and parameters could be selected to provide an equivalent fit; hence, a thorough mapping of MPS is required before firm conclusions can be drawn. Second, the experimental data is most often highly scattered and not amenable to simple interpretation. This behavior is illustrated in Fig. (4) where post-incubation swelling rates for 316 stainless steel are shown[7-9]. In such cases MPS maps, which are really systematic representations of model sensitivity, can provide important clues as to the fundamental source of such variability.

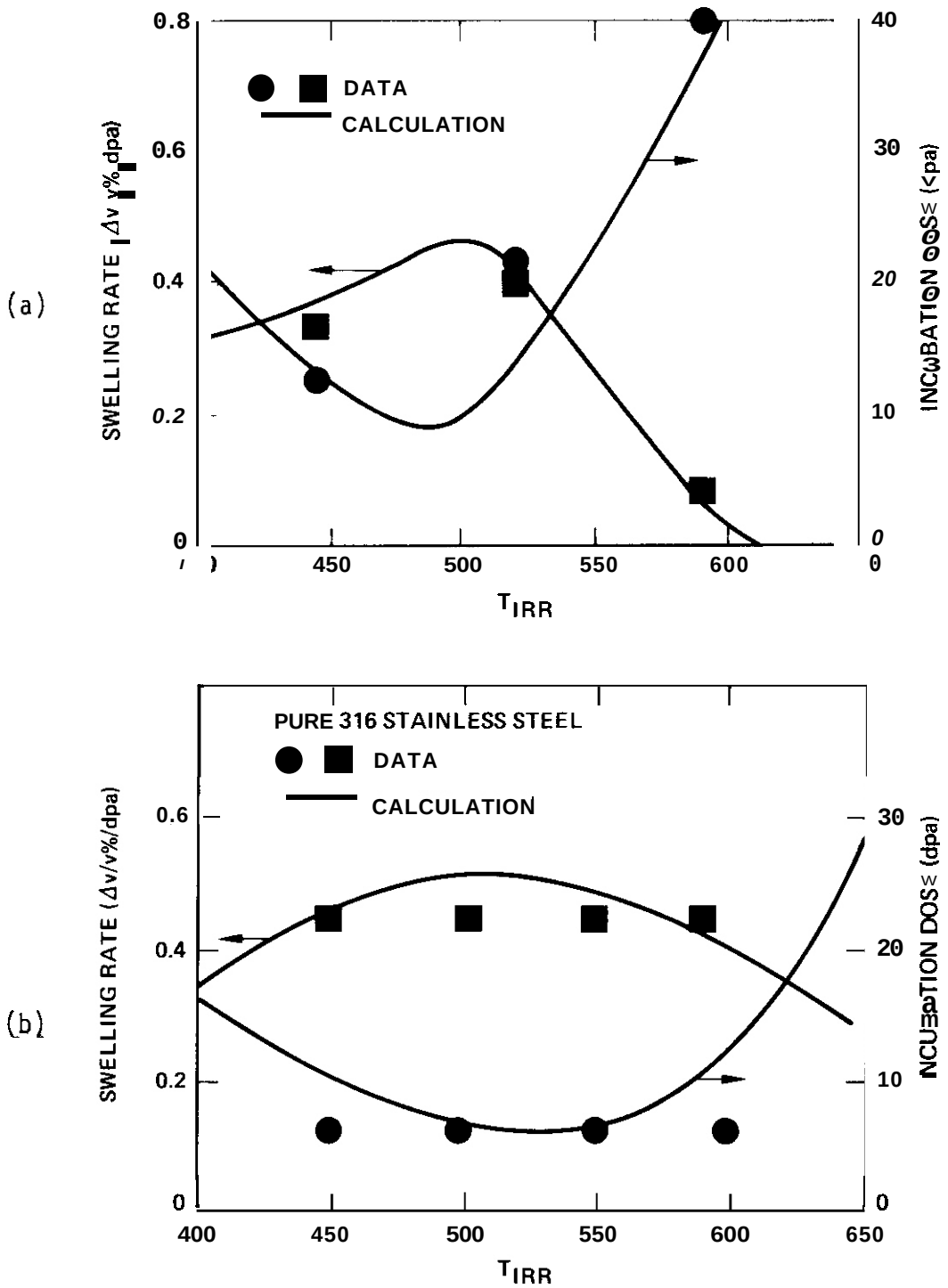

FIGURE 3. Model Prediction - Experiment Comparisons of Swelling Parameters for (a) 304 and (b) Pure 316 Stainless Steels.

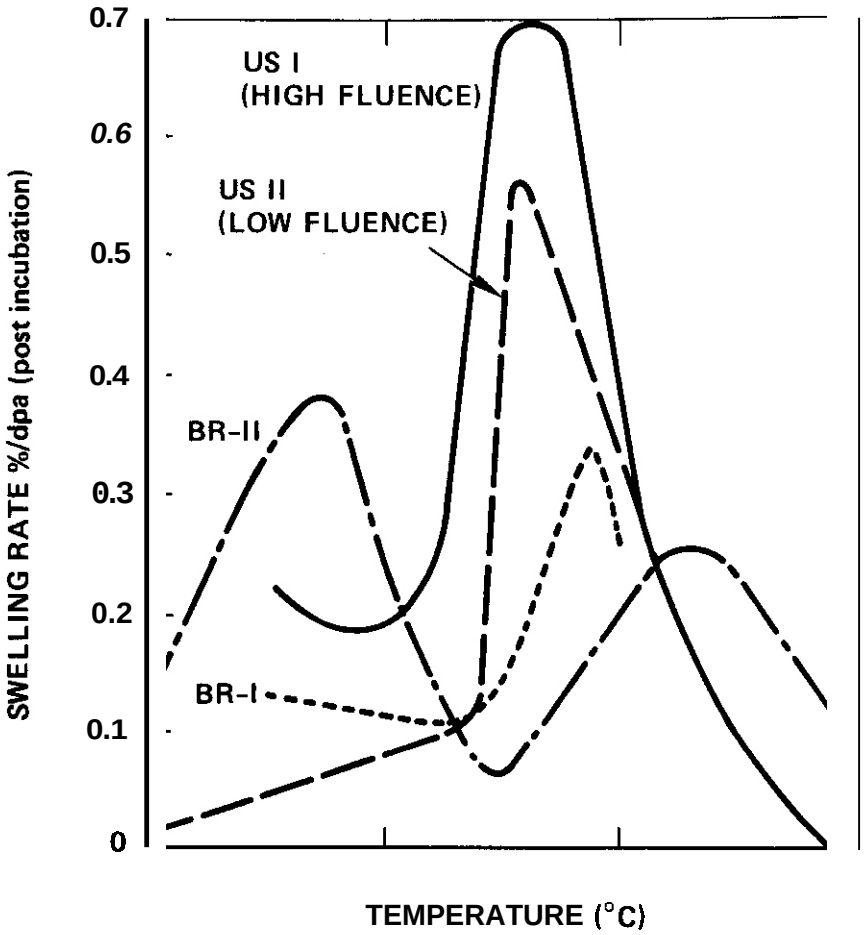

FIGURE 4. Swelling Rate Curves for 316 Stainless Steel from Various References.

Examples of MPS maps, indicating the variation of peak swelling temperature and peak swelling rate with vacancy formation and migration energies, are shown in Fig. (5).

Several thousand calculations have been carried out to date in initial mapping of MPS. The typical cost of generating a swelling curve is on the order of $.15 to $1.50 depending on the set of mechanisms and parameters; hence, extensive mapping is feasible. It is estimated that several times this number may be needed to fully map MPS for the current range of mechanisms and parameters in the void swelling model. Until now analysis of the results has been done by hand; clearly however, mapping, development of approximate analytical expressions and lumped parameters, comparisons of predictions with experiment, and identification of physical regions of MPS must be automated. Such automation procedures are now under development.

Preliminary results from the modeling have suggested a number of qualitative features of microstructural evolution, including:

(1) probable sequences of events leading to formation of extended defects - viz. bubble nucleation and growth as a precursor to void formation, possibly aided by solute segregation-matrix depletion and phase instability mechanisms;

(2) a strong correlation between the evolution of various microstructural features;

(3) a strong correlation between microstructure and microchemistry linked primarily through effective defect mobilities which may be time and dose dependent due to phase instabilities;

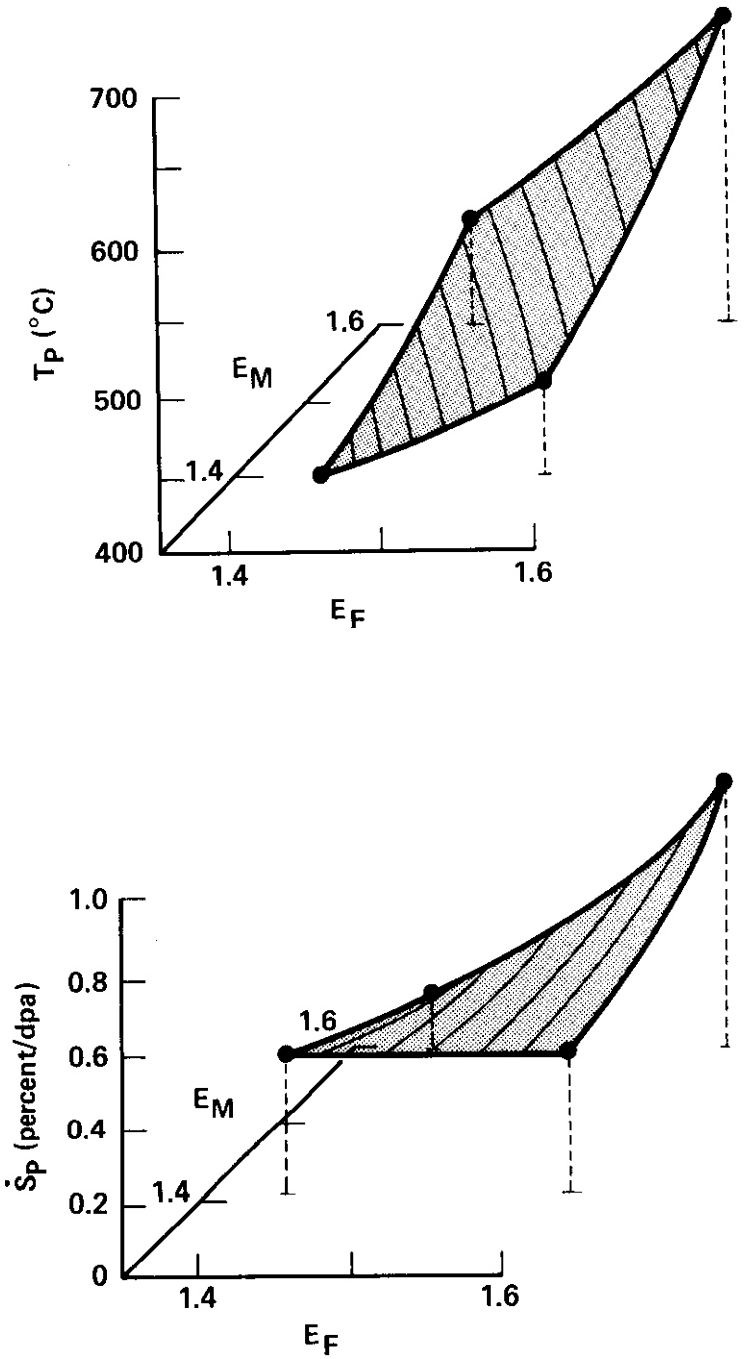

FIGURE 5. Illustrations of MPS Maps, in This Case Swelling Parameters as a Function of Vacancy Formation ani Migration Energies.

(4) influence of the initial nucleation microstructure on subsequent growth stages - viz. void-to-dislocation sink ratios directly influence swelling, and small bubbles sinks may coexist with voids in some cases;

(5) sensitivity of swelling to bubble nucleation and growth kinetics and helium transport mechanisms;

(6) increasing helium generation rate leading to either increased or decreased swelling depending on the particular set of damage parameters - viz. dpa rate, He/dpa ratio, temperature, and material parameters.

d. Dislocation Microstructure Evolution Model

Strong correlations between evolution of various microstructural features are well established; indeed, the point defect segregation mechanisms that lead to the formation of one microstructural feature must, by basic principles of symmetry and conservation, affect other features. This kind of correlation is clearly illustrated in considering the growth of voids through the net accumulation of vacancies and the evolution of dislocations through the net accumulation of interstitials.

Therefore, a model of coupled void growth - dislocation evolution has been developed. The physical basis for the model is as follows:

(1) point defects and di-interstitials can be treated as if at quasi-steady state;'

(2) the di-interstitial is the stable nucleus for faulted loop growth;

(3) bubbles and voids are unbiased sinks for both vacancies and interstitials;

(4) faulted loops and network dislocations both preferentially absorb interstitials;

(5) faulted loops have a greater bias for interstitial absorption than does the network;

(6) loops unfault when they impinge on other dislocations; that is, there is a maximum loop size determined by the total dislocation density;

(7) network dislocations climb at a rate determined by the net accumulation of interstitials (or alternately vacancies);

(8) dislocations climb until they meet a sink, which may be a surface or a dislocation of opposite sign. At high dislocation densities the latter distance is much shorter; hence, the average climb to annihilation distances is a function of the network dislocation density.

Standard rate theory equations have been used to develop a quantitative computer model based on these physical principles. However, a detailed model is not necessary to understand the basic

phenomenology of dislocation evolution. In particular, under void swelling conditions an excess flux of interstitials to dislocations will cause growth of loops to the critical size and climb of network dislocations to annihilation. The various dislocation sink and source terms will eventually quasi-equilibrate in coincidence with an approximate equilibration of the dislocation microstructure and steady state swelling.

Fig. (6) shows approximate steady state loop and total dislocation densities calculated from the model as a function of temperature; Fig. (7) shows a plot of dose-dependent, total dislocation density and void swelling at 500°C for parameters typical of both solution annealed and cold worked stainless steel.

No particular effort has been made to adjust the model parameters or mechanisms. The agreement between these predictions and experimental observations, therefore, is particularly striking. First, the predicted development of saturation dislocation microstructures and swelling rates, irrespective of initial dislocation densities, is in general agreement with experiment [10]. Second, the steady-state values of total dislocation density are in good quantitative agreement with experimental values. The peak in the solution annealed dislocation density curve is a real prediction of the model, but has not been reported experimentally. Third, the steady state values of swelling are reasonable and the magnitudes and relative values of the incubation doses in solution annealed and cold worked material are roughly consistent with experimental trends. Finally, while the faulted loop densities are generally somewhat lower than have been reported in some cases, the values are fairly close to other observations [11]. It should be noted that the predicted loop densities may be particularly sensitive to model parameters. Further, the predicted loop densities first increase, peak and then decrease with dose in agreement with observations; however, this behavior makes experimental-model prediction comparisons more complicated since rather

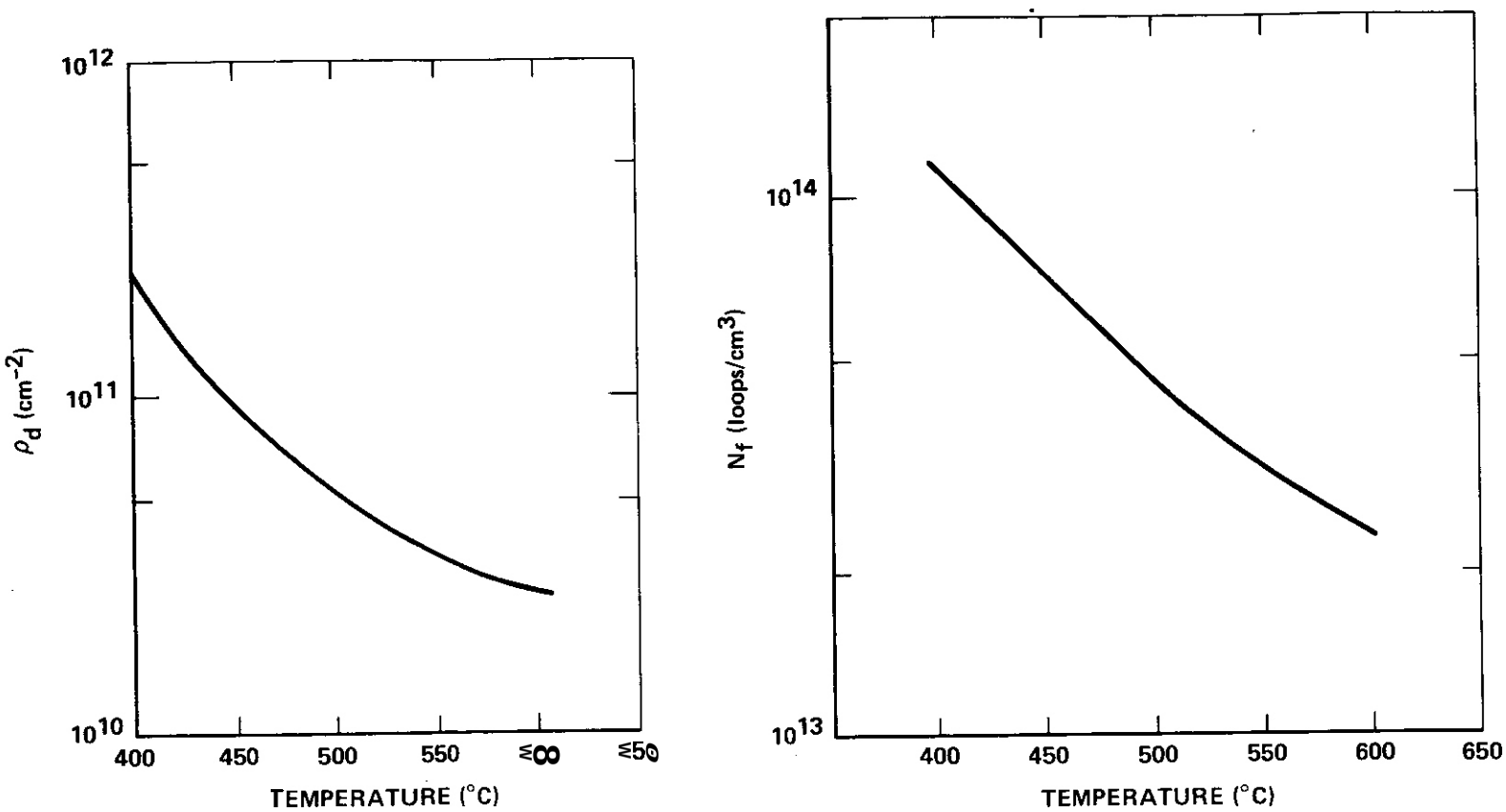

FIGURE 8 Predicted (a) Total Dislocation and (b) Faulted Dislocation Loop Densities.

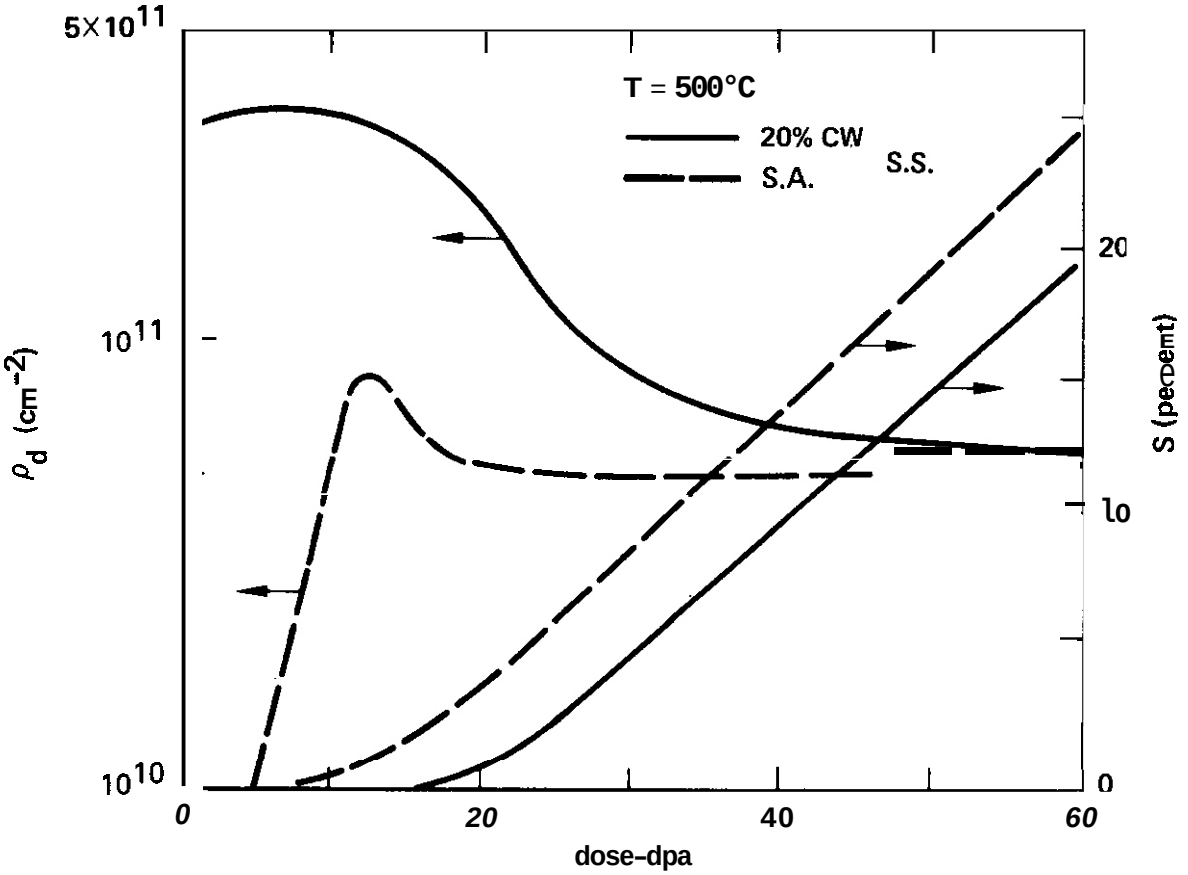

FIGURE 7. Predicted Total Dislocation Density and Swelling *for* Solution Annealed and Cold Worked Stainless Steels.

ecise "equivalent" exposure levels must be determined prior to saturation high fluences.

e. Composite Model of Evolution of Damage Microstructure

A composite model of the evolution of void, bubbles dislocations microstructure and microchemistry in materials in which both helium and displacement defects are continuously generated is under development. The model attempts to provide a comprehensive physically based framework for most of the mechanisms described previously so their relative significance can be assessed. Such a model will also allow more precise determination of the effects of interaction between the various fundamental damage mechanisms.

The model treats directly the three interacting phenomenological steps in microstructural evolution -- diffusion of primary defects (vacancies, interstitials, helium and solute atoms), nucleation of extended microstructural features, such as voids, and growth of these extended defects. The input data are temperature, primary defect generation rates, and material and defect parameters. A preliminary version has been reported [4].

In the following section we will describe the general framework of the composite model; because of its mathematical and computational complexity, however, not all the components have been fully implemented.

The diffusion model calculates the quasi-steady-state concentrations and sink fluxes of vacancies, interstitials and solute atoms as a function of the generation rate and existing sink concentrations. Of course, these concentrations vary with time as the microstructure evolves with continuing irradiation. The differential equation describing the lattice helium concentration is numerically

integrated from the start of irradiation. Provision for trapping and detrapping of helium, and a mixture of interstitial and substitutional diffusion is provided. Dislocation evolution is modeled as described previously.

Bubble nucleation and growth is treated by a set of differential equations describing the time dependent evolution due to helium atom migration to form di, tri, tetra and larger helium atom clusters. Helium impingement rate coefficients are based on diffusion limited kinetics. Emission of helium atoms from clusters can occur either thermally, and/or by cascade resolutioning, and/or self-interstitial impingement. Bubble motion leading to collisional coalescence is also allowed; point defect fluxes are used to modify bubble bulk diffusivities. Terms for trapping helium and heterogeneous nucleation of bubbles on dislocations and precipitates are included in the model. A major difference between the simpler void formation model, described previously, and the composite model is that statistical void nucleation is treated in the latter. The kinetic equilibrium radii for the bubbles are calculated as a function of the number of helium atoms and the existing net vacancy flux using an equation-of-state derived from the hard-sphere model.

By careful group averaging, 100 differential equations may be sufficient to treat helium clusters of up to several thousand atoms. Beyond the maximum cluster size the growth rate of helium clusters to a critical void nucleus is determined. The bubbles serve as heterogeneous nucleation sites for void embryos, which in turn can form voids. Inclusion of the embryo term is to allow for an incubation time for the nucleation of voids on bubbles. Thus, a bubble of size x can form by a bubble of size x-1 by acquiring a helium atom, by a bubble of size x+1 emitting a vacancy, or by dissolution of an embryo of size x. A bubble in size class x is lost by helium impingement, emission or formation of an embryo of size class x.

Void nucleation is allowed to take place homogeneously, and heterogeneously on embryos or on other specified heterogeneous nucleation sites. Embryo formation rates are determined from the number of helium atoms and prevailing net vacancy fluxes. Actual rates are interpolated from input tables of values calculated using simple nucleation theory. Incubation times are treated similarly. The coupled set of embryo-bubble differential equations is structured so that at times on the order of the incubation time the concentration of embryos in a given size class would approach the steady state critical nucleus concentration if the bubble density were to remain constant. Void nucleation occurs at the rate of net vacancy impingement on an embryos. Nucleated voids are placed in the closest member of a matrix of size classes in helium number-radius space. An additional source of voids is provided for by the growth from the maximum bubble size to a critical bubble-void transition size.

In general the buildup of large concentrations of lattice sinks and the resulting decrease in net vacancy and helium fluxes eventually terminates void nucleation except by the relatively slow growth of some bubbles to very large sizes.

The growth of voids is treated in terms of the growth (or shrinkage) rate from one size class to another. At quasi-steady state swelling, dislocation microstructures can equilibrate.

Microchemical changes are approximately accounted for by calculating average net solute fluxes to the various sinks--viz. a cluster in a certain size class accrues a specific average number of solute atoms (or solute - point defect complexes). This treatment assumes that the sinks serve as the principal segregation and precipitation sites. Any combination of sink strengths, rate limiting kinetics and the like can be specified in the model, and local chemistry effects as

well as overall sink structure can be accounted for. Equations to describe precipitate redistribution are also included in the model.

Clearly, a model of this complexity requires a significant long term development effort. In addition to important information gained using the simpler models described previously, data from carefully designed experiments is critically needed; indeed an iterative cycle of model development-experiment-model refinement is implicitly assumed in this research. Ultimate validation and calibration will take place in the high energy facility most like a fusion environment.

Fig. (8) shows some results of preliminary calculations using the composite model, albeit under relatively simplified conditions where effects such as collisional coalescence and microchemistry are not treated. These results illustrate the ability of the composite model to treat the highly interactive and correlated phenomena associated with microstructural evolution.

B. Mechanical Properties

1. Introduction

In-service mechanical property degradation leading to failure of fusion first wall structures is potentially one of the most serious technological obstacles to commercial fusion power. The need to have sufficient mechanical property data to make alloy development decisions is confronted by three problems: the lack of proper test environment; the extremely limited volume of the most proper environments in high energy neutron facilities; and the general difficulty in relating standard mechanical tests to structural failure.

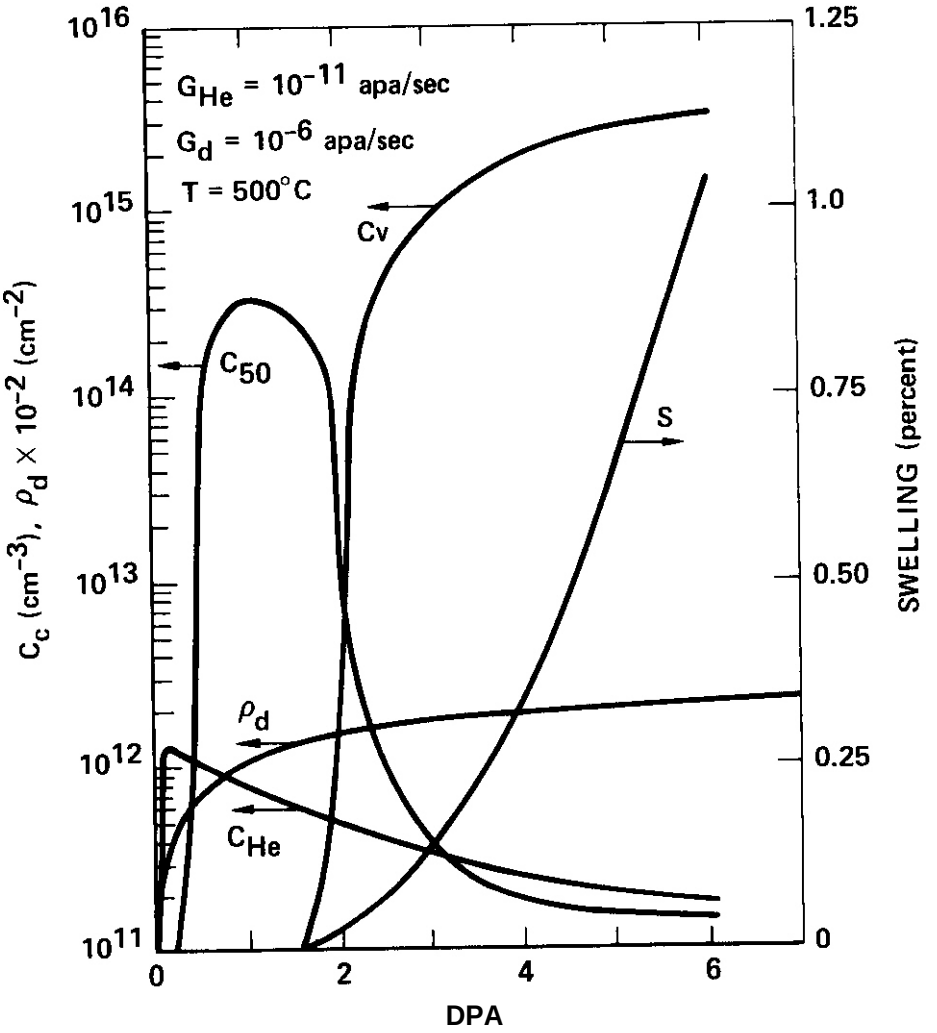

FIGURE 8. Illustration of Composite Model Calculation Results.

This research addresses these problems with a dual strategy of developing a better understanding of the relationship between microstructure and basic mechanical properties (e.g. tensile flow behavior); and basic properties and failure. Three general classes of analytical tools will be used: micromechanical models of flow and fracture; flow, failure and corresponding microstructure maps; and failure analysis methods (including, eventually, use of finite element methods to analyze and apply test data).

2. The Influence of Irradiation Microstructure on Flow Properties

A reasonable starting point for analysing the relationship between damage microstructure and mechanical properties is the 300 series austenitic stainless steels since there is a significant data base for both microstructural and mechanical property data in this alloy class. This effort also provides an initial basis for developing the high strain rate portion of the deformation - failure maps for Path A alloys and a direct linkage of property to microstructure maps.

Four distinct microstructural features were treated in the correlation model including: gas bubbles; voids; dislocation loops; network dislocations. No effort was made to treat specifically solute redistribution or phase instabilities; however, because of the strong inter-correlations in the development of other microstructural features, microchemical variations may be implicitly included as covariances in the correlations.

The microstructural features were modeled as follows: for bubbles (b), voids (v), and loops (a) a radius-density parameter $rN_{b,v,\ell}$ was defined in parametric forms $f_{b,v,\ell}(T,dpa)$ approximating data trend curves and/or model based predictions of microstructural development.

Similarly, the total network dislocation density $\rho_n = f_n(T, dpa)$ was determined from the data base or equivalent model predictions. Some illustratives plots of these parametric functions are shown in Fig. (9).

These parametric microstructure models were then combined with simple dislocation hardening models to predict yield stress changes as

$$\sigma_{ys} = \sqrt{\left[\sum_i \frac{G_b\sqrt{2Nr_i}}{\beta_i}\right]^2} + K\sqrt{\rho_n} + \sigma^0_{ys} \qquad (1)$$

where G is the shear modulus, b the Burgers vector, β_i strength parameter for obstacle **i**, K an empirical network dislocation strengthening constant and σ^0_{ys} the initial yield stress. Linear superposition was used to combine contributions from both short plus long and long plus long range strengthening components. A root mean square superposition was used to find the total contribution of short-range obstacles. The temperature dependent empirical value of K was estimated by using strength differences between solution annealed and cold worked steel in the unirradiated condition. Thermal recovery of cold work during testing at higher temperatures was accounted for.

The parameters for β were roughly consistent with current theory for the strength of different types of obstacles; $\beta_b = 5$, $\beta_v = 1$, $\beta_\ell = 3$.[12]

Fig. (10) illustrates some model prediction/experimental comparisons at approximately ($T_I = T_T = T \pm 30°C$) 400 and 550°C along with individual contributions from the various microstructural features.[12] The agreement is rather good in terms of both the shape and

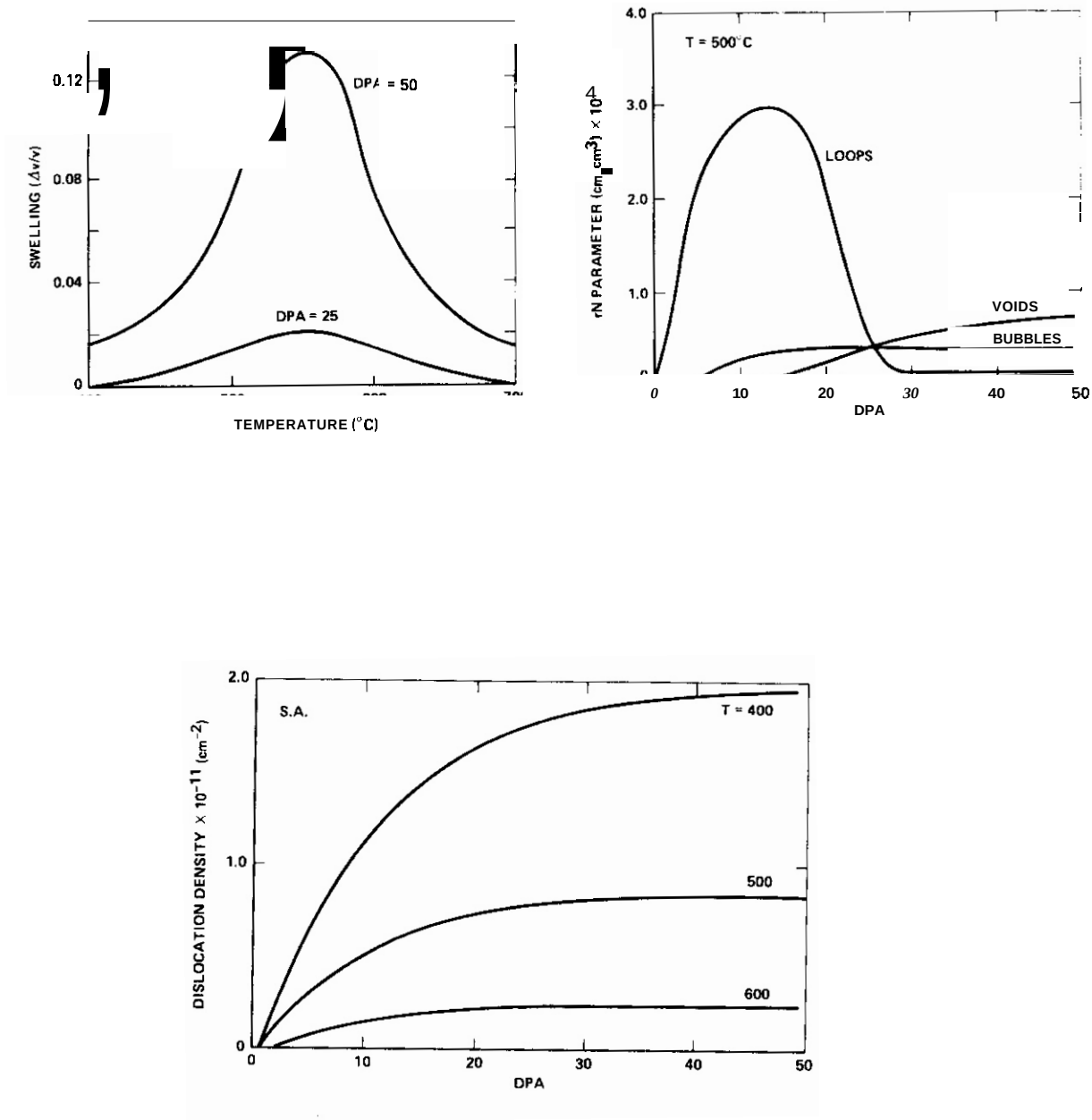

FIGURE 9. Examples of Parametric Microstructure Models Used in Mechanical Property - Microstructure Correlation Study.

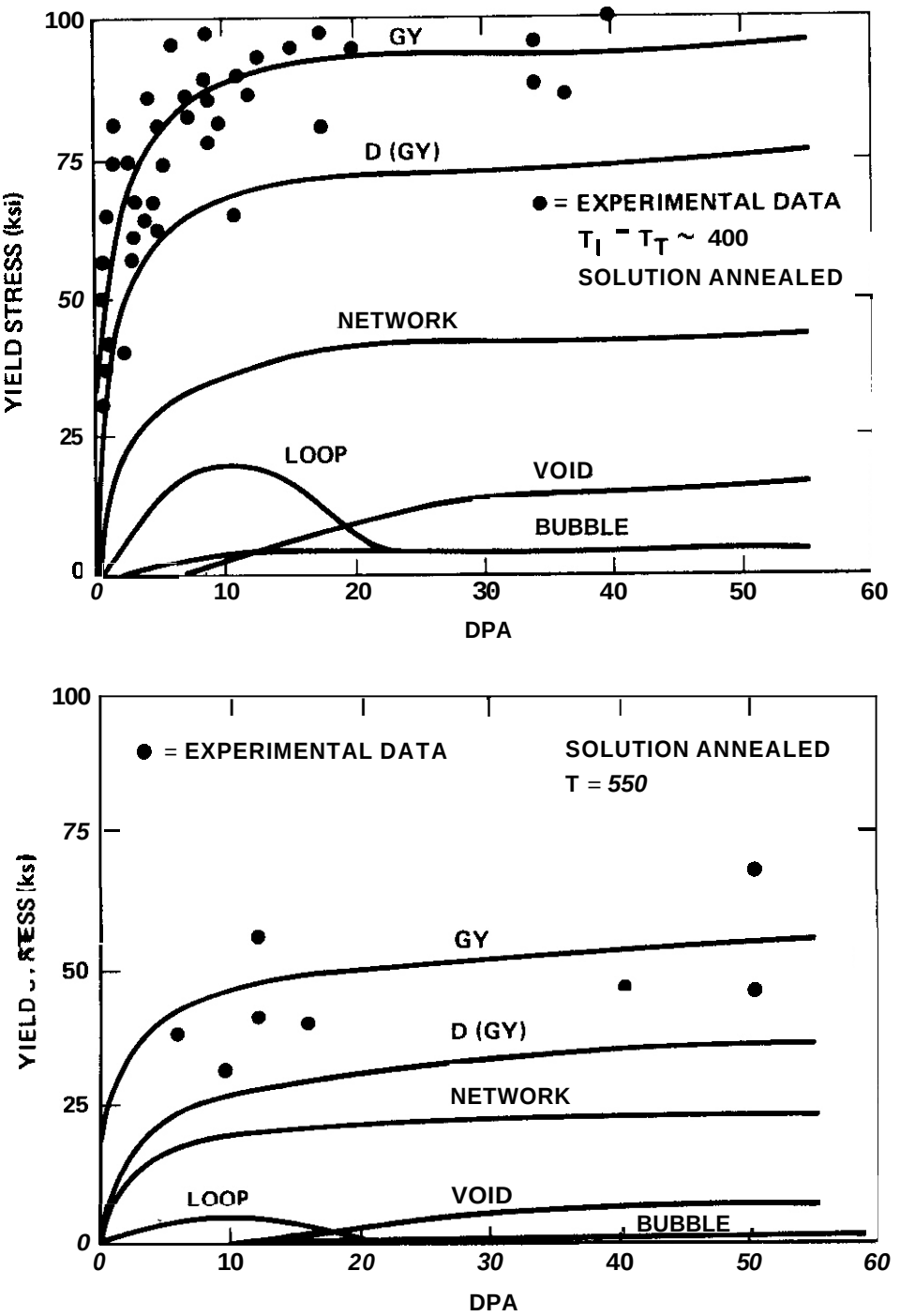

FIGURE 10. **Model Prediction - Experiment Comparisons for the Yield Stress of Solution Annealed Stainless Steel.**

magnitude of the model curves. The calculations also suggest that the network dislocations provide the major contribution to strengthening, and that the continuation void swelling beyond the point where both cavity densities and dislocation structure have equilibrated, contributes little to increased yield strength.

Fig. (11) shows model calculations for cold-worked steels; data points are plotted as small numbers which indicate both the approximate irradiation temperature and dose. Again the agreement between the model predictions and experimental observations is very encouraging. A summary of predicted versus measured [14] yield stress changes for both cold worked and solution annealed curves over a wide range of temperatures and exposures is shown in Fig. (12).

VII. REFERENCES

1. A. Taylor, D.I. Potter, H. Wiedersich, J.R. Wallace, H.A. Hoff and D.G. Ryding, "Investigation of Pulsed-Ion Irradiation on Void Microstructure", CTR Quarterly Progress Report, ANL/CTR/TM-39, pp. 18-22, Argonne National Laboratory, Argonne, I11., April 1975.

2. G.R. Odette and R. Myers, "Void Nucleation in Pulsed Irradiation Systems", Controlled Thermonuclear Research Quarterly Progress Report, HEDL/TME-75-90, pp. 2-19, Hanford Engineering Development Laboratory, Richland, WA, July 1975.

3. L.K. Mansur, "Void Swelling in Metals and Alloys Unver Irradiation: An Assessment of the Theory", Nucl. Tech. 40-1, pp. 5-34, (1978).

4. G.R. Odette and M.W. Frei, "Potential Effects of Interaction Between Transmutants and Displaced Atoms in Controlled Thermonuclear Reactor First Walls", Proc. of the First Topical Meeting on the Technology of Controlled Nuclear Fusion CONF-74-0402-PZ, 2, pp. 485-499 (1974).

5. G.R. Odette and S.C. Langley, "Modeling of Synergistic Effects of Displaced Atom and Transmutant Damage in Fission and Fusion Environments". Proceedinas of the First International Conference on Radiation Effects and Tritium Technology for Fusion Reactors, CONF-750989-P1, pp. 395-416 (1976).

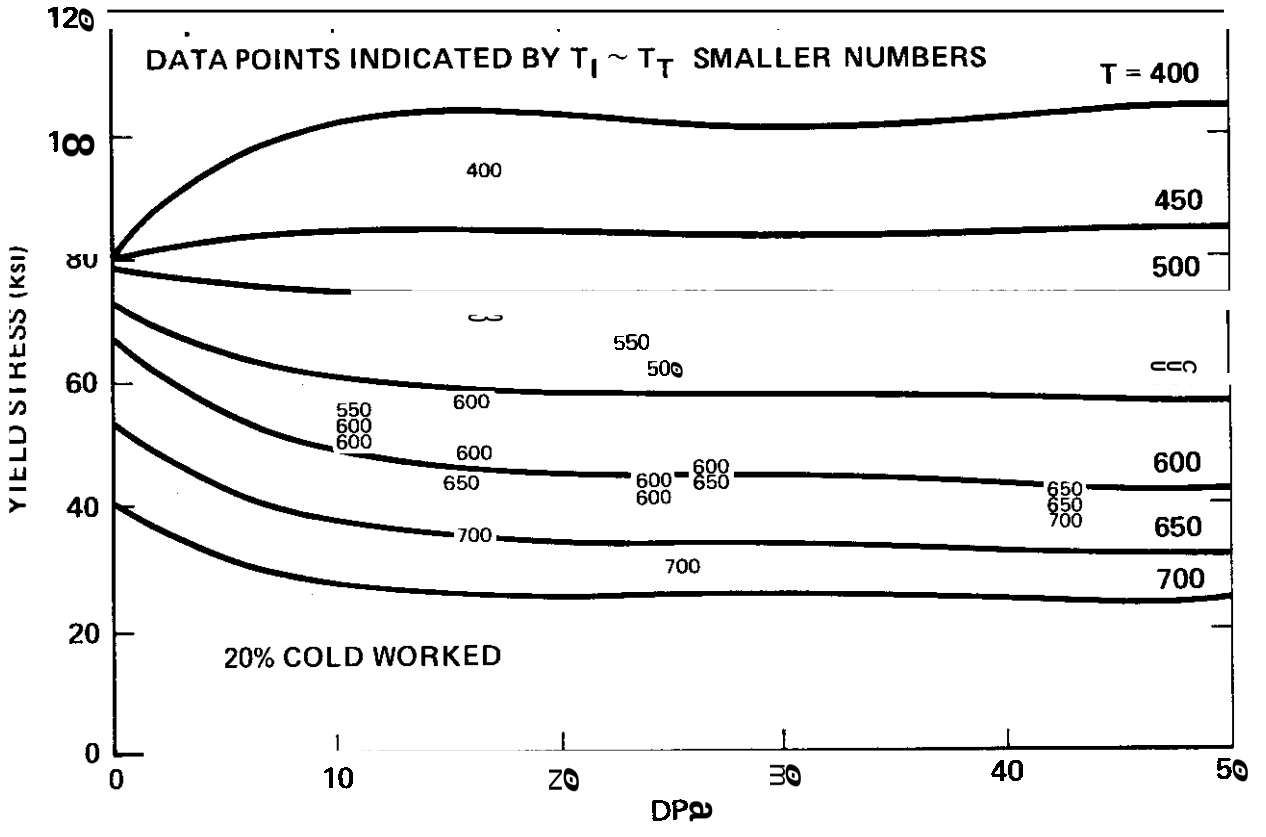

FIGURE 11. Model Prediction - Experiment Comparison for the Yield Stress of 20% Cold Worked 316 Stainless Steel.

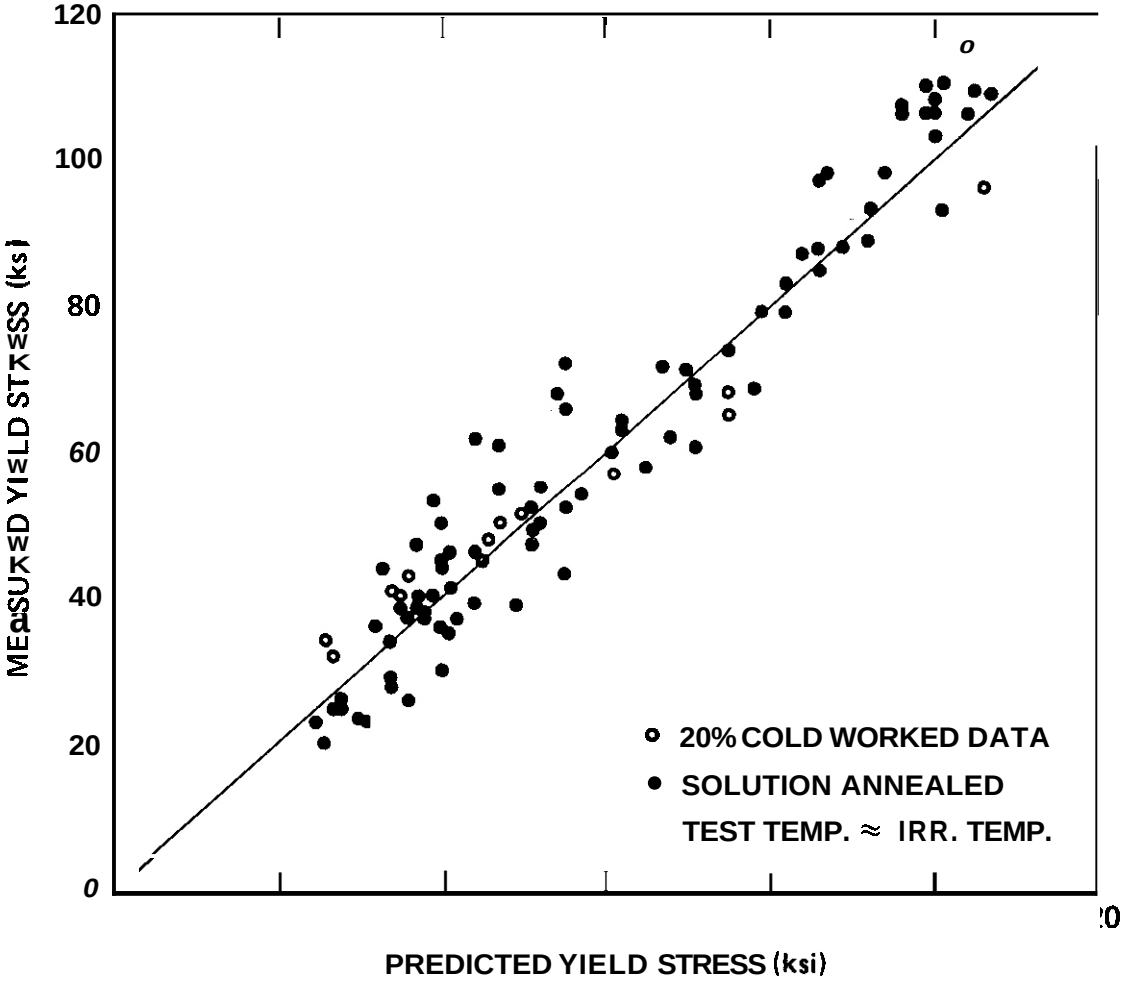

FIGURE 12. **Comparison of Predicted and Measured Yield Stresses for a Range of Temperatures and Neutron Fluences.**

6. A.D. Brailsford and R. Bullough, "The Rate Theory of Swelling Due to Void Growth in Irradiated Metals", J. Nucl. Mat. 44, pp. 121-135 (1972).

7. W.K. Appleby, E.E. Bloom, J.E. Flinn, F.A. Garner, "Swelling in 300-Series Stainless Steels", Radiation Effects in Breeder Reactor Structural Materials, M.L. Bleiberg and J.W. Bennett, Eds, pp. 509-528, The Metallurgical Society of AIME (1978).

8. J.I. Bramman, C. Brown, J.S. Watkin, C. Cawtrone, E.J. Fulton, P.J. Barton and E.A. Little, "Void Swelling and Microstructural Change in Fuel Pin Cladding and Unstressed Specimens Irradiated in DFR". Ibid., pp. 479-508.

9. J.S. Watkin, J.H. Gittus and J. Strandring, "The Influence of Alloy Constitution on the Swelling of Austenitic Stainless Steels", Ibid., pp. 467-479.

10. H.R. Brager, F.R. Garner, E.R. Gilbert, J.E. Flinn and W.G. Wolfer, "Stress Effected Microstructural Development and the Creep-Swelling Interrelationship", Ibid., pp. 727-753.

11. P.J. Barton, B.L. Eyre and D.A. Stow, "The Structure of Fast Reactor Irradiated Solution Treated AISI Type 316 Steel", J. Nucl. Mat. 67 pp. 181-197, (1977).

12. D. Bement, "Fundamental Materials Problems in Nuclear Reactors, Proceedings of the Second International Conference on the Strength of Metals and Alloys", 2, American Society for Metals, pp. 623-728 (1970).

13. J.J. Holmes, A.J. Lovell and R.L. Fish, "Ductility of Irradiated Type 316 Stainless Steel", Effects of Irradiation on the Structure and Properties of Alloys, STP-529 pp. 383-398, American Society for Testing and Materials (1974).

14. R.L. Fisher and J.D. Watrous, "Effect of Fast Reactor Irradiation on Tensile Properties of 20 Percent Cold Worked Type 316 Stainless Steel", Irradiation Effects on the Microstructure and Properties of Metals pp. 91-100, American Society for Testing and Materials (1976).

VIII. FUTURE WORK

A. Microstructural Evolution

Continued efforts will be directed at improving all of the microstructure models discussed previously; particular emphasis will be placed on facilitating physical interpretation of the results and comparisons of the model predictions with experimental observations--viz. efficiently defining physically valid regions of MPS. The simpler models will still be used for scoping studies of MPS, and for designing and interpreting new experiments. For example, the MFE-II DAFS experimental matrix and an experimental HVEM study of pulsing were, in part, designed using these models. Continued effort to implement more fully the components of the composite model in a computationally tractable manner will also be a high priority goal.

B. Mechanical Properties

The models relating flow properties to microstructure are being extended to treat tensile ductility parameters such as uniform elogation. An effort will be made to relate the microstructural features to the "hardness" parameter which has been used to effectively define equations of mechanical state for both unirradiated and irradiated stainless steels. The basic physical processes leading to an effective equation of state-microstructure relationship will be carefully studied, with emphasis on integrating strengthening, work hardness and flow localization mechanisms.

Micromechanical models will be applied to relate basic properties and micro structure to failure-related properties such as fracture toughness, fatigue strength and crack growth resistance. In addition, models of grain boundary failure in the creep regime including

the influence of helium, matrix hardening, stress relaxation and the like are being assembled. These models and the available data base will be used to develop microstructure - flow and failure maps for the entire range of temperature and stresses of interest. An assessment of the influence of extrinsic parameters such as stress state and stress concentrations related to macroscopic defects (i.e. cracks) will also be initiated. Finally the modeling and analytical effort will consider what constitutes appropriate failure criteria and test procedures for fusion first wall structures - e.g. plastic instability or fracture toughness.

An experimental program currently centered around utilization of the RTNS-II facility has been recently initiated in collaboration with HEDL and LLL. This effort is not only aimed at designing, conducting and interpreting RTNS-II experiments, but also .developing new test techniques for the fusion program. In particular, an effort is under way to develop quantitatively useful microminiaturized mechanical tests, with initial emphasis on instrumented hardness.

XI. PUBLICATIONS

None during the last reporting period

I. PROGRAM

Title: Irradiation Effects on Fusion Reactor Structural Materials
Principal Investigator: J. A. Sprague
Affiliation: Naval Research Laboratory

II OBJECTIVE

The objectives of this work are to examine the effects of composition on phase stability of neutron-irradiated titanium alloys and to study the effects of major element composition and helium generation rate on the tensile behavior of simple iron-nickel-chromium alloys.

III. RELEVANT DAFS PROGRAM PLAN TASK/SUBTASK

TASK II.C.1 Effects of Material Parameters on Microstructure
TASK II.C.7 Effects of Helium and Displacement on Flow
TASK II.C.8 Effects of Helium and Displacement on Fracture

IV. SUMMARY

Electron microscopy foils of a series of titanium alloys and tensile specimens of a series of iron-.nickel-chromium ternary alloys were inserted in an irradiation assembly in the EBR-II reactor. The titanium alloys are intended to examine the effects of atomic misfit on solute segregation and phase stability. The iron-nickel-chromium alloys will be used to study the effects of helium and microstructure on tensile behavior.

V. ACCOMPLISHMENTS AND STATUS

A. DAFS Test Matrix for the EBR-II Reactor Experiment - J. A. Sprague (NRL) and R. W. Powell (HEDL)

1. Introduction

In June 1978 the Fusion Reactor Materials Program inserted an irradiation assembly in the EBR-II reactor. The target conditions for this experiment were two peak fluences, 5 x 10^{22} n/cm^2 (E>0.1 MeV) and 10 x 10^{22} n/cm^2 (E>0.1 MeV), at each of three temperatures, 400, 450, and 550°C. This report describes the specimens included in the DAFS portion of the experiment and explains the rationale behind these tests.

2. Titanium Alloys

The objective of this portion of the experiment was to examine the segregation of several solute atoms in titanium under neutron irradiation and to study the resultant phase transformations. Recent theoretical[1,2] and experimental[3,4] investigations of irradiation-induced solute segregation in face-centered-cubic (fcc) alloys have indicated that substitutional solute atoms which are smaller than the atoms of the solvent lattice can trap self-interstitial atoms, forming mobile complexes. The migration of these complexes to point defect sinks can cause increased solute concentrations, and possibly precipitation, in the regions near the sinks. If similar results hold for the hexagonal-close-packed (hcp) and body-centered-cubic (bcc) lattices of the a-and β-phases of titanium, then irradiation-induced solute segregation should occur in most commercial Ti-alloys, since most of the commonly used alloying elements have a negative misfit. As used here, misfit is defined as the fractional change in lattice parameter(s) of a solid solution alloy per atom fraction of solute.[3]

To study the effect of solute size on the stability of titanium alloys, two a-stabilizing elements, aluminum and tin, and two 8-stabilizing elements, vanadium and niobium, were chosen. Their atomic misfits in titanium are given in Table 1.[5]

TABLE 1

ATOMIC MISFITS OF ALLOYING ELEMENTS IN Ti

Element	α Phase a-axis	α Phase c-axis	β Phase
Al	∿0%	-6%	--
Sn	+10%	∿0%	--
V	-3%	-6%	-6%
Nb	--	--	∿0%

The following alloys were prepared by arc-melting 129 buttons in a gettered argon atmosphere (compositions in wt.%):

1. Ti-3%Al
2. Ti-6%Al
3. Ti-6%Sn
4. Ti-12%Sn
5. Ti-2%V
6. Ti-4%Nb
7. Ti-6%Al-10%Nb
8. Ti-6%Al-20%Nb
9. Ti melt control

In addition to these alloys, an extra low oxygen (0.06 wt.%) heat of Ti-6%Al-4%V and high purity Ti were included in the experiment.

Electron microscope foils of the Ti-3A1, Ti-6Sn, Ti-12Sn, Ti-2V, Ti-4Nb, Ti melt control, and high purity Ti were prepared by cold rolling to a thickness of 0.4 mm and punching 3 mm-dia. disks. Due to difficulties in cold rolling, the Ti-6A1, Ti-6Al-10Nb, and Ti-6Al-20Nb were hot forged at 600°C to rods 5 cm long and 6 mm in diameter. These rods were then

turned to 3 mm diameter. Disks, 0.4 mm thick, were sliced from these rods following heat treatment (described below). The Ti-6Al-4V was prepared from previously heat-treated stock by turning to 3 mm-dia. rod and slicing 0.4 mm disks.

Due to the variety of alloy compositions, several different heat treatments were used. The Ti melt control, high purity Ti, Ti-3A1, Ti-6A1, Ti-6Sn, and Ti-12Sn were annealed in vacuum (less than 10^{-6} torr) at 800°C for two hours, followed by a "fast cool" (furnace removed from furnace tube). The Ti-2V and Ti-4Nb were vacuum-annealed at 700°C for four hours, followed by a furnace cool. The Ti-6Al, Ti-6Al-10Nb, and Ti-6Al-20Nb were vacuum-annealed as 3 mm-dia. rods at 1040°C for 30 minutes, followed by a fast cool, and then at 720°C for two hours, followed by a fast cool. This heat treatment was the approximate equivalent of the commercial 8-anneal for Ti-6Al-4V, the condition in which the stock of that alloy was supplied.

To allow for three specimens at each irradiation condition and three archive specimens, a total of 21 disks of each material were shipped to HEDL, where they were marked for identification and loaded into the reactor experiment assembly.

3. Fe-Ni-Cr Tensile Test Specimens

These specimens were included to study the effects of microstructure and helium generation rate on the tensile behavior of Fe-Ni-Cr alloys. The nickel and chromium contents were varied to produce different levels of swelling and helium production. Comparisons with identical specimens to be inserted in the Oak Ridge Research Reactor (ORR) will provide similar information at much higher helium generation rates.

The nominal compositions (in wt.%) of the five alloys included in this portion of the experiment are given in Table 2. Nickel content varied from 25% to 45% at a constant chromium level of 15% while chromium content ranged from 7.5% to 20% at a constant nickel level of 35%.

TABLE 2

COMPOSITION MATRIX OF Fe-Ni-Cr TENSILE SPECIMENS

	Fe-25%Ni-15%Cr	
Fe-35%Ni-7.5%Cr	Fe-35%Ni-15%Cr	Fe-35%Ni-20%Cr
	Fe-45%Ni-15%Cr	

The increased nickel contents will produce decreased swelling and increased helium production while increased chromium levels will produce increased swelling at a constant helium production rate. In addition, nearly constant swelling is expected in some alloys with significantly different helium generation rates (viz., low nickel and low chromium versus high nickel and high chromium). The effect of these variations on the tensile behavior will be determined from this experiment.

Three duplicate specimens of each alloy were included for each of the three irradiation temperatures and two fluences. The temperatures are the same for the overall experiment but, due to the axial position of the tensile specimen subcapsules, the target fluences for these specimens are 2.5 x 10^{22} n/cm^2(E>0.1 MeV) and 5 x 10^{22} n/cm^2 (E>0.1 MeV).

The heat treatments were identical for all specimens and were designed to develop a small grain size relative to the specimen thickness. The treatment consisted of a vacuum anneal at 950°C for fifteen minutes following 30% cold work.

VII. REFERENCES

1. R. A. Johnson and N. Q. Lam, "Solute Segregation in Metals Under Irradiation," Phys. Rev. B13, p. 4364 (1976).

2. R. A. Johnson and N. Q. Lam, "Solute Segregation to Voids During Irradiation," Phys. Rev. B15, p. 1794 (1977).

3. L. E. Rehn, P. R. Okamoto, O. I. Potter and H. Wiedersich, "Effect of Solute Misfit and Temperature on Irradiation-Induced Segregation in Binary Nickel Alloys," J. Nucl. Mat. 74, p. 242 (1978).

4. H. R. Brager and F. A. Garner, "Dependence of Void Formation on Phase Stability in Neutron-Irradiated Type 316 Stainless Steel," Proceedings of 9th ASTM International Symposium on Effects of Radiation on Structural Materials, Richland, Washington, 1978, American Society for Testing and Materials, to be published; Hanford Engineering Development Laboratory Report HEDL-SA-1412, 1978.

5. W. B. Pearson, Handbook of Lattice Spacings and Structures of Metals and Alloys, pp. 872-878, Pergammon Press, New York, 1958.

VIII. FUTURE WORK

A schedule for examination of specimens will be established following the first interim discharge of the experiment.

IX. PUBLICATIONS

None.

I. PROGRAM

Title: Effects of Irradiation on Fusion Reactor Materials
Principal Investigator: F. V. Nolfi, Jr.
Affiliation: Argonne National Laboratory

II. OBJECTIVE

The objective of this work is to determine the microstructural evolution, during irradiation, of first-wall materials with special emphasis on the effects of helium production, displacement damage and rates, and temperature.

III. RELEVANT DAFS PROGRAM PLAN TASK/SUBTASK

SUBTASK II.C.2.1 Mobility, Distribution, and Bubble Nucleation

IV. SUMMARY

The microstructure of Ti-64, which was single and dual-ion irradiated at temperatues between 450 and 650°C, has been examined by TEM. Profuse irradiation-induced precipitation of 6-phase platelets occurs in all samples. Cavities form in all dual-ion irradiated samples and also in the single-ion irradiated specimen at the highest temperature. Precipitation appears to be independent of dose from 3-25 dpa and independent of helium content, but is strongly temperature dependent; the precipitate size increases and the number density decreases with increasing temperature. For cavities, the size and number density both increase with the addition of helium, and swelling is low; the maximum swelling observed in *any* sample was -0.6% at 25 dpa.

Samples of Fe-20Ni-15Cr and Type 316 stainless steel have been dual-ion irradiated, and also pre-injected and single-ion irradiated. The

Fe-20Ni-15Cr is for a dose dependence study at low dose rate ($3x10^{-4}$ dpa $\cdot s^{-1}$). Studies of the temperature, dose and helium injection rate dependencies will be performed on the Type 316 stainless steel.

V. ACCOMPLISHMENTS AND STATUS

Microstructure of Irradiated Fusion Reactor First-wall Materials — G. Ayrault

A. Radiation Damage in Ti-64 (in collaboration with McDonnel-Douglas Astronautics Corporation)

Titanium alloys have been suggested as candidate structural materials for fusion reactors. However, information regarding their response to displacement-producing radiation is sparse, and is nonexistant for concurrent high helium production. Here we report TEM observations of radiation microstructural evolution in the first of a set of three commercial titanium alloys, Ti-64, Ti-811 and Ti-15333.

1. Experimental Procedure

Ti-64 (6wt % Al, 4 wt % V) is an α-β alloy containing an HCP, α-phase (stabilized by Al) and a BCC, β-phase (stabilized by V). The samples used in this study were annealed at 925°C for 4 hours, which yielded a microstructure consisting of large (~10μ) equiaxed grains of primary a, along with some smaller transformed β-grains.[1,2] The samples were single-ion irradiated with 2.4-MeV V^+ ions and also dual-ion irradiated with 2.4-MeV V^+ ions and degraded 0.95-MeV ^3He ions in the ANL Dual-Ion Irradiation Facility.[3] Single-ion doses ranged from 3-25 dpa, and the dual-ion samples were irradiated to a fixed dose of 25 dpa with 10:1 appm He:dpa ratio. In both cases, the nominal irradiation temperatures were 450, 550, and 650°C; actual irradiation temperatures were read for all samples with an infrared pyrometer.

2. Precipitates

The most prominent microstructural change in irradiated specimens is profuse precipitation of β-platelets shown in Figs. 1 and 2. The crystallographic orientation of the β-platelets with respect to the matrix obeys the Burgers orientation relationship:

$$(0001)\alpha \parallel (011)\beta$$

$$\langle 1\bar{2}10\rangle \parallel \langle 11\bar{1}\rangle\beta$$

Precipitation occurs at 450, 550, and 650°C in irradiated samples, but is not observed in unirradiated control samples having the same thermal history.

The precipitate sizes and number densities are strongly temperature dependent — the size increases with increasing temperature, and the number density decreases. Figure la is a dark field micrograph from an $(0\bar{1}1)$ precipitate reflection in the 25 dpa, single-ion sample irradiated at 465°C. Six equivalent orientations are allowed by the Burgers orientation relationship; in this micrograph only one is seen so that ~1/6 of the precipitates are visible. Larger precipitate sizes and lower number densities are found in the 12 dpa sample irradiated at 547°C, Fig. Ib. Again, only one of the six possible precipitate orientations is in strong contrast. Similar large changes in precipitate structure are seen in going to 660°C at 25 dpa, Fig. lc. Different diffraction conditions have put all six precipitate orientations in strong or weak (but visible) contrast in this micrograph.

A roughly corresponding set of dual-ion samples is shown for comparison in Fig. 2. Figures 2a and 2b show ~1/6 of the precipitates, and in Fig. 2c all the precipitates are in contrast. The specimen shown in Fig. 2a was actually irradiated at 541°C, not 450°C, as a result of

beam-heating. The precipitate size and number density are intermediate between those of the 465°C and 547°C single-ion samples shown in Figs. la and lb. Similarly, the precipitate structure of the dual-ion specimen irradiated at 624°C, Fig. 2c, is intermediate between those of the single-ion samples irradiated at 547°C and 660°C, Figs. lb and lc. The dual-ion precipitate structure at 556°C, Fig. 2b, is essentially the same as that of the single-ion sample at 547°C, Fig. lb.

These observations suggest the following qualitative pattern of precipitation: Precipitate size increases rapidly with temperature and number density decreases. Little or no difference exists between single and dual-ion irradiated samples; any differences that do exist are within a range attributable to differences in irradiation temperature. A similar qualitative statement can be made about the dose dependence of precipitation in single-ion irradiations: There is no obvious difference in precipitate size and number density between the lowest (3 dpa) and highest (25 dpa) dose **samples.**

3. Cavities

Cavities are formed during single-ion irradiation at 660°C, Fig. lc, and at all three (541, 556 and 624°C) dual-ion irradiation temperatures, Fig. 2 (the cavities are not visible in Fig. 2a because of contrast conditions). For single-ion irradiated samples at 660°C, the cavity number density is ~2×10^{13} cm^{-3} and the swelling ($\Delta V/V$) is ~0.07%; the mean cavity diameter is $\bar{D} \simeq 300$ Å. At 624°C, dual-ion irradiation produces a higher cavity number density, ~4.5×10^{13} cm^{-3}, larger cavity size, $\bar{D} \simeq 490$ Å, and swelling of the order of ~0.6%. In addition a tendency towards preferential formation of cavities along grain boundaries, Fig. 3, occurs in dual-ion irradiated samples but not in single ion. This effect is not included in the quantitative determination of cavity sizes and number densities - all measured regions were within grains. For dual-ion irradiations at 556°C, the number density ~7×10^{14}, $\bar{D} \simeq 60$ Å, and the swelling is ~0.02%. These numbers are approximate since many of the small cavities are near the

visibility limit and more cavities may actually exist than appear.

The cavities formed during single-ion irradiation are voids since no gas was injected. If the cavities observed in the dual-ion irradiated samples are equilibrium bubbles, the gas contained in them can be estimated if the cavities are treated as spherical. From the balance of gas pressure vs surface energy

$$p_g = \frac{8\pi}{3} \frac{\gamma}{KT} \frac{1}{V} \sum r_i^2 \quad ,$$

where p_g is the injected gas density, r_i are the measured cavity radii, and γ is the surface energy; the summation runs over all cavities in the volume, V. For $\gamma = 10^3$ ergs. cm^{-2}, a gas density of ~10 appm is required to form an equilibrium bubble distribution resembling that in the 556°C sample; for the 624°C sample ~40 appm is required. Comparing there gas concentrations to the nominal 250 appm injected He dose, it is seen that the cavities m y well be overpressured helium bubbles.

B. Dual-Ion Irradiation of Type 316 Stainless Steel

Samples of Type 316 stainless steel (MFE Ht.-15893) have been dual-ion irradiated in the ANL Dual-Ion Facility with 3.0-MeV Ni^+ ions and degraded 0.87-MeV ^3He ions; the dose rate was 3×10^{-3} dpa · s^{-1}. The material was initially 50% cold worked, then annealed at 1050°C for 1 hour and aged 10 hours at 800°C.

A dose dependence study and a temperature dependence study were carried out. In the dose dependence study, the irradiation temperature was 625°C and the doses ranged from 3-25 dpa. Helium was injected at rates of 5:1, 15:1, and 50:1 appm He:dpa. For comparative purposes, additional samples were preinjected at room temperature with 5 appm He and single-ion irradiated with 3.0-MeV Ni^+ ions at the same temperature and to the same doses as above. In the temperature dependence study, the dose and helium injection rates were held constant at, respectively, 12 dpa

and 15:1 appm He:dpa, and the irradiation temperatures were 550, 600, 650, and 700°C.

C. Dose Rate Study of Radiation Damage in Fe-20Ni-15Cr

Samples of an experimental Fe-20Ni-15Cr alloy, supplied by W. G. Johnston, have been dual-ion irradiated in the ANL Dual-Ion Facility with 3.0-MeV Ni^+ ions and degraded 0.87-MeV ^3He ions. The doses were 3-12 dpa, the dose rate $3x10^{-4}$ dpa $\cdot s^{-1}$, and the irradiation temperature was 650°C; helium was injected at a rate of 15:1 appm He:dpa. For comparative purposes additional samples were preinjected at room temperature with 5 appm He and single-ion irradiated with 3.0-MeV Ni^+ ions. The irradiation conditions and temperature were the same as above. The microstructural evolution data obtained from this experiment will be compared to that obtained from o w earlier dual-ion irradiation study of this alloy[4] carried out at 700°C and a dose rate of $3x10^{-3}$ dpa $\cdot s^{-1}$. The lower irradiation temperature in the present study corresponds to the lower dose rate.

VI. REFERENCES

1. J. W. Davis, ADIP Quarterly Progress Report for Period Ending March 31, 1978.

2. J. W. Davis, S. M. L. Sastry and L. J. Pionke, ADIP Quarterly Progress Report for Period Ending June 30, 1978, p. 85.

3. A. Taylor, J. Wallace, D. I. Potter, D. G. Ryding and B. Okray Hall, Proc. Intl. Conf. on "Radiation Effects and Tritium Technology for Fusion Reactors," Vol. I, p. 158, 1975.

4. S. Agarwal and G. Ayrault, DAFS Quarterly Progress Report for Period Ending March 31, 1978, p. 135.

VII. FUTURE WORK

1. TEM examinations of single and dual-ion irradiated Ti-811 and Ti-15333 are in progress.

2. TEM examinations of preinjected single-ion and dual-ion irradiated Fe-20Ni-15Cr and Type 316 stainless steel are in progress.

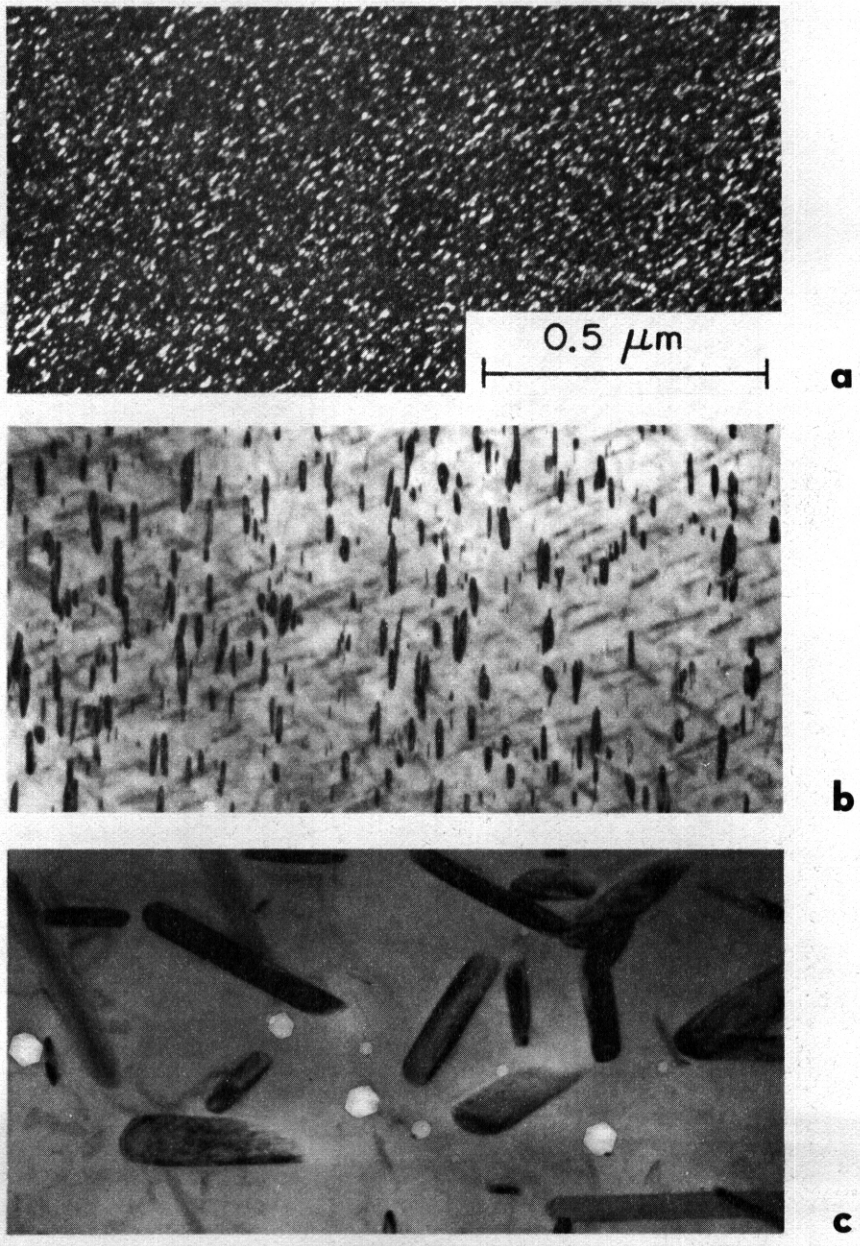

Fig 1. Single-ion irradiated Ti64 (a) Dark field-465°C, 25 dpa (b) Bright field-547°C, 12 dpa (c) Bright field-660°C, 25 dpa.

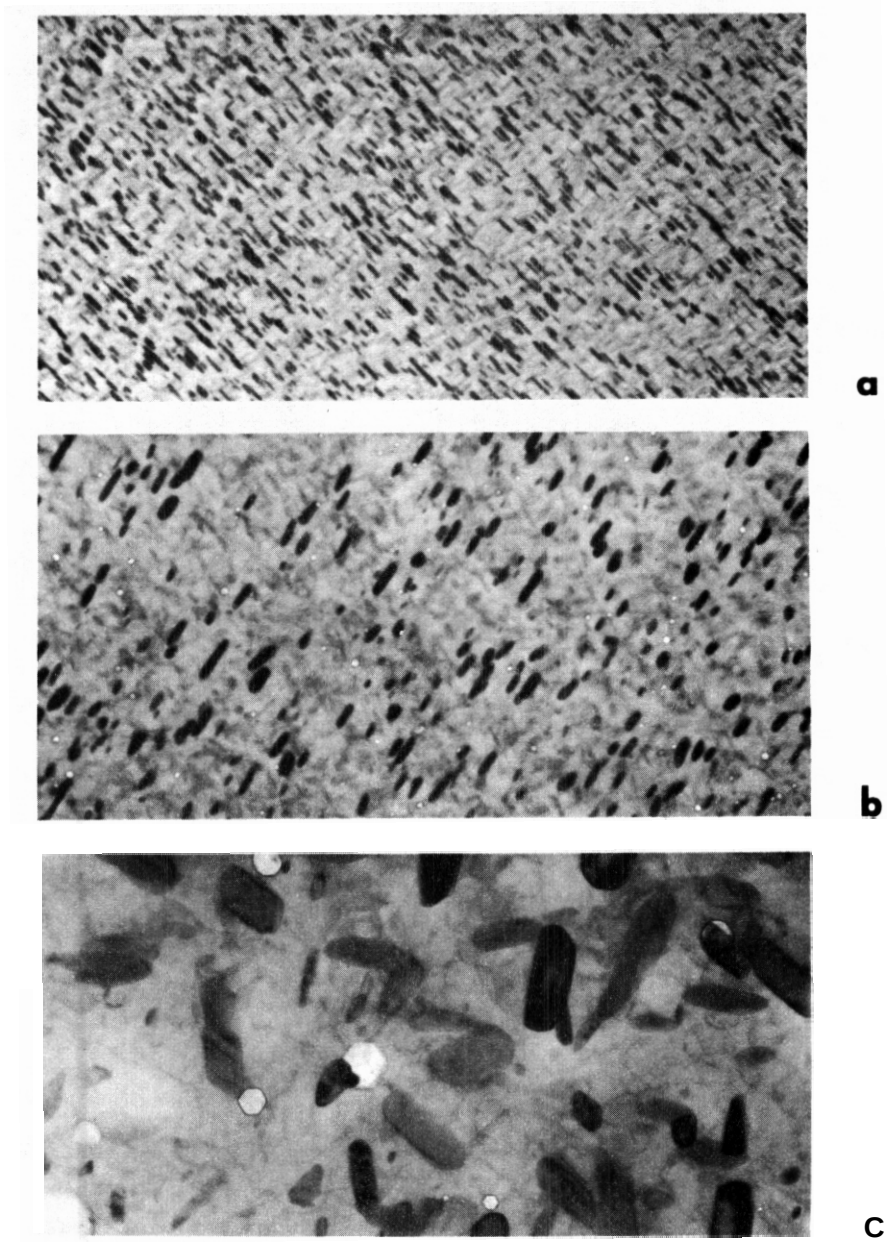

Fig. 2: Dual-ion irradiated Ti 64-25 dpa, 10:1 He: dpa ratio (a) 541°C (b) 556°C (c) 624°C.

Fig. 3: Preferential formation of cavities at grain boundary in Ti64 dual-ion irradiated at 624°C.

I. PROGRAM

Title: Irradiation Response of Materials

Principal Investigators: J. A. Spitznagel, W. J. Choyke

Affiliation: Westinghouse Research and Development Center

II. OBJECTIVE

The objective of this work is to assess the phenomenology and mechanisms of microstructural evolution in materials exposed to simultaneous helium injection and creation of atomic displacement damage by a second ion beam.

III. RELEVANT DAFS PROGRAM PLAN TASK/SUBTASK

SUBTASK II.C.2.1. Helium Mobility, Distribution and Bubble Nucleation

IV. SUMMARY

The effects of momentum transfer, detrapping and radiation-enhanced diffusion of helium in various materials can be studied using the elastic scattering of high energy alpha particles[1,2,3] and perhaps the $^3He(d,p)\alpha$ nuclear reaction technique[4]. Previous work at the High Energy Ion Bombardment Simulation (HEIBS) Facility at the University of Pittsburgh under separate funding using the α-α scattering technique has shown that helium is very effectively trapped in 304 stainless steel following implantation. The average travel of an implanted helium atom was less than 100nm following bombardment with high energy ($\sim$2 MeV) protons or oxygen atoms to damage levels from $\sim$1 to 20 dpa at temperatures of 500-600°C[3]. Primary recoil spectra calculations were made[3] for the implanted helium atoms. These demonstrated that, while less than 1% of the helium would receive sufficient kinetic energy from knock-on events to travel 100nm

or more through the lattice, approximately 48% would have received sufficient kinetic energy to free the helium from the deepest trap imaginable ($\sim$4 eV per atom for a helium atom bound to a ledge site on a dislocation loop[5]). It was concluded that if detrapping and rapid diffusion of helium do occur under the conditions of these experiments then retrapping must occur within a few ($<5 \times 10^2$) atomic jumps and/or the mean residence time in a trap must be large relative to the duration of the ion bombardment ($\sim$12 hours).

V. ACCOMPLISHMENTS AND STATUS

Work was initiated to determine the feasibility of using the $^3He(d,p)\alpha$ nuclear reaction technique to study the effects of momentum transfer, detrapping and radiation-enhanced diffusion of helium in an ion-bombarded b.c.c. metal using the ion channeling and back-scattering apparatus at the HEIBS Facility. If adequate shielding and sufficiently low beam currents can be used to eliminate the neutron irradiation hazard, this technique will be used to study helium mobility in high purity molybdenum (model material). The nuclear reaction technique has the advantage of requiring only the 2 Mv Van de Graaff and, unlike the α-α scattering technique, does not tie up the large accelerator needed for the dual ion irradiation experiments.

VI. REFERENCES

1. A. G. Pieper and R. B. Theus, NRL Memorandum Report 2555, p. 38 (1973).

2. L. Shabason and W. J. Choyke, Nucl. Instr. and Methods, 137, p. 533 (1976).

3. W. J. Choyke, J. A. Spitznagel, J. N. McGruer and J. S. Lally, "Momentum Transfer and Damage Energy Gradient Effects on Helium Distributions in Type 304 Stainless Steel", Accepted for Publication in J. Nucl. Mater. (1978).

4. P. P. Pronko and J. C. Pronko, PHYS REV, B 9, 7, p. 2870 (1974)

5. D. J. Reed, Radiation Effects, 31, p. 129 (1977).

VII. FUTURE WORK

Range and straggle predictions for 3He in Mo using the EDEP-1 code with a variety of current electronic stopping formulations will be compared. The irradiation hazard associated with the 3He(d,p)α technique will be determined. Molybdenum specimens suitable for helium depth profiling by either the nuclear reaction or α-α scattering technique will be prepared.

VIII. PUBLICATIONS

None

I. PROGRAM

Title: In-Situ Helium Irradiation

Principal Investigators: D. Kuhlmann-Wilsdorf, W. A. Jesser

Affiliation: University of Virginia

II. OBJECTIVE

The objective of this work is to determine the effect of helium on microstructural evolution by HVEM observations during in-situ helium ion irradiations of first wall materials with emphasis on bubble nucleation and growth as correlated to the microstructure.

III. RELEVANT DAFS PROGRAM TASK/SUBTASK

Subtask II.C.2.1 Helium Mobility, Distribution, and Bubble Nucleation.

IV. SUMMARY

Dynamic in-situ HVEM observations of the evolution of helium ion radiation damage and its interaction with the existing microstructure of 316 stainless steel samples were made over a range of ion fluxes and sample temperatures.

With increasing fluence dynamic observations revealed the typical sequence of initial black-spot damage followed by bubble nucleation and growth, and finally surface deformation. At high temperatures and fluxes, bubbles at the grain boundaries were observed to have significantly larger radii and with a lower number density than those within the grains. At

lower fluxes and temperatures, no size or density variation was found. This result is presumably controlled by the sample temperature rather than the beam flux. It was observed that twin boundaries are also decorated by oversized helium bubbles. The mechanisms by which enlarged helium bubbles decorate microstructural features is under investigation.

Blistering and exfoliation of the surface were observed dynamically during in-situ experiments. We believe this is the first time such dynamic transmission electron microscope observations have been reported.

V. ACCOMPLISHMENTS AND STATUS

A. In-situ HVEM Studies of Helium Irradiated Stainless Steel - - J. L Bennetch, L. S. Horton, and W. A. Jesser, (University of Virginia, Charlottesville, VA)

1. Introduction

In the experimental set-up described previously in DAFS reports[1,2] 3 mm electropolished 316 stainless steel samples have been bombarded by He^+ ions with energies up to 80 keV and fluxes up to 1.5×10^{15} ions/cm^{2}sec. The ion irradiations were performed in-situ, within a 500 kV HVEM, or in the drift tube of the accelerator attached to the microscope. The evolution of the helium radiation induced microstructure was continuously observed during the bombardment in the HVEM and after bombardment the samples were examined in a high resolution Philips EM *400* Transmission Microscope. Dynamic in-situ observations were recorded using a video system. Surfaces of the irradiated samples were examined in a JEOL JSM 35 microscope.

During the course of a high flux experiment, three distinct stages of microstructure are observed, black spot damage, bubble nucleation and growth, and surface deformation. If a high flux is employed, the evolution is too rapid for convenient examination of the individual stages. In order to investigate the full range of microstructural changes caused by the ion bombardment, it was necessary to conduct the experiments in the following three stages. In the first stage, low ion flux experiments from ambient temperature to about 500°C were performed both in-situ and within the drift tube. The primary result observed is black spot damage. The second stage of experiments involved higher ion fluxes and somewhat higher temperatures. Fluences in these experiments were chosen so as to permit studies of the nucleation and growth of gas-filled voids. The last stage of experiments and microstructural evolution are observed under the highest flux conditions which results in ion induced surface deformation.

2. Experimental Data and Results

a. Low Flux Experiments - In these experiments, 3 mm electropolished samples were irradiated with helium ions at fluxes of approximately 10^{13} ions/cm2sec or less and with sample temperatures of less than 500°C. After a critical dose of helium was reached, tiny black spots, presumed to be interstitial loops, were observed to form. Increased dose caused the black spot density and size to increase to a steady state value within 30 minutes of irradiation. No visible bubbles were observed even after many hours of further irradiation. Also, no major surface deformation was observed. The above result was observed over a wide temperature range. Also this result was independent of helium ion energy from 40 to

100 keV.

b. High Flux Experiments - When the helium ion beam flux is about 10^{14} ions/cm^{2}sec or greater, the rate of black spot formation is rapid and is quickly followed by bubble nucleation and growth. Irradiations over a range of ion fluxes between 10^{14} and 10^{15} ions/cm^{2}sec. and sample temperatures between a few hundred degrees celsius and about 700° C have shown that grain boundaries and twin boundaries in the 316 stainless steel are decorated by a low density of large bubbles while the other regions within the grain contain a high density of small bubbles.

Figure 1 shows a transmission electron micrograph of a sample irradiated with helium ions at a flux near 1.5×10^{15} ions/cm^{2}sec and a sample temperature of approximately 650°C in the electron thin area of the sample. The bubbles along the grain boundaries had an average diameter of about 900 Å. Bubbles on the twin boundaries were also oversized while the average diameter of the bubbles in the grain was near 170 Å. The total ion dose of the sample was approximately 7×10^{17} ions/cm^2.

A similar enlargement of grain boundary bubbles is seen in figure 2. This sample was irradiated with a sample temperature of approximately 650° C and with an ion flux of approximately 6×10^{14} ions/cm^{2}sec. The average diameter of bubbles along the boundary is 110 Å while that of bubbles in the grain is about 40 Å. The total ion dose was approximately 3×10^{17} ions/cm2.

The dose difference between these experiments could be significant, however, the low flux and small sample thickness of the latter sample as compared to the high flux and large sample thickness of the sample shown

in figure 1 may also play a role in determining the number density and size of the bubbles. The flux, fluence and sample thickness dependenceare further being investigated.

A sample irradiated with helium ions at approximately 400° C and a flux of approximately 10^{14} ions/cm^{2}sec to a fluence of about 7×10^{17}ions/cm^2 showed bubbles of diameter 540 Å with no difference in bubble size or number density between those on grain boundaries and those within the grain.

c. High Fluence Experiments - Following bubble formation, blistering and/or exfoliation was observed in samples irradiated to a sufficiently high ion dose. Figure 3 shows a transmission micrograph of blisters in the thicker (greater than 2000 Å) area of a sample irradiated with high sample temperature and ion flux. However, exfoliation was the predominant deformation feature found over the surface. Another sample with lower flux and sample temperature is shown in the transmission micrograph of figure 4. This exfoliation occurred in an area of thickness less than 2000 Å. In both samples, blistering and/or exfoliation occurred in areas of thickness less than the projected helium range for the ion energyused.

3. Discussion of Results and Future Work

It seems evident from the experimental data that both ion flux and sample temperature play an important role in bubble nucleation. At the lower fluxes and temperatures, no bubble formation was observed. Possibly the critical dose required for bubble formation was not reached. Alternately, at low ion fluxes in thin samples, the surface may prevent the helium ion concentration from reaching a value necessary to produce visi-

ble bubbles. More experimentation with high ion doses with low ion fluxes will be required to determine if bubble nucleation eventually occurs at fluxes of 10^{13} ions/cm^{2}sec or less.

When bubbles were formed at higher fluxes, the ion flux and sample temperature influenced the nucleation and growth of larger bubbles at the grain boundaries. Grain boundary-helium bubble interactions have been investigated in copper by Beere[3], who proposes that as a moving grain boundary encounters bubbles, the bubble radius increases due to a decrease in the bubble surface energy. In our experiments no obvious boundary movements have been observed during the in-situ irradiations. The lack of enhanced bubble size at the grain boundaries in the cooler sample irradiated with ion fluxes in the low 10^{14} ions/cm^{2}sec. range is consistent with a lower helium mobility. This temperature dependence of oversized bubble decoration of grain boundaries is consistent with other observations in the literature.

Further investigation is required to separate sample temperature and ion flux related phenomenon. Special attention should be placed on grain boundary motion and the involvement of dislocations in the bubble nucleation and growth.

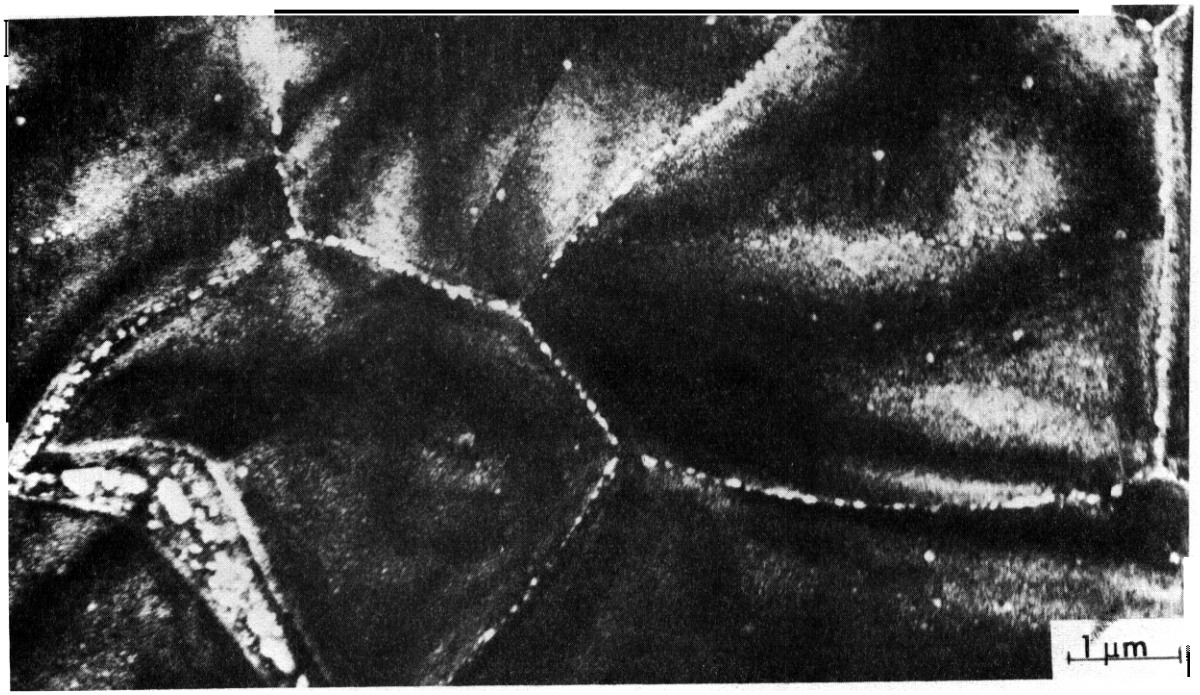

Figure 1: Transmission electron micrograph showing grain boundary bubble enlargement in a 316 SS sample irradiated with 80 keV helium ions with an ion flux of 1.5×10^{15} ions/cm^{2}sec and a sample temperature of 650° C to a total ion dose of 7×10^{17} ions/cm^2.

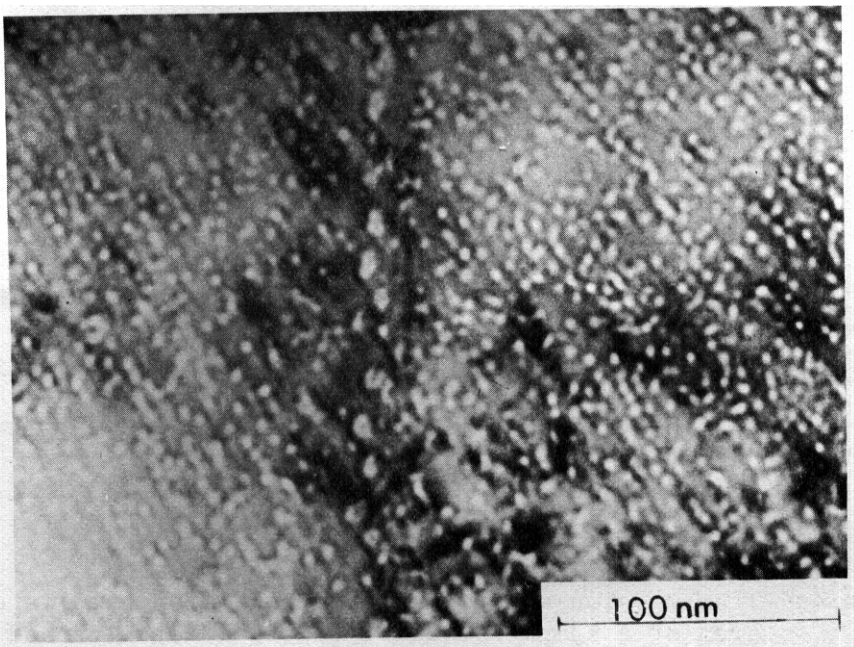

Figure 2: Same as figure 1, except for an ion flux of 6×10^{14} ions/cm^{2}sec and a fluence of 3×10^{17} ions/cm^2.

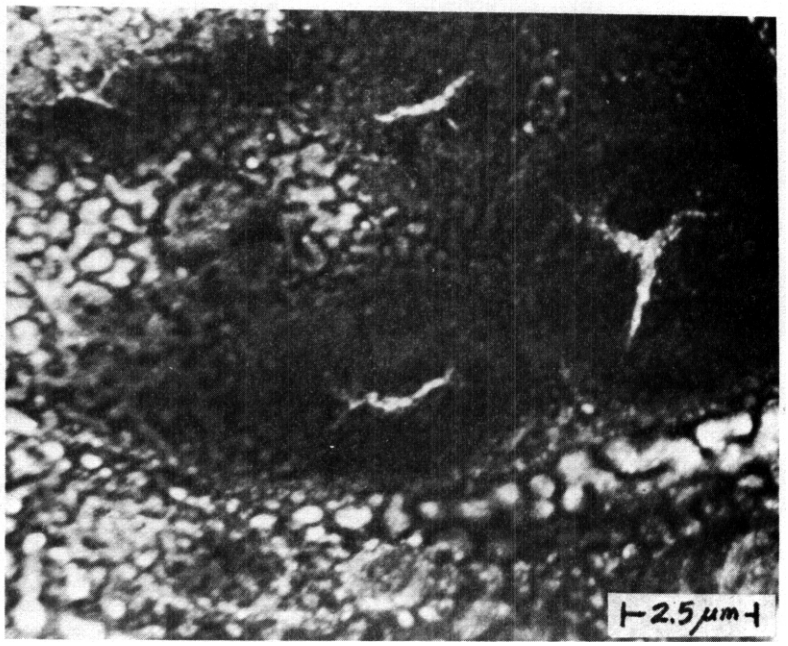

Figure 3: *400* kV **transmission electron micrograph** of **blisters on a 316 SS sample irradiated at a high temperature and a high flux.**

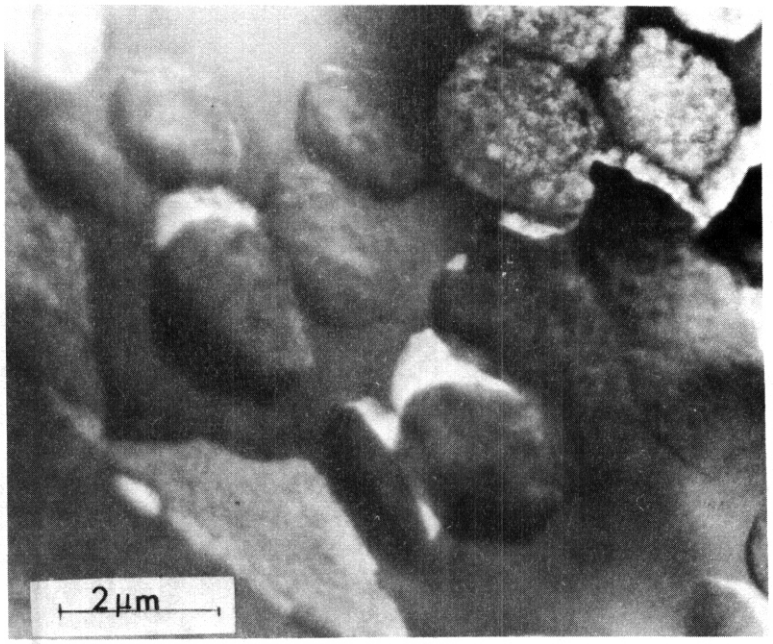

Figure *4:* **Transmission electron micrograph of an exfoliated area of a sample irradiated at a lower flux and temperature than the sample** shown **in figure 3.**

VI. REFERENCES

1. J. I. Bennetch, J. A. Horton, W. A. Jesser, "In-situ HVEM tensile tests of irradiated and unirradiated stainless steel", Quarterly Technical Progress Report DAFS, January-March 1978, DOE/ET-0065/1, August 1978.

2. J. I. Bennetch, J. A. Horton, W. A. Jesser, D. Kuhlmann-Wilsdorf, R. A. Johnson, and H. G. F. Wilsdorf, "In-situ HVEM tensile tests of irradiated and unirradiated stainless steel", Quarterly Technical Progress Report DAFS, April-June 1978, in press.

3. W. Beere, "An In-situ observation of the grain boundary/bubble interaction", Scripta Metallurgica, 9, (1975), pp. 999 - 1001.

VII. FUTURE WORK

See Section V, part 3 - Discussion of Results and Future Work.

I. PROGRAM

Title: Mechanical Properties
Principal Investigator: R. H. Jones
Affiliation: Battelle-Pacific Northwest Laboratory

II. OBJECTIVE

The displacement damage produced in Materials Research Corporation Marz grade nickel and niobium and reactor grade 316 SS by 16 MeV protons and (D,T) and (D,Be) neutrons is being correlated on the basis of cluster size and density and yield strength. The effects of steady state and cyclic flux, temperature and stress on the microstructure and flow stress are being studied. The relationship between the radiation induced microstructure and flow properties is also being studied. Irradiation damage studies of path B and C alloys are planned.

III. RELEVANT DAFS PROGRAM PLAN TASK/SUBTASK

SUBTASK II.C.5 Effects of Cycling on Microstructure
SUBTASK II.C.11 Effects of Cascades and Flux on Flow
SUBTASK II.C.12 Effects of Cycling on Flow and Fracture

IV. SUMMARY

The yield strength increase of T(d,n) and Be(d,n) neutron irradiated nickel and niobium have been compared over the fluence range of 5×10^{16} cm^{-2} to 10^{18} cm^{-2}. Irradiations were performed on material from the same source, given identical heat treatments and prepared and evaluated by the same techniques.

The nickel was less spectral sensitive than niobium as shown by the ratio of the number of Be(d,n) to T(d,n) neutrons at equal yield strength increase. For nickel this ratio was 1 while for niobium it was 5.

V. ACCOMPLISHMENTS AND STATUS

1) T(d,n) and Be(d,n) NEUTRON IRRADIATIONS

The yield strength increase of Be(d,n) and T(d,n) neutron irradiated nickel and niobium have been measured and the results are shown in Figs. 1 and 2. Comparison of the yield strength versus particle fluence curves for T(d,n) and Be(d,n) neutron irradiated nickel in Fig. 1 shows that the slopes are similar while an equal number of Be(d,n) as T(d,n) neutrons were needed to induce an equal yield strength increase. A similar comparison for niobium in Fig. 2 shows that the slopes are again approximately equal while five (5) times as many Be(d,n) as T(d,n) neutrons were needed to induce an equal yield strength increase.

The cause of the different spectral sensitivities of nickel and niobium to T(d,n) and Be(d,n) neutrons is not clear; however, Mitchell of LLL observed a similar but smaller difference between copper and niobium. This comparison should be made on a damage energy per atom or displacements per atom basis. To accomplish this, the Be(d,n) neutron energy spectrum must be established and the damage energy or displacement cross sections for each material must be known over the energy spectrum. The neutron spectrum for the Be(d,n) neutrons obtained at U.C. Davis with 40 MeV D^+ is being determined by L. Greenwood and R. R. Heinrich of ANL from multi-foil dosimeters attached to the PNL specimen packets.

Two more specimen packets have been irradiated with Be(d,n) neutrons to:

1) better define the yield strength increase and microstructure response.

2) improve the spatial data for neutron energy and flux.

The goal fluences for these packets were 6×10^{17} n/cm^2 and 1×10^{17} n/cm^2. Dosimeter foils were divided into a 3x4 matrix of 2 mm square foils. The results of these irradiations will be reported next quarter.

2) 16 MeV PROTON IRRAOIATIONS

The yield strength increase results for nickel and niobium irradiated with a 10^{13} p/cm^2-s flux (1.6μa/cm^2) of 16 MeV protons to a fluence of $5x10^{17}$ p/cm^2 at 30°C is also shown in Figs. 1 and 2. A helium flow of 7 scfm at 760 torr was used to maintain a specimen temperature *of* 30°C, while a static helium atmosphere of 760 torr was used to maintain a specimen temperature of 40°C at a proton flux of 10^{12} p/cm^2-s (.16μa/cm^2).

The yield strength increase of nickel irradiated with the high proton flux lies on a reasonable extrapolation of the lower flux data while the niobium data does not. An irradiation to $2\text{-}3x10^{18}$ p/cm^2 is scheduled to determine whether the niobium yield strength increase has saturated or whether the data point at $5x10^{17}$ p/cm^2 is in error.

3) 14 MeV NEUTRON-16 MeV PROTON CORRELATION

The correlation between the yield strength increase of 14 MeV neutron and 16 MeV proton irradiated nickel has been further substantiated by the Be(d,n) neutron data and the $5x10^{17}$ p/cm^2 data. Similarities were also observed in the flow behavior. Serrated yielding occurred in nickel irradiated to 3 and $10x10^{17}$ n/cm^2 with Be(d,n) neutrons and to $5x10^{17}$ p/cm^2 with 16 MeV protons. Since serrated yielding is associated with the density of defect clusters, the microstructures are also expected to be similar. Transmission electron microscopy on foils irradiated with the wire specimens is in progress.

VI. FUTURE WORK

Evaluation of the remaining nickel, 316 SS and niobium tensile and TEM specimens irradiated with Be(d,n) neutrons will be completed. Microscopy of nickel and niobium irradiated with 16 MeV protons to $5x10^{17}$ p/cm^2 is in progress while irradiations to 1 and $3x10^{18}$ p/cm^2 are scheduled. Scoping experiments to determine the maximum proton flux and temperature capabilities

of the 16 MeV proton irradiation apparatus are planned. The limits are estimated to be about 10^{14} p/cm^2-s and 500-700°C.

VII. PUBLICATIONS

A paper entitled "Experimental Radiation Damage Studies in 16 MeV Proton Irradiated Nickel and Niobium" by D. L. Styris and R. H. Jones will be presented at the Fifth Conference on Application of Small Accelerators, Nov. 6-8, 1978 at North Texas State University.

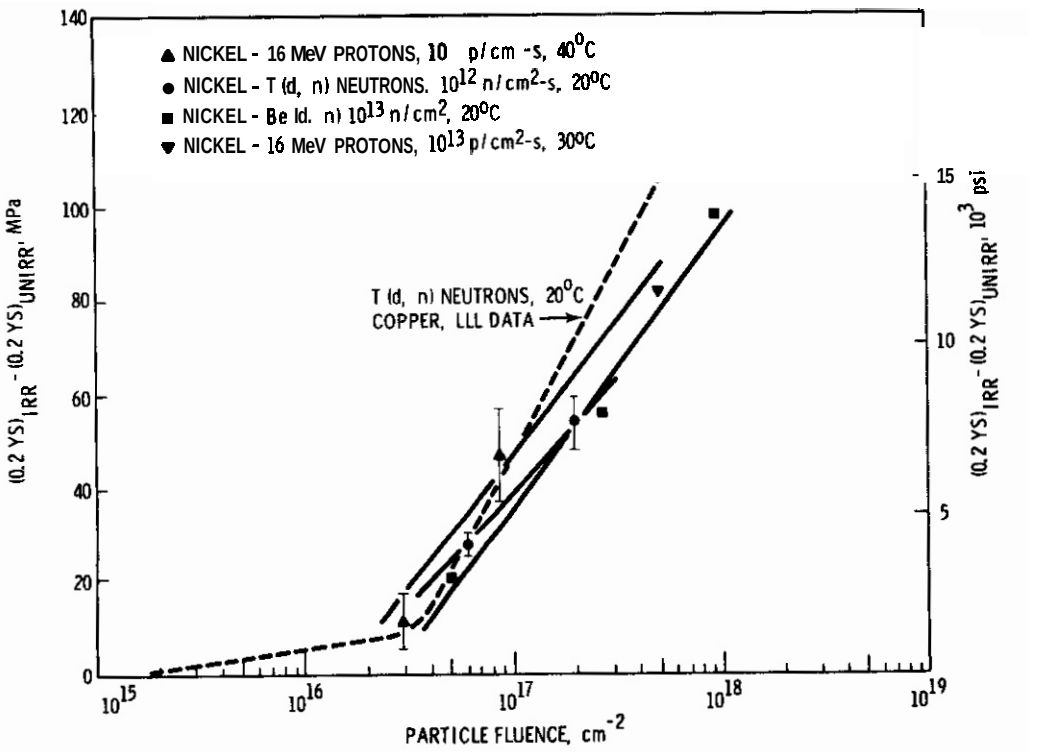

FIGURE 1. Yield Strength Increase Versus Particle Fluence for Neutron and Proton Irradiated Nickel.

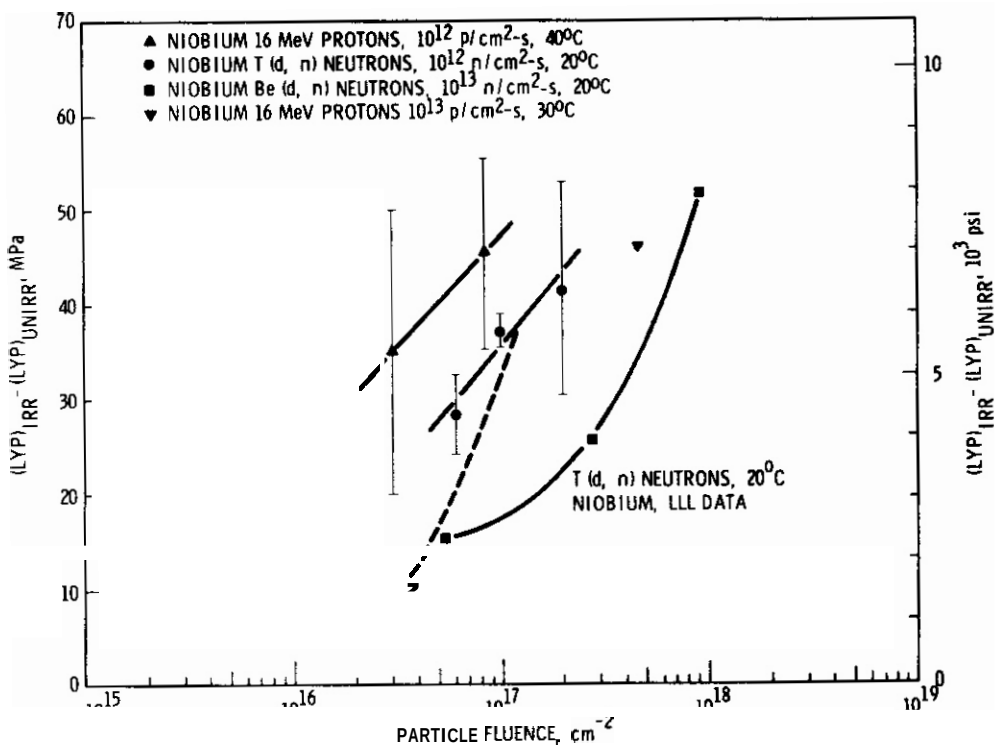

FIGURE 2. Yield Strength Increase Versus Particle Fluence for Neutron and Proton Irradiated Niobium.

I. PROGRAM

Title: Effects of Near Surface Damage and Helium on the Performance of the First Wall

Principal Investigator: O. K. Harling

Affiliation: Nuclear Reactor Laboratory, Massachusetts Institute of Technology

II. OBJECTIVE

The objective of this study is to understand and quantify the effects of near surface damage and implanted gas on the performance of the fusion reactor first wall.

111. RELEVANT DAFS PROGRAM TASK/SUBTASK

TASK	II.C.5	Effects of Cycling on Microstructure
	II.C.12	Effects of Cycling on Flow and Fracture
	II.C.13	Effects of Helium and Displacement on Crack Initiation and Propogation
	II.C.15	Effects of Near Surface Damage on Fatigue

IV. SUMMARY

Detailed design of an in-reactor fatigue cracking experiment has been complete&. Installation of the experiment is well under way and start of irradiations is scheduled for late in the 1978 CY.

V. ACCOMPLISHMENTS AND STATUS -- H. Andresen (M.I.T./Hahn Meitner Inst.) and O. Harling, A. Argon and K. Kwok (M.I.T.)

The aim of the in-reactor fatigue cracking experiment has been described in the last quarterly report. Detailed design of this experiment was completed and the safety report was essentially approved

by the Safeguards Committee of the MITR-II. A preliminary setup showed that the intended fast pressure cycling of the helium coolant does not cause vibrations of the irradiation thimble or other parts. Mechanical and electrical services for the fatigue experiment on the MIT reactor are well under way.

VI. REFERENCES

None

VII. FUTURE WORK

In-reactor testing and initiation of the fatigue cracking experiment is expected to begin in the next quarter.

I. PROGRAM

Title: Radiation Effects to Reactor Materials

Principal Investigator: G. L. Kulcinski and P. Wilkes

Affiliation: University of Wisconsin

II. OBJECTIVE

To develop a fundamental understanding of the formation of voids, loops and precipitates in heavy ion and electron irradiation metals and alloys.

III. RELEVANT DAFS PROGRAM TASK/SUBTASK

II.C.6. Effects of Damage Rate and Cascade Structure on Microstructure.

IV. SUMMARY

Specimens of high purity nickel were irradiated with high energy carbon and aluminum ions to study the effect on the void microstructure of using different bombarding species. The depth dependent damage structure was determined by preparing the foils such that they could be viewed directly in cross section. These results were then compared to previous irradiations performed on identical material using self-ions. The swelling behavior observed in the end-of-range region for all samples was similar, implying that impurities introduced by the ion beam do not strongly influence the swelling response of the material. The mass of the irradiating ions had no noticeable effect on the swelling values achieved for similar damage states, even though the recoil energy spectrum produced by the various ions were different. A dose scan using aluminum ions showed the void density to rise very rapidly and then drop with increasing dose above 2 dpa. Voids were also observed in all specimens at depths ~15% beyond the predicted end-of-range.

V. ACCOMPLISHMENTS AND STATUS

A. Effects of Bombarding Ions on the Void Swelling Profile in Nickel, J.B. Whitley, G.L. Kulcinski, H.V. Smith, Jr., and P. Wilkes, (University of Wisconsin, Madison, Wisconsin).

1. Introduction

The increased use of heavy-ion beams as a tool fur studying radiation induced void formation in metals has led to an interest in examining the depth dependence of the damage structure. The character of the heavy-ion damage mechanism changes considerably as the ion loses energy and by examining the depth dependence of the final damage state, one can gain an understanding of the radiation damage process. The various techniques that have been used to determine the depth dependent structure include successive thinning of transmission electron microscope (TEM) samples,[1] stereoviewing in a high-voltage electron microscope,[2-4] and preparation of TEM specimens for viewing directly in cross section.[5-9] Of these techniques, the latter is the most direct and powerful, but it is only easily applied to metals that can be electroplated with coatings of similar chemical composition.

The authors have previously used the cross sectioning technique to study the depth dependent microstructure of high purity nickel irradiated with 14 MeV and 14-19 MeV copper ions.[5,6,10] In these studies, voids were found at depths ≈20% beyond the maximum ion range predicted by various stopping theories,[11,12] and the void swelling profile was not simply related to the total damage profile. No major differences in microstructure were observed between the nickel and copper ion irradiated samples.

This paper presents the depth dependent microstructure development in high purity nickel irradiated at 525°C with carbon ions or with aluminum ions. These results will be compared with previous results obtained

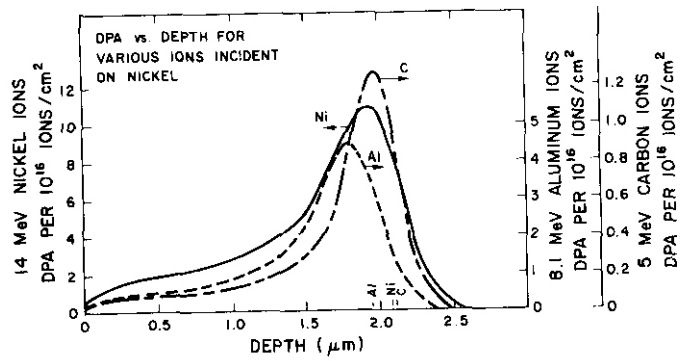

FIGURE 1. The calculated displacement curves for carbon, aluminum, and nickel ions incident on a nickel target. The stopping parameters were calculated using the Brice code.[11] (See footnote 1) Note the different scale values of each curve. Also shown near the base of the curves are the mean ion ranges given by the code.

3. Results

a. Aluminum Ion Irradiations

Nickel samples were irradiated at 525°C (798°K) with 8.1 MeV aluminum ions with fluences ranging from 4×10^{15} ions/cm^2 to 2.1×10^{16} ions/cm^2. The ions flux used was typically 8×10^{11} ions/cm^2 ($\approx 4 \times 10^{-4}$ dpa/s at the peak). The development of the depth dependent microstructure is shown in the micrographs of Figure 2. The left-hand-side of each micrograph shows the original foil surface. The incident ions have traveled from left to right and came to rest in the area near the right-hand-side of each micrograph. Voids nucleated quite readily in this material and were observed at all damage levels. The voids were always observed in these samples up to depths of 2.75 μm, with a few voids observed at even greater depths. There was no deviation in the void microstructure in the implanted range region that could be attributed to point defect interaction

from self-ion irradiations. The comparative results of these irradiations will be analyzed in terms of the differences in the damage processes by ions of different masses and different chemical species. Specifically, comparisons will be made to other irradiation studies of nickel containing small additions of carbon or aluminum before irradiation.[13,14]

2. Experimental Procedure

Details of the irradiation facility and sample target chamber[15,16] and the post-irradiation specimen techniques[5,6] can be found elsewhere. In brief, the specimens consisted of 0.5 mm thick nickel foil with nominal purity >99.995%. The ions used for this study were produced by an ANIS[17] negative ion source and accelerated in a tandem Van De Graaff accelerator to produce 5 MeV C, 8.1 MeV Al, and 14 MeV Ni ions. The damage curves calculated by the Brice code[11][a] are shown for these three ions in Figure 1. The ion energies were chosen such that the ions would have similar ranges in the target. The gross damage effectiveness as measured in displacements per atom (dpa) however, is quite different for the three ions as can be seen by the different scales for the various ions. Note that within each specimen, there exists both a large variation in the final damage level and also a corresponding variation in the displacement rate at which this level was achieved. The specimens were annealed at 850°C for one hour in an inert gas atmosphere and electropolished prior to loading into the target chamber. The specimens were irradiated in an ultra-high vacuum, high temperature sample chamber with a nominal pressure of 1×10^{-8} torr (1.3×10^{-6} Pa). After irradiation the specimens were prepared in cross sections by electroplating a 1 to 1.5 mm thick nickel deposit onto both sides and then slicing in a plane normal to the original foil surface using a low speed diamond saw. Three millimeter discs were then removed and the samples polished in a conventional two jet electro-polishing unit and examined in a 120 kV electron microscope.

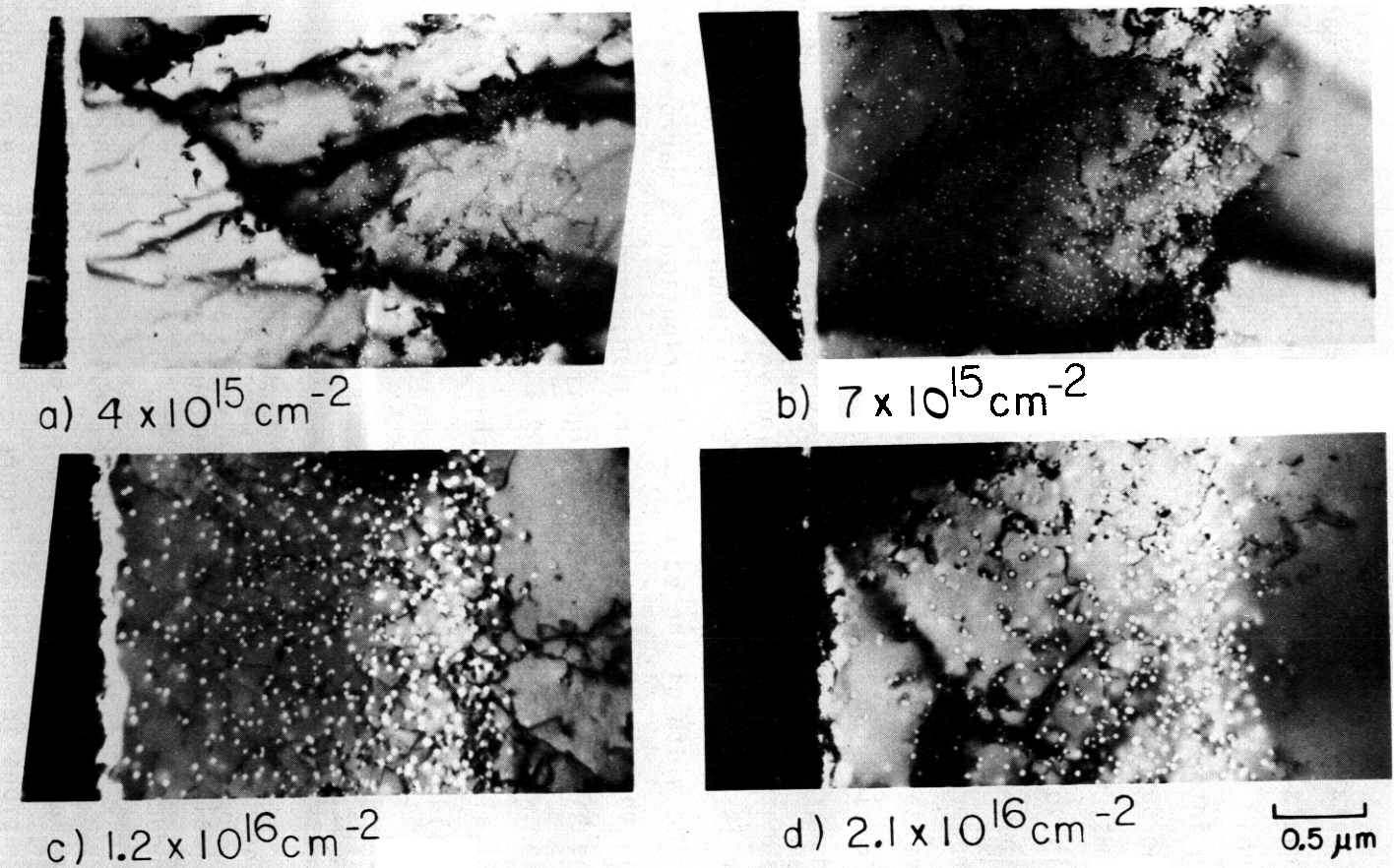

FIGURE 2. Nickel irradiated at 525°C (798°K) with 8.1 MeV aluminum ions to four fluence levels. The original foil surface is visible near the left-hand-side of each micrograph. The aluminum ions came to rest near the right-hand side

with aluminum ions. The voids were truncated octahedra throughout the damage region.

Void data was obtained from these specimens by dividing each into depth intervals 0.25 μm wide parallel to the foil surface. Average void diameter, void density, and void volume fraction were then measured within each interval. Figure 3 shows these data obtained for two fluence levels. The data points for each interval are plotted as points and not as histograms, with the curves drawn to aid the eye in following the depth variation in void parameters. At low fluences (Figure 3a) the void density curve has the same general shape as the displacement curve. At high fluences, however, the void density has dropped significantly and shows much less variation in magnitude from the front surface to the end-of-range than at low fluences. Except for the near surface region where larger voids are observed, the average void size throughout the damage region does not vary significantly. The void size distribution as a function of dose at two different depths is shown by the histograms of Figure 4. The width of the void size distribution is narrower in the mid-range region than in the end-of-range region, even though the average void sizes in the high dose case are not significantly different. The region of peak void swelling occurs at about 2.1 μm reaching a value of 3.3%. The theoretical peak damage level in this sample occurred at 1.8 μm reaching a value of C.5 dpa.

b. Carbon Ion Irradiations

The carbon ion irradiations were carried out on specimens prepared identically to those for the aluminum irradiation and the irradiation was conducted at 525°C (798°K). The carbon ion flux was 4×10^{12} ions/cm^2·s (5×10^{-4} dpa/s at the peak) and the ion fluences were 1.5×10^{16} ions/cm^2 and 9.3×10^{16} ions/cm^2. The void structures developed from these irradiations are shown in Figure 5, where again the original foil surface is shown on the left-hand-side of the micrographs. Voids were once more observed throughout the entire damage region, (even down to

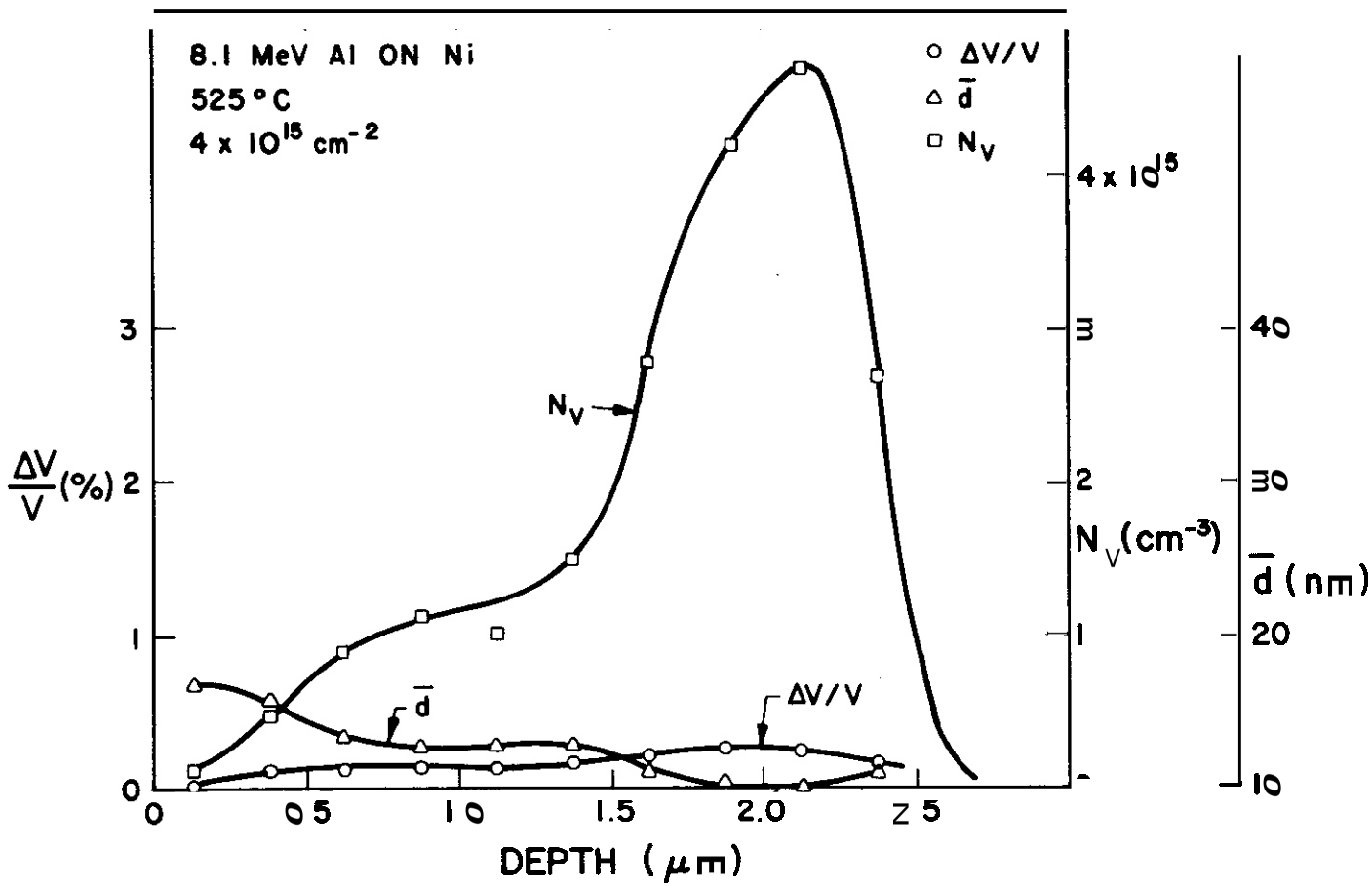

FIGURE 3a. Average void diameter $\bar{d}$, void density N_V, and void volume fraction $\Delta V/V$ measured as a function of depth in nickel irradiated with aluminum ions. al after a fluence of 4×10^{15} ions/cm^2 The curves serve only to guide the eye.

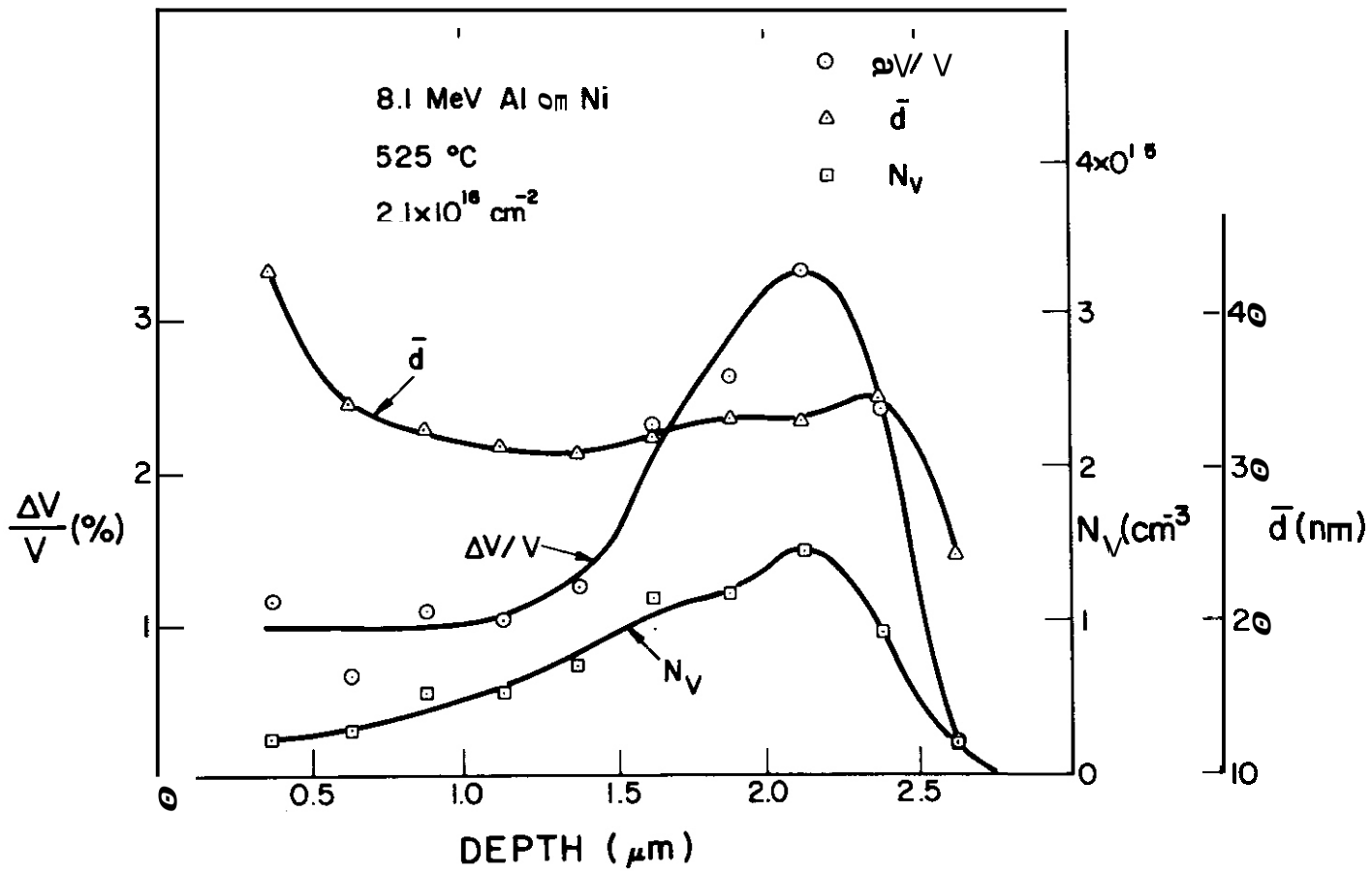

FIGURE 3b. Average void diameter $\bar{d}$. void density N_v, and void volume fraction $\Delta V/V$ measured as a fuction of depth in nickel irradiated with aluminum ions. b) after a fluence of 2.1×10^{16} ions/cm^2 The curves serve only to guide the eye.

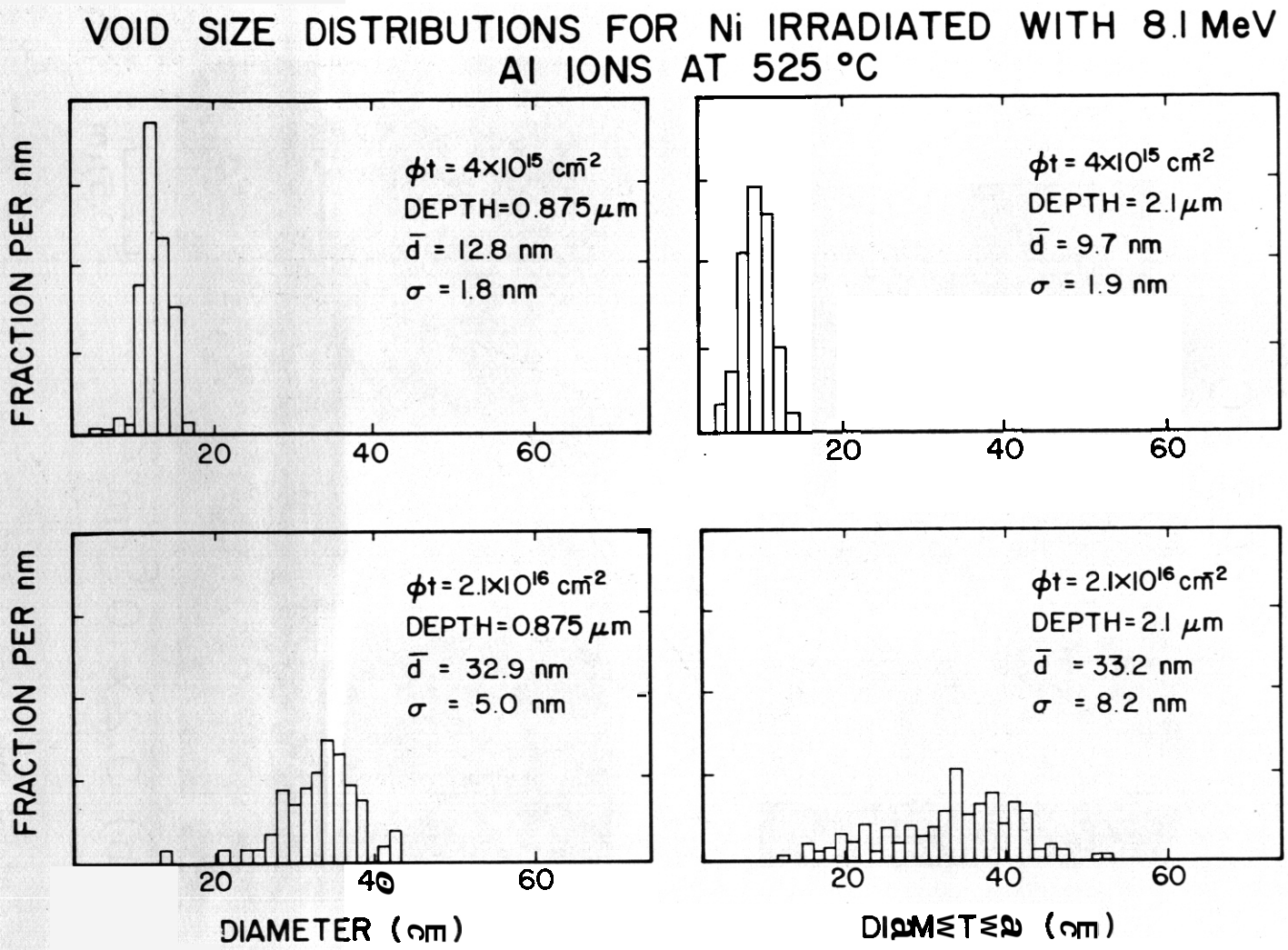

FIGURE 4. Void size distributions at two depths in nickel irradiated with aluminum ions to two fluence levels.

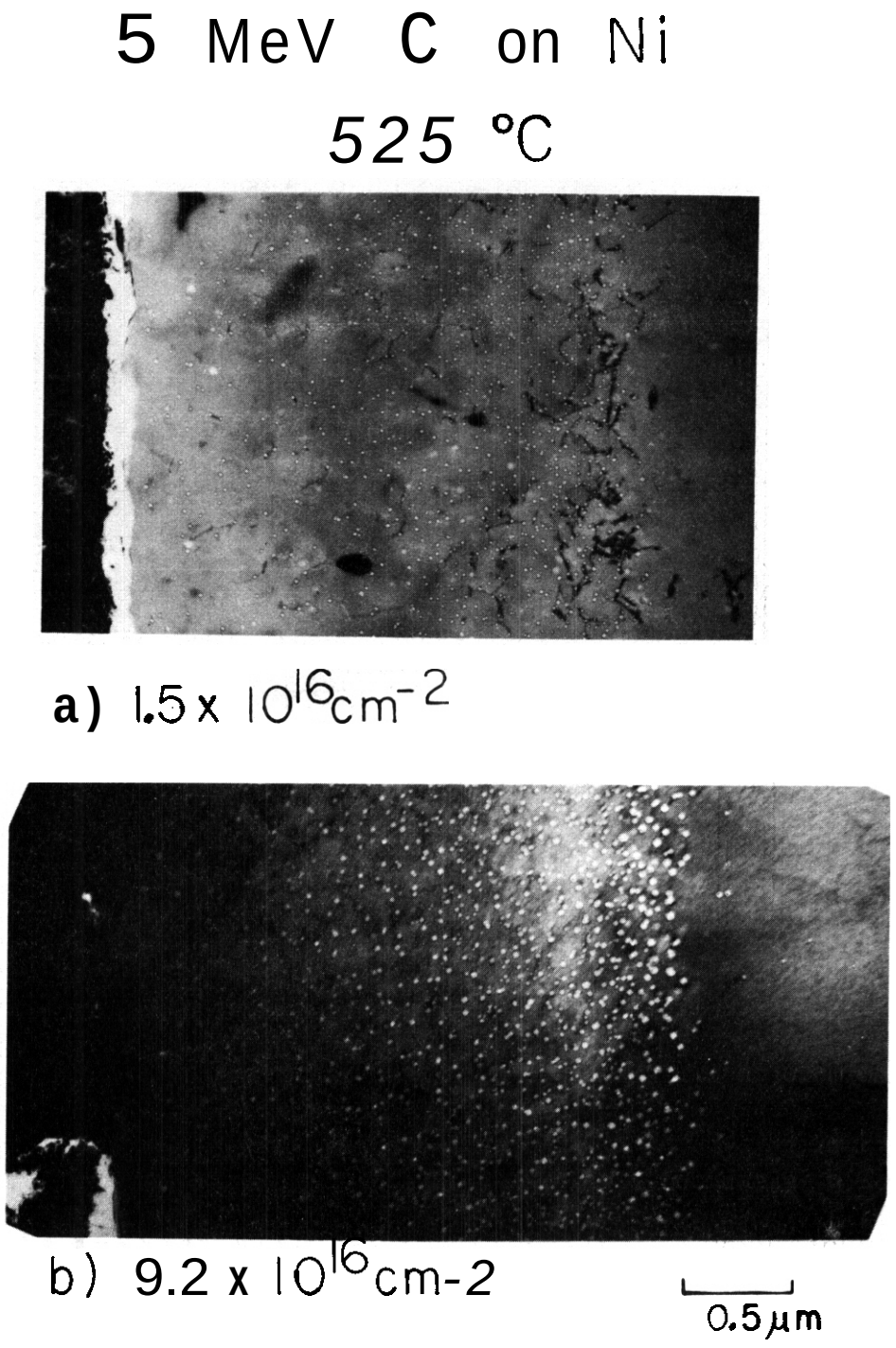

FIGURE 5. Nickel irradiated at **525°C** (798°K) with 5 MeV carbon ions to two fluence levels.

0.2 dpa) indicating the ease with which voids could nucleate in these samples. Most voids were observed in these samples at depths less than 2.85 μm, with a few voids seen at depths up to 3.2 μm. There is a slight increase in the void size at the end-of-range. Void shapes were again truncated octahedra.

The plots of void density, void size and void volume fraction for the two carbon ion fluences are shown in Figure 6. The void density curve is noticeably broader than the displacement curve in this case. The void density does not drop as rapidly with dose as in the aluminum ion irradiation, nor does the void size vary strongly with depth except for the surface region and the end-of-range region where it is larger than average. The peak void swelling in the carbon irradiated samples occurred at 2.4 μm with a value of 2.6%. The theoretical damage peak of 12 dpa occurs at a depth of 2.0 μm.

c. Dislocation Structure Development

The dislocation structure observed after irradiation with carbon ions is shown in Figure 7a. The structure consists mainly of network dislocations with a few scattered loops. The total dislocation density ranged from 10^{10} to 10^{11} cm/cm^3, and increased significantly in the end-of-range region.

The dislocation structure for the aluminum irradiated samples is shown for two fluence levels in Figures 7b and 7c. Here, at the low fluence, the dislocation structure consists of a dense network of dislocations interwoven among the high density of voids. This structure contains very few loops and is confined to the end-of-range region. At the highest fluence, the dislocation density has been reduced somewhat while at the same time extending to the near surface region.

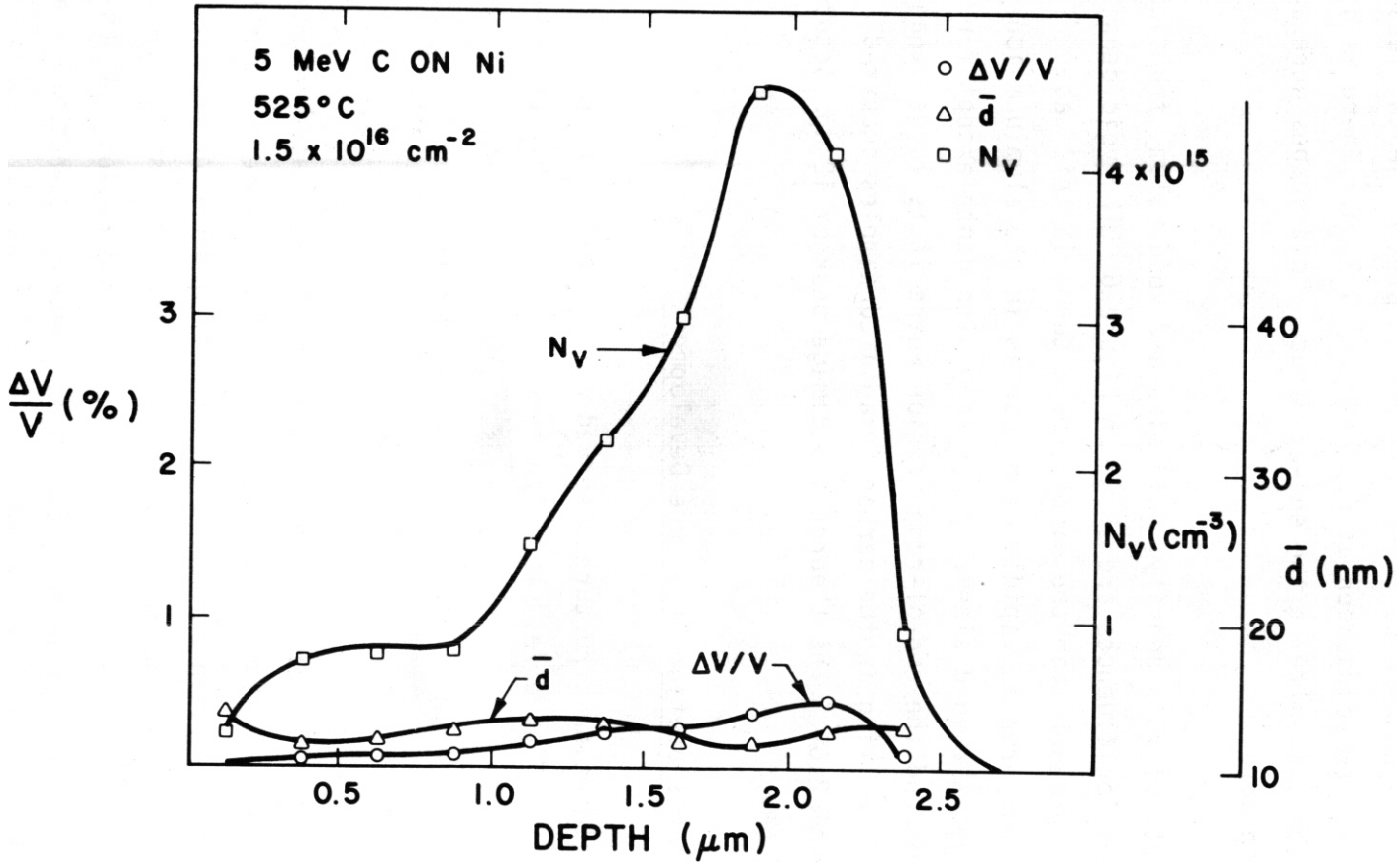

Figure 6a. Average void diameter, void density, and void volume fraction as a function of depth in nickel irradiated with carbon ions to 1 5 x 10^{16} cm^{-2}.

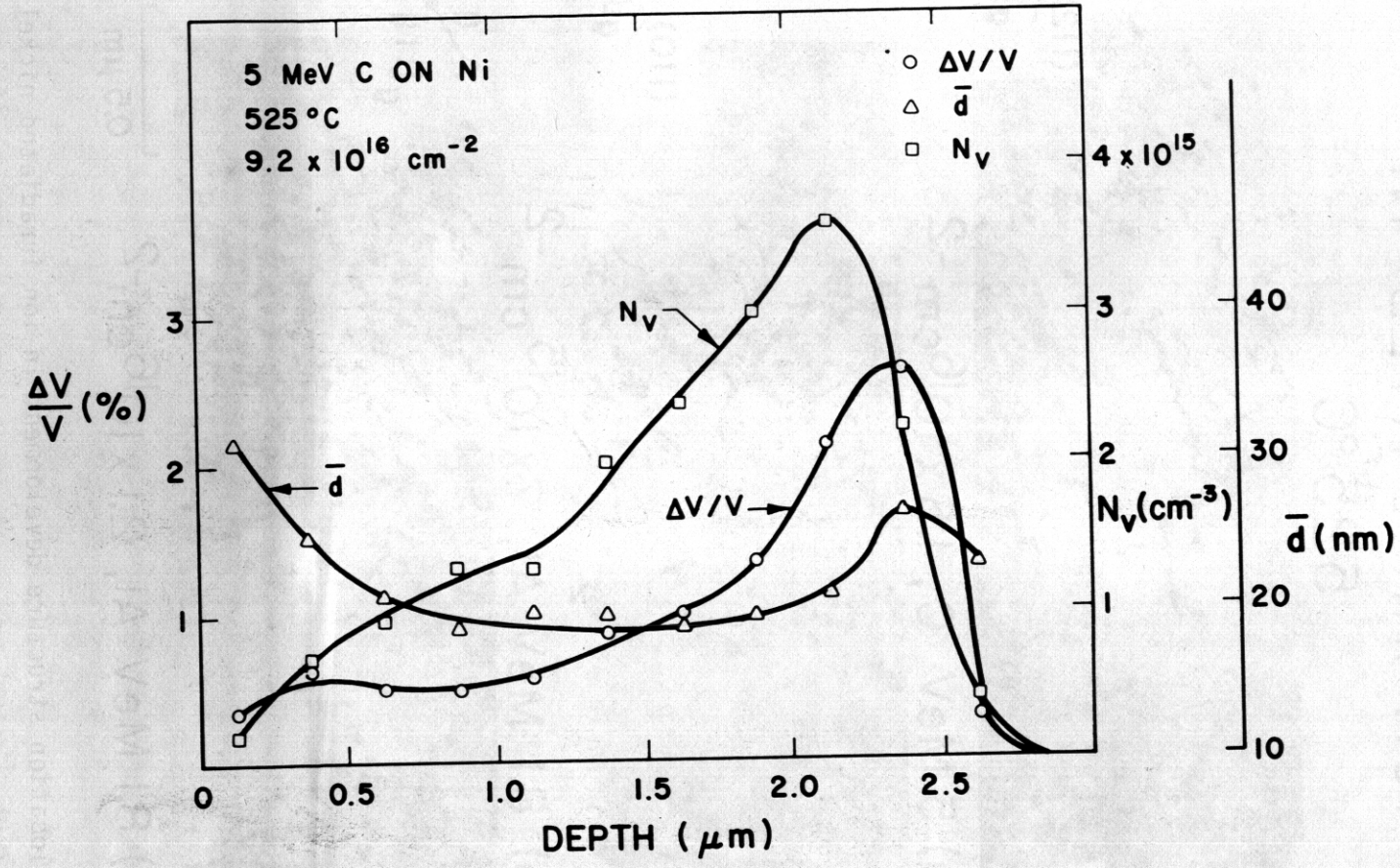

Figure 6b. Average void diameter, void density, and void volume fraction as a function of depth in nickel irradiated with carbon ions to $9.2 \times 10^{16}\ cm^{-2}$.

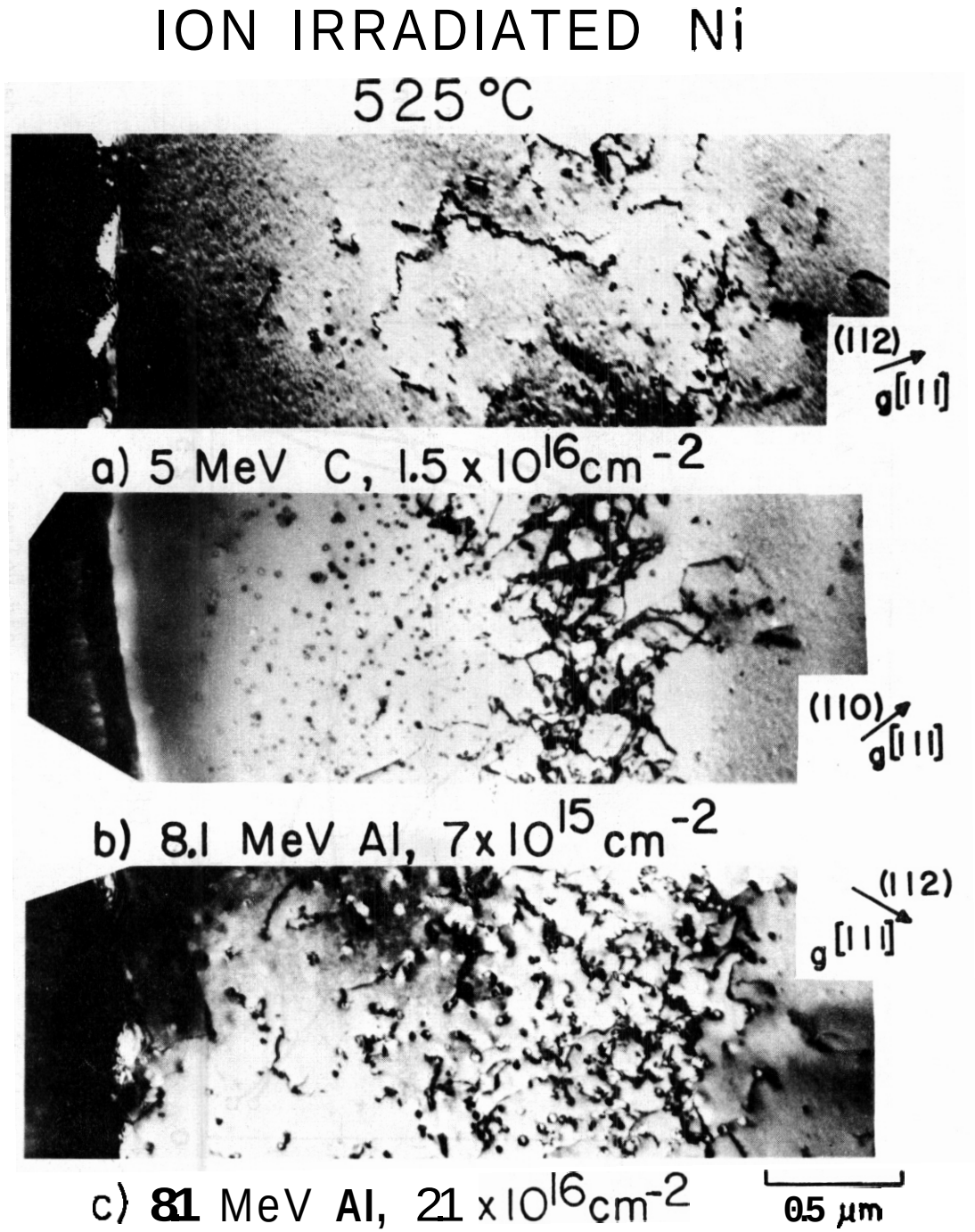

FIGURE 7. Dislocation structure development in ion irradiated nickel
a) after irradiation with carbon ions to a fluence of 1.5 x 10^{16} ions/cm2;
b) after irradiation with aluminum ions to a fluence of 7 x 10^{15} ions/cm2;
c) after irradiation with aluminum ions to a fluence of 21 x 1016 ions/cm2.

d. Comparison to Self-Ion Irradiations of Identical Specimens

The carbon and aluminum irradiations were designed such that a relatively c [illegible] d be made with a self-ion irradiated specimen.] [illegible] parison is shown where the ion fluences are such that the peak damage values vary from ~15 dpa for the nickel ion irradiated specimen to ~10 dpa for the aluminum ion irradiated specimen. The void data obtained from the self-ion irradiated specimen is shown in Figure 9. The nickel ion sample was irradiated at a higher dose rate, however, with a nickel ion flux of 1.5×10^{12} ions/cm^2·s (1.6×10^{-3} dpa/s at the peak compared to 5×10^{-4} dpa/s for the carbon and aluminum irradiated specimens).

There were several differences in the void microstructure between these specimens. In the near surface region, the self-ion irradiated specimen had a much larger void size in the surface region than either the aluminum or carbon irradiated specimens. This increase in void diameter is similar to the increase seen next to grain boundaries in these specimens. The self-ion irradiated specimen showed a reduction in the void size in the end-of-range region which was not seen with the other ions. This reduction corresponds to the peak in the void density curve. After aluminum irradiation, there is little variation in the void density and this reduction in void size is not seen. The carbon ion irradiated sample fails to show a drop in void size with increasing void density, but does show an increase at the far end-of-range region.

All specimens contained voids at depths greater than the range of the damage curve. This is shown in Figure 8, where the arrows on the micrographs indicate the predicted maximum ion range. The nickel ion irradiated sample showed a rather sharp void density cutoff with very few voids found beyond this range. Both the carbon and the aluminum irradiated samples failed to show this sharp cutoff, with a few scattered voids as much as 200-300 nm beyond the general void containing area.

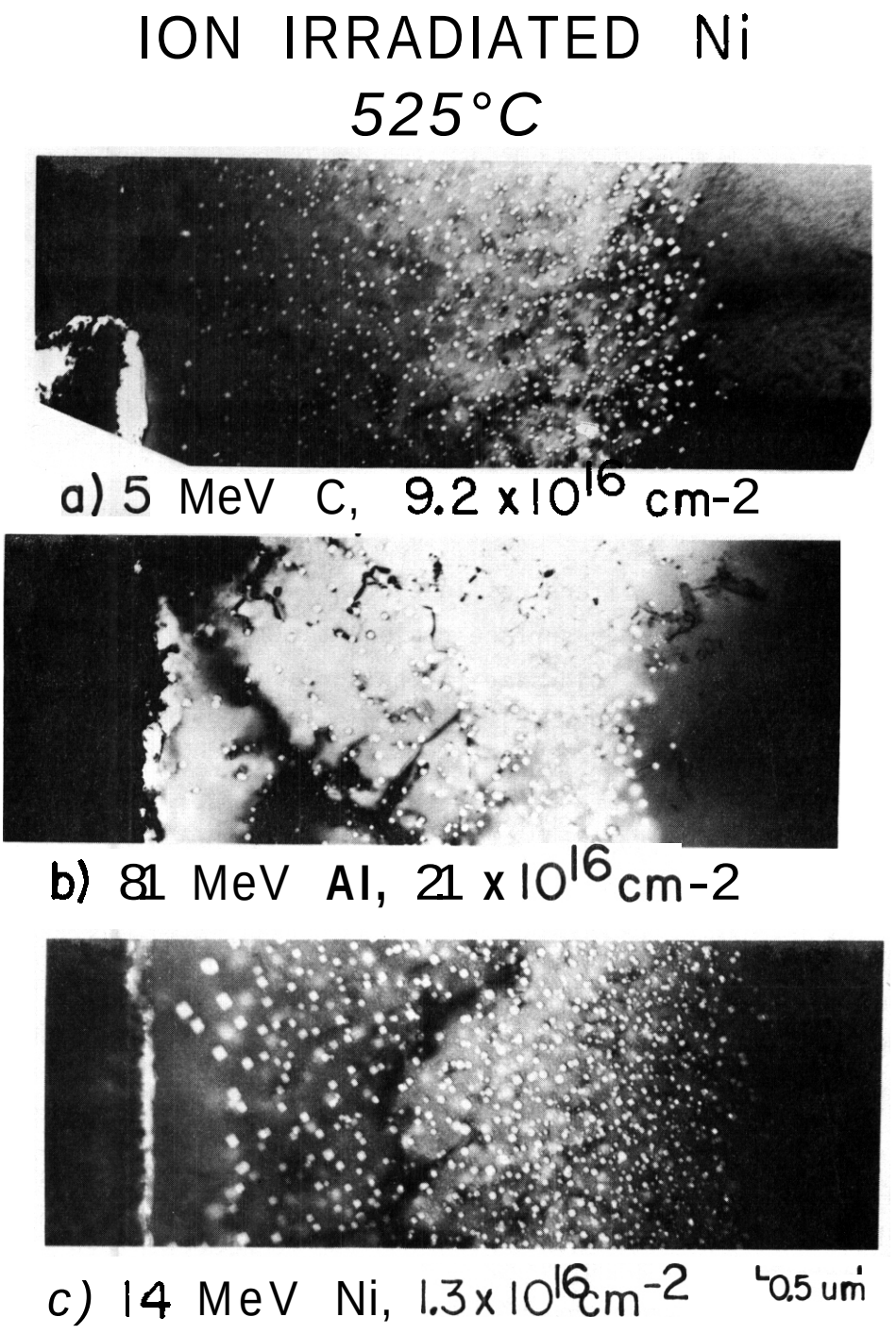

FIGURE 8. A comparison of nickel specimens irradiated at 525°C (798°K) with three different ions to fluence levels giving similar peak damage levels. The arrows near the right-hand-side of each micrograph indicate the predicted maximum ion range for the appropriate incident ion.

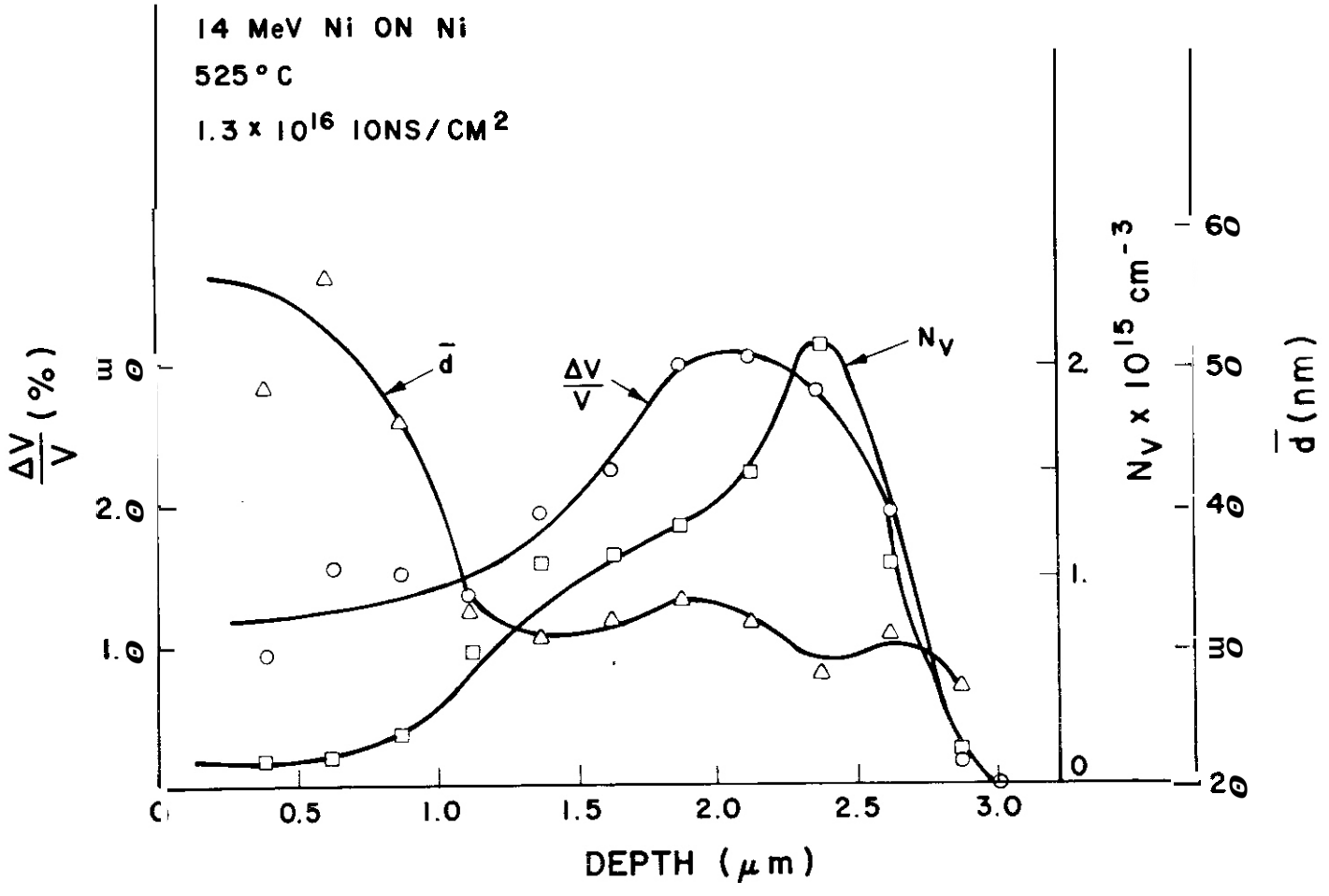

FIGURE 9. Average void diameter, void density, and void volume fraction as a function of depth in nickel irradiated with 14 MeV nickel ions at 525°C (798°K) to a fluence level of 1.3×10^{16} ions/cm^2.

4. Discussion

a. Effects Due to Disparate Incident Ions

There are two basic differences between irradiations with different ions that could be expected to affect the final damage state of the material. The first is the change in chemical composition by implantation while the second is the change in cascade structure. These will be discussed in turn.

i. Excess Interstitials and Impurity Effects

An important difference between irradiations performed with different ions is the end-of-range effects due to the incident ion coming to rest in the materials. In both the aluminum and nickel ion irradiated samples, the incident ion behaves like a lattice atom and hence will represent an extra interstitial produced in these regions. Under low swelling rate conditions, (i.e., when defect loss by recombination or to unbiased sinks dominates) this small fraction of excess interstitials could significantly reduce the void swelling rate in the end-of-range region.[18] This effect is not believed to be important for the high swelling rates observed in this study. In the case of aluminum or carbon irradiations, the incident ion represents an impurity which gradually increases in concentration as the irradiation proceeds, Since impurities often affect swelling behavior quite strongly, the end-of-range region of ion irradiated samples may be suspect. In this study, no major differences in void microstructure were observed in the end-of-range region of any of the specimens. The relatively small increase in void size at the end-of-range in the carbon sample may be due to an impurity effect such as a lowering of the surface energy.

Previous studies of nickel containing carbon[13] and nickel containing aluminum[14] before irradiation showed significant decreases in

swelling when compared to pure nickel specimens. The studies of carbon doped nickel of Sorenson and Chen[13] found that a carbon level of 0.3 atomic percent would completely suppress void formation. In the high dose sample of this study, carbon was injected to a level of at least ~0.4 atomic percent (even if the carbon distributes itself uniformly throughout the damage region). In the previous studies, the impurity was present in significant amounts at the start of the irradiation and hence could play a significant role in the void and loop nucleation process. When the impurity is being introduced by the irradiating beam, it is still at very low concentration levels early in the irradiation sequence and hence cannot significantly alter the nucleation process in materials that nucleate voids as rapidly as the material used in this study. If an irradiation were to be continued to much higher fluence levels, it is possible that the effects of implanted impurities on the void growth rate would become evident. The major observation of this study was that the time history of the irradiation-impurity level is important in determining what effects, if any, will be seen. This effect is important in considering such studies as simultaneous gas implantation with ion bombardment and in considering what effects transmutation reaction products might have on materials subject to neutron irradiation.

ii. Cascade Effects

The second effect examined in this study is the different displacement cascade structures produced by ions of different mass. Previous studies on irradiated stainless steel[19,20] have found protons to be over ten times more effective in producing swelling than an equivalent dpa irradiation using nickel ions. This difference was believed due to the lower mass of the proton. The differential scattering cross-sections for the three different ions at two different depths are shown in Figure 10. It can be seen that the primary knock-on (PKA) cross section, and hence the number of defects produced by a single incident ion, decreases with decreasing ion mass. With increasing depth, the cross-section for

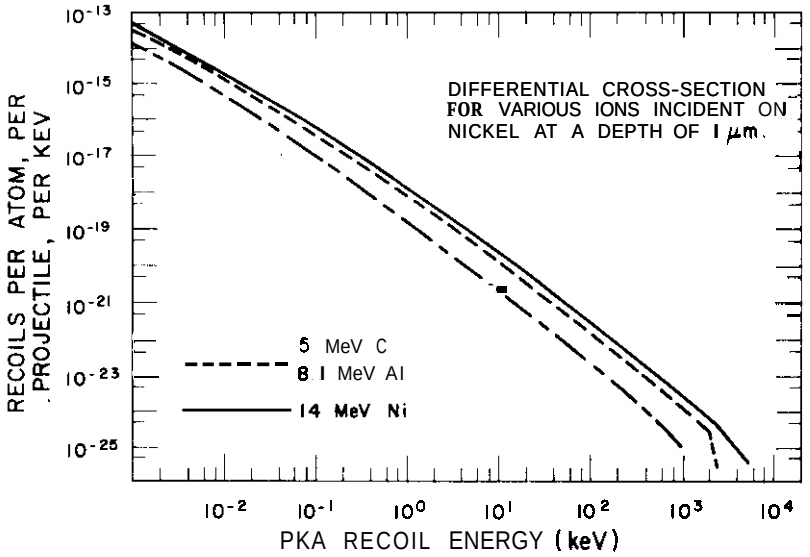

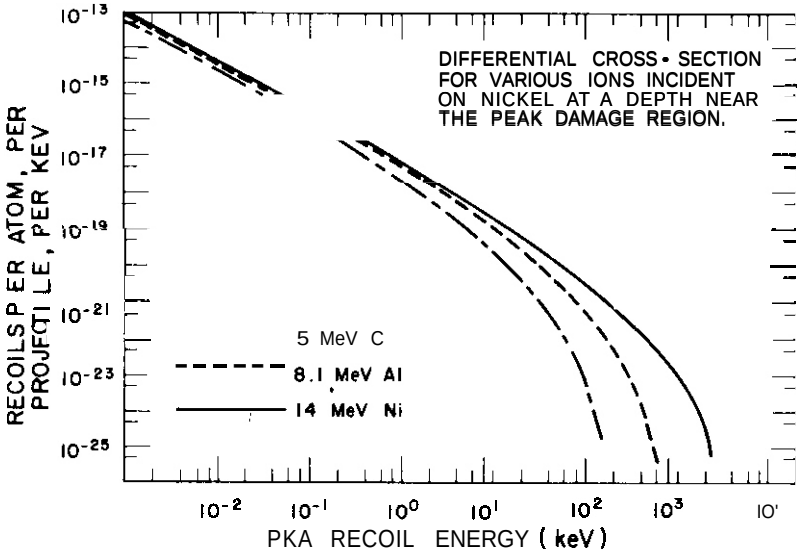

FIGURE 10. The primary recoil energy spectra for the three ions incident on nickel. The top curve corresponds *to* a depth of 1 μm, and the bottom curve a depth corresponding to the peak of the damage curve.

producing low energy PKA's will increase while the maximum energy that can be transferred is decreasing. One would expect the smaller displacement cascade of the light ions to allow less in-cascade recombination and hence release a larger fraction of the radiation produced defects to diffuse into the matrix. The results presented here, however, show that within a factor of two, there are no significant differences in the void microstructure that can be attributed to the different cascade structures.

b. Range Measurements

Both the carbon ion and aluminum ion irradiated specimens of this study contained a significant number of voids at depths ≈15% beyond the end-of-range given by the theoretical treatment of Brice.[11] In both cases, the peak of the swelling curve was also ~10% beyond the predicted peak of the damage curve. These results are consistent with previously reported results using nickel[5,6,8] and copper ions[6] incident on nickel, with the deviations from the predicted nickel and copper ion curves being somewhat larger. Narayan, et al.,[8] attribute this deviation in range to an underestimate of the electronic energy loss by the incident ion. This seems to be a reasonable explanation, even though such mechanisms as vacancy diffusion down the steep concentration gradient at the end-of-range could allow void growth in a damage free region.

c. Void Density

Under the aluminum ion irradiation, the void number density was observed to be a maximum at the lowest ion fluence, and then to drop with increasing fluence. Similar behavior has been observed previously in nickel[21,22] and is not believed to be due to void impingement, but rather due to local changes in the microstructure.[22] In the material prepared for this study, voids did nucleate quite easily. This apparently leads to such a high void density that continuing the irradiation beyond that necessary to nucleate the voids causes a subsequent change in the

microstructure which allows some of the voids to continue to grow, with the rest shrinking and disappearing. Possible causes for this behavior include a) an increase in the void critical size, b) the dislocations connecting the voids leading to enhanced void coarsening, and c) the lower vacancy concentration due to the increasing sink density.[23] The data from this study was not sufficient to determine which mechanism was valid.

5. 'Conclusions

The depth dependent void microstructure in nickel irradiated at 525°C with carbon and aluminum ions was measured and the following conclusions were drawn:

1. Any end-of-range effects due to the irradiating ions stopping in the material are minimal. This demonstrates the importance of the impurity-irradiation time history, with impurities present in significant amounts at the start of the irradiation being much more important than impurities added during the irradiation.

2. Voids were observed at depths ≈15% beyond the predicted damage curve, indicating that either the theoretical energy loss models are in error or that vacancies are transported over large distances from their point of origin.

3. The void density was a maximum at the lowest carbon and aluminum ion fluences, and dropped with increasing ion fluence. This indicates that the critical void size for growth is increasing with the growing void and dislocation microstructure.

4. The differences in the PKA spectra from carbon, aluminum, and nickel irradiations does not appear to have any major effect on the nucleation and growth of voids.

VI. REFERENCES

1. W. G. Johnston, J. H. Rosolowski, and A. M. Turkalo, Journal of Nuclear Materials 62, 1976, pp. 167-180.

2. C. W. Chen, A. Mastenbroek, J.O. Elen, Radiation Effects 16, 1972, pp. 127-132.

3. S. Diamond, I. M. Baron, M. L. Blieberg, R. Bajaj, and R. W. Chichering, Proceedings of International Conference on Radiation Effects and Tritium Technology for Fusion Reactors, Gatlinburg, Tenn., Oct. 1975, Vol. I, pp. 207-229.

4. A. F. Rowcliffe, S. Diamond, M. L. Blieberg, J. Spitznagel, and J. Choyke, Properties of Reactor Structural Alloys After Neutron or Particle Irradiation, ASTM STP 570, American Society for Testing and Materials, 1975, pp. 565-583.

5. J. B. Whitley, P. Wilkes, and G. L. Kulcinski, UWFDM-159, University of Wisconsin, Madison, Wisconsin, 1976.

6. J. B. Whitley, G. L. Kulcinski, P. Wilkes, and H. V. Smith, Jr., accepted Journal of Nuclear Materials, (1978).

7. R. A. Spurling and C. G. Rhodes, Journal of Nuclear Materials 44, 1972, pp. 341-344.

8. J. Narayan and O. S. Oen, Journal of Nuclear Materials 66, 1977, pp. 158-162.

9. J. Narayan and O. S. Oen, and T. S. Noggle, Journal of Nuclear Materials 71, 1977, pp. 160-170.

10. J. B. Whitley, P. Wilkes, G. L. Kulcinski, Transactions of the American Nuclear Society, Vo. 23, 1976, pp. 136-137.

11. D. K. Brice, SAND75-0622, Sandia Laboratories, Albuquerque, New Mexico, July 1977.

12. I. Manning and G. P. Mueller, Computer Physics Communication 7, 1974, pp. 85-94.

13. S. M. Sorenson, Jr., and C. W. Chen, Proceedings of International Conference on Fundamental Aspects of Radiation Damage in Metals, Gatlinburg, Tenn., Oct. 1975, CONF 751006, pp. 1213-1220.

14. F. A. Smidt, Jr., and J. A. Sprague, Naval Research Laboratory Memorandum Report 2998, 1975, pp. 39-51.

15. R. G. Lott and H. V. Smith, Jr., Symposium on Experimental Methods for Charged Particle Irradiation, Gatlinburg, Tenn., CONF 750947, Sept. 1976, pp. 82-98.

16. H. V. Smith, Jr., and R. G. Lott, Nuclear Instruments and Methods 143, 1977, pp. 125-132.

17. H. V. Smith, Jr., I.E.E.E. Transactions on Nuclear Science, NS-23, 1976, p. 1118, to be published.

18. A. O. Brailsford, and L. K. Mansur, Journal of Nuclear Materials 71, 1977, pp. 110-116.

19. G. L. Kulcinski, Applications of Ion Beams to Metals, Plenum Corporation, N.Y., 1974, pp. 613-637.

20. O. W. Keefer and A. G. Pard, Journal of Nuclear Materials 47, 1973, p. 97.

21. J. A. Sprague, J.E. Westmareland, F. A. Smidt. Jr.. and P. R. Malmberg, Consultant Symposium on The Physic; Of Irradiation Produced Voids, Harwell, Oxfordshire, U. K., 1974, pp. 263-267.

22. T. O. Ryan, Ph.D. Thesis, University of Michigan, 1975. (Available from University Microfilms, Ann Arbor, Michigan, U.S.A.)

23. N. Ghoniem and G. L. Kulcinski, Journal of Nuclear Materials 69,70, 1978, pp. 816-820.

FOOTNOTES:

a. The conversion to displacements assumed a displacement energy of 40 eV and used the recommended practice for neutron damage simulation by charged particle irradiation, E 521-76 (Prepared under ASTM Committee E-10, Subcommittee E 10.08, 1974).

VII. FUTURE WORK

The effect of dpa rate on the microstructure of heavy ion Ni will be described.

VIII. PUBLICATIONS

1. G. L. Kulcinski, "Progress in Materials Research for Fusion Reactors," IAEA Conf. on Reactor Design, Madison, 1977 to be published in Nuc. Fusion.

2. J. 8. Whitley, G. L. Kulcinski, P. Wilkes, and H. V. Smith, Jr., "The Depth Dependent Damage Profile in Nickel Irradiated with Nickel and Copper Ions," accepted to J. Nuc. Materials.

3. J. B. Whitley, G. L. Kulcinski, P. Wilkes, and H. V. Smith, Jr., "Effects of Bombarding Ions on the Void Swelling Profile in Nickel," 9th ASTM International Symposium on Effects of Radiation on Structural Materials," Richland, WA, 1978.

I. PROGRAM

Title: Irradiation Response of Materials
Principal Investigators: J. A. Spitznagel and W. J. Choyke
Affiliation: Westinghouse Research and Development Center

II OBJECTIVE

The objective of this work is to assess the phenomenology and mechanisms of microstructural evolution in materials exposed to simultaneous helium injection and creation of atomic displacement damage by a second ion beam.

III. RELEVANT DAFS PROGRAM TASK/SUBTASK

SUBTASK II.C.II.I Light Particle Irradiations

IV. SUMMARY

Tensile tests are being performed on Type 316 stainless steel foils several microns thick for comparison with tests on specimens of conventional size.

V. ACCOMPLISHMENTS AND STATUS

A. Miniaturized Tensile Specimens*

The mechanical behavior of miniature specimens is of interest in studies of radiation effects on mechanical properties. In the case of neutron irradiation, the large penetration range of neutrons has made it possible to evaluate bulk material using standard laboratory size test specimens. For light particle and ion irradiations, by contrast, the

* Funded by non-DOE sources.

range of penetration is very small -- microns, versus hundreds of centimeters for neutrons. This limited range of penetration by light particles and ions has led to emphasis on microstructural effects with little attention to direct mechanical property measurements. Current interest in fusion reactors and the present need to use ion irradiations to simulate the damage expected due to the hard neutron energy spectrum from fusion reactions gives renewed incentive to make mechanical property tests on ultrathin foils. A question which immediately arises is whether the properties of such thin foils are representative of bulk material. To answer this question, tensile tests were run on 316 stainless steel foils having a thickness of a few microns. Data are currently being analyzed.

VI. REFERENCES

None.

VII. FUTURE WORK

The results of the scaling studies will be reported next quarter. This work will be used to design mechanical property specimens suitable for use in the High Energy Ion Bombardment Simulation (HEIBS) Facility at the University of Pittsburgh.

VIII. PUBLICATIONS

None.

I. PROGRAM

Title: Effects of Irradiation on Fusion Reactor Materials
Principal Investigator: F. V. Nolfi, Jr.
Affiliation: Argonne National Laboratory

11. OBJECTIVE

The objective of this work is to establish a correlation between the net point defect production rates obtained during light-ion and neutron irradiations that have the same calculated damage rates deduced from the exposure parameters.

III. RELEVANT DAFS PROGRAM PLAN TASK/SUBTASK

SUBTASK II.C.ll.l Light Particle Irradiations

IV. SUMMARY

Installation and repairs of the torsional-creep apparatus at the ANL Cyclotron are complete. The performance of the apparatus has been checked-out by performing thermal creep measurements. Damage correlation experiments are being planned.

V. ACCOMPLISHMENTS AND STATUS

A. Damage Correlation -- V. K. Sethi and A. P. L. Turner

The torsional-creep apparatus has been transferred from Hanford Engineering Development Laboratory to Argonne National Laboratory. Repairs of irradiation damaged and malfunctioning electronic equipment are completed. The apparatus is now installed at the ANL Cyclotron and in working condition.

In the creep apparatus a wire specimen is stressed in the torsional mode by an electromagnetic (galvanometer) loading technique. Rotation or strain is measured by an optically coupled photocell tracking system. Temperature control of the specimen is obtained by resistance heating and varying the temperature of flowing helium passing perpendicularly across the specimen. Coupling between the control and measuring functions is through an infra-red pyrometer feed-back system. The apparatus is capable of strain resolution of better than 10^{-6}, with a $\pm 3^{\circ}C$ temperature stability with beam on/off conditions. A detailed description of the apparatus can be found elsewhere [1].

The apparatus will be used to establish a correlation between the damage produced in first-wall materials by light-ions and neutrons with energies similar to those in a fusion reactor (FR) spectrum. Type 316 stainless steel (HT No. 15893) has been obtained from the MFE stockpile and is being processed into 0.076 cm diameter wire. The specimens will be fabricated from the wire by electropolishing a reduced section (-0.013 cm dia. & -0.64 cm long).

The apparatus has been checked-out for temperature control, sensitivity to vibrations, stability and electronic noise by performing thermal-creep measurements. Figure 1 shows the temperature dependence of the minimum creep-rate for 20% cw type 316 stainless steel (HT No. V87210) for a maximum shear stress of 140 MPa (20 ksi) at the minimum diameter. In addition, with the assistance of Eric Opperman of Hanford Engineering Development Laboratory, a preliminary proton irradiation creep experiment was conducted on a stainless steel specimen at $400^{\circ}C$ stressed to a maximum shear stress of 140 MPa (20 ksi) at the minimum diameter. The specimen was irradiated to a total dose of -0.007 dpa and a total strain of $\sim 2 \times 10^{-5}$ was observed during a 6 hour period. The average creep-rate from this short-time irradiation is also illustrated in Fig. 1 (open symbol).

VI. REFERENCES

1. E. K. Opperman, J. L. Straalsund, G. L. Wire and R. H. Howell, "Proton Simulation of Irradiation Induced Creep", **accepted** by Nuclear Technology for publication.

VII. FUTURE WORK

The rate of climb controlled plastic deformation is proportional *to* the rate at which excess vacancies or interstitials arrive at dislocations and, thus, can he used for establishing a link between the damage produced in first-wall mterials by various bombarding spieces. Torsional creep-rate measurements will be made on wire specimens of type 316 stainless steel (HT No. 15893) during low temperature irradiations with light-ions at the *ANL* Cyclotron. The effects of stress and charged-particle flux will be investigated. Analyses of the experimental data using various models of radiation-enhanced creep will he used to establish a basis for determining the effective net defect production rates.

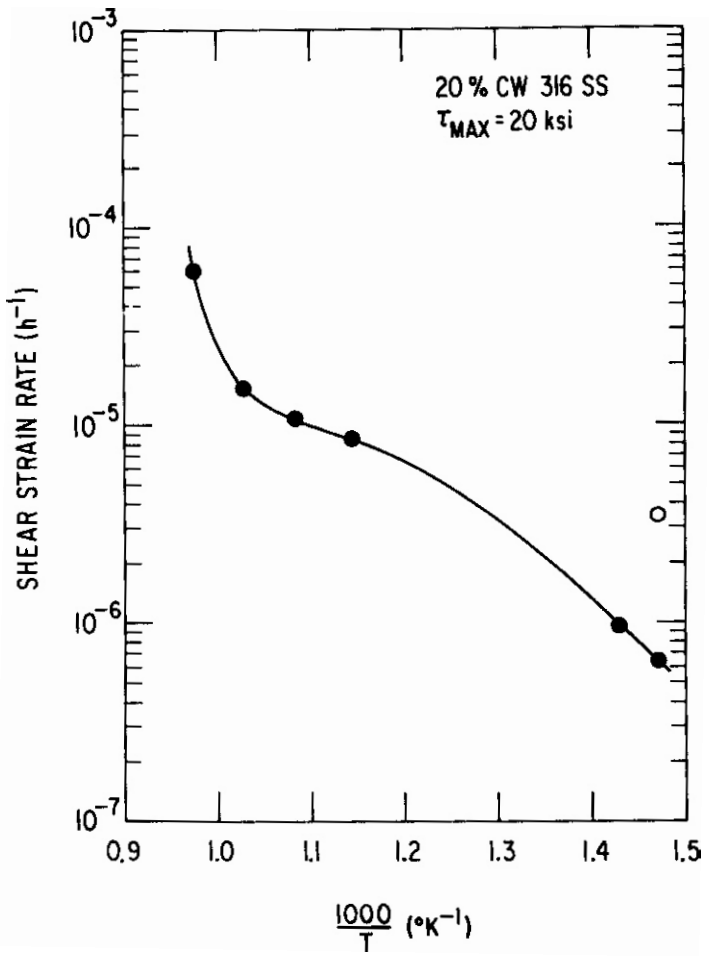

FIGURE 1. Thermal and 11 MeV-proton irradiation creep rates for 20% CW Type 316 stainless steel. Irradiation creep at 400°C.

I. PROGRAM

Title: Irradiation Response of Materials

Principal Investigators: J. A. Spitznagel, W. J. Choyke

Affiliation: Westinghouse Research and Development Center

II. OBJECTIVE

The objective of this work is to assess the phenomenology and mechanisms of microstructural evolution in materials exposed to simultaneous helium injection and creation of atomic displacement damage by a second ion beam.

III. RELEVANT DAFS PROGRAM PLAN TASK/SUBTASK

SUBTASK II.C.18.1 Nucleation Experiments

IV. SUMMARY

Targets of 316 SS from the MFE heat in both solution treated and 20% cold-rolled conditions were bombarded with 28 MeV Si^{+6} ions and 2 MeV helium ions to study the effects of helium injection mode and cold work on cavity formation. Varying the mode of helium injection (pre-implanting at elevated temperature vs simultaneously implanting the helium) was shown to have a large influence on the nucleation and growth of cavities, dislocation loops and carbide precipitation. Work continued on the installation of the ultrahigh resolution residual gas analyzer for studies of the effect of the vacuum ambient on microstructural evolution during irradiation of the reactivelrefractory metals.

V. ACCOMPLISHMENTS AND STATUS

A. The Effects of Hot Pre-Implantation and Simultaneous Helium Injection on Microstructural Evolution in 316 SS

The problems of designing mixed spectrum reactor experiments requiring spectral tailoring to achieve constant appm helium/dpa ratios and pre-implanting helium into materials which will not experience sufficient helium generation by transmutation reactions are substantial. Charged particle irradiation experiments will hopefully be able to provide some insight into the effects of helium implantation technique on microstructural evolution and on the need for spectral tailoring.

At present, two ion accelerators are being used to either sequentially or simultaneously implant helium ions and produce atomic displacement damage with 28 MeV Si^{+6} ions in 316 stainless steel from the MFE heat. Targets are currently 3 mm diameter discs prepared from solution annealed (1050°C - 1 h) or cold-worked material (1050°C - 1 h + 20% C.R.). In the sequentially bombarded targets, helium has been pre-implanted at temperatures in the range 550°C to 750°C. The helium was distributed over a depth of several microns in the target by "chopping" a beam of 2 MeV helium ions with Al degrader foils of varying thickness. The helium concentration profile was also "tailored" to closely match the damage energy profile from the 28 MeV silicon ions. This resulted in a damage region extending from a depth of ~0.5 μm to 3 μm in the target over whfch the helium/dpa ratio was nearly constant. Bombardment with silicon ions has been conducted at the same temperature as the helium pre-injection. Simultaneous bombardment of companion targets with helium and silicon ions has been performed at temperatures identical to those used for the sequentially bombarded targets. Samples were bombarded to peak damage levels of ~30-40 dpa at each temperature. Calculated atomic displacement rates varied from $\sim 6.4 \times 10^{-5}$ dpa.sec^{-1} at the surface to $\sim 1.2 \times 10^{-3}$ dpa.sec^{-1} at the peak damage region. The appm helium/dpa ratio was maintained constant throughout these experiments at a value of ~11. Following bombardment the targets

are being sectioned to various depths corresponding to different damage rates and fluences along the damage energy profile for the silicon ions. To avoid surface proximity and excess silicon effects, data are being taken from a 1.0 to 3.0 μm deep region.

TEM observations have revealed marked differences in microstructure depending on the helium implantation technique and ion bombardment temperature. In particular, precipitation of second phases, cavity formation and dislocation loop formation are all sensitive to the mode of helium injection at low fluences (∿2-10 dpa). In this report we will briefly summarize the current microstructural observations. Numerical analysis of cavity size distributions, precipitate volume fractions dislocation density, etc. is in progress and will be reported in the next quarter.

Figure 1 shows the effect of pre-implanting helium at 600°C or 750°C vs simultaneously implanting it at the same temperature on carbide precipitation in 20% cold worked 316 SS. The time-temperature-precipitation (TTP) diagram was constructed from data published by Weiss and Stickler[1] and Spitznagel and Stickler[2] on 316 stainless steels similar to the reference MFE heat. No complete TTP diagram has been determined for the reference steel at this time however, and the figure is meant to be schematic. Maziasz[3] has used a similar approach in comparing long time thermal aging effects out of reactor and irradiation effects in the HFIR reactor.

The micrographs are arranged in pairs in Figure 1. Each pair refers to a time-temperature combination on the TTP diagram indicated by the "X's". For each combination the micrograph on the left is for an unirradiated thermal control specimen. The micrograph on the right is for an ion bombarded target exposed for the same time-temperature combination as the thermal control but under a damage rate of $\sim 1 \times 10^{-4}$ dpa.s^{-1}. The short exposure specimens were subjected to co-impinging beams of

helium and silicon. The long exposure samples had the helium pre-implanted at 600°C or 750°C. The damage level in all of the bombarded specimens was ~5 dpa and the helium concentration ~60 appm. Intragranular carbide precipitation in the thermal control samples occurred through the often observed "random-dot" nucleation and growth sequence described by Lewis and Hattersley[4]. The only evidence for precipitation of a second phase in the irradiated material was the formation of Widmannstaten precipitates in the specimen helium pre-implanted at 750°C and then bombarded at the same temperature (upper right micrograph). The Widmannstaten structure is similar to an early stage of $M_{23}C_6$ carbide precipitation observed by Singhal and Martin[5] in a 24% Ni 25% Cr stainless steel. It is not a form of the carbide usually observed in 18-8 or 18-12 austenitic stainless steels. (These rod-shaped precipitates were too small and few in number to permit identification with electron diffraction analysis or chemical extraction techniques and hence their exact nature is not known at this time). The data suggest that the effect of either pre-implanting or simultaneously implanting the helium is to retard the nucleation and growth of intragranular carbides in this 316 SS. Precipitation of $M_{23}C_6$ carbides on the grain boundaries, however, was not affected by ion bombardment. The results are consistent with the idea that vacancies trapped by the helium are unavailable to assist in carbide nucleation and growth. The effects of helium concentration and "time-at-temperature" will have to be explored more fully to understand the occurrence of the rod-shaped precipitates in the helium pre-implanted specimen but not in the simultaneously implanted target.

"Time-at-temperature" effects such as precipitation and recrystallization must be carefully considered if pre-implantation of helium at elevated temperature is to be a viable approach for obtaining reference microstructures for mechanical properties testing in low nickel alloys through mixed spectrum or fast neutron irradiation. Recovery and recrystallization were also observed to depend on the mode of helium injection for the 20% cold rolled 316 SS, Figure 2. Cavity sizes are very different

in the two grains separated by the carbide-decorated boundary as a result of partial recrystallization in the specimen pre-implanted with helium at 750°C and subsequently bombarded to ~5 dpa at the same temperature. No recrystal1ization (but some recovery) was observed in the companion target bombarded with co-impinging beams of He + Si at 750°C. It is likely that the additional 7-1/2 h at temperature required for the helium pre-injection was sufficient to trigger the recrystallization. Experiments involving shorter pre-implantation times and thermal annealing of control samples are in progress to study the influence of helium implantation rate and time-at-temperature on the microstructural stability of this alloy.

It is possible that at these low fluences and low helium levels, the helium per se exerts little influence on the stability of the cold-worked microstructure. Few cavities were observed at grain boundaries even in the partially recrystallized specimens. In addition, the pre-existing dislocation cell walls were not the dominant cavity nucleation sites as anticipated, Figure 3. Most of the cavities appeared in the cell interiors and were associated with the Widmannstaten precipitates. This can be seen more clearly in Figure 4. The swelling associated with these cavities is approximately 0.2% at a fluence of ~6 dpa and a helium level of ~60 appm. There is no evidence, as yet, that this heterogeneous cavity formation results in a bimodal swelling vs temperature curve as has been observed in the 316 SS used in the Advanced Cladding Program (LMFBR technology)(6).

Figure 5 shows the effect of varying the helium implantation mode on cavity formation in the cold-worked 316 SS. Pre-implanting the helium at elevated temperature invariably produced much larger maximum cavity sizes. No cavities were visible in the cold-worked specimens at these fluences for irradiation temperatures of 600°C or lower. Cavities were observed at lower temperatures, however, in the solution annealed material, Figure 6. Again the effect of "hot" pre-implantation was to increase the maximum cavity size. However, for the annealed material there was a background of very small cavities in the pre-implanted

specimens as indicated by the frequency-size distribution curve. Simultaneous implantation produced' a much more uniform distribution of cavity sizes suggesting a continuous process of nucleatfon and growth. It appears that selective growth of certain cavity embryos occurs in the pre-implanted specimens. The large cavities are usually associated with the Widmannstaten precipitates.

Finally it has been observed that the helium injection mode has a strong influence on the nature of the dislocations but not on total dislocation density under the conditions of these experiments. Figure 7 indicates the observed trend. Pre-implantation results in fewer dislocation loops after bombardment relative to specimens simultaneously doped with helium during the production of atomic displacement damage. The results are consistent with theoretical calculations which suggest that helium atoms decorating the periphery of a dislocation loop will repel self-interstitial atoms and so inhibit loop growth[7].

The initial results offer little encouragement that pre-implantation of helium in low nickel alloys followed by mixed spectrum or fast reactor irradiation will produce "equivalent" microstructures and mechanical properties compared to specimens in which the helium is continuously produced during irradiation. However, higher fluence data over a range of damage rates are required.

B. Design of a Residual Gas Analyzer System Compatible with Dual-Ion Beam Bombardment Requirements

Some refractory metals which appear to have useful characteristics for fusion applications unfortunately act as "getters" at operating temperatures of interest. Any radiation damage study on such materials has to take this into account. In selecting reactive/refractory metals for various fusion reactor applications, it will be important to know and understand the impact of the vacuum conditions on the microstructural changes resulting from ion bombardment at elevated temperatures.

One can approach this problem by settling for nothing but ultra-high vacuum ($<10^{-9}$ torr) around the bombarded samples. At the present time this would present severe problems for doing dual beam experiments in our facility. A compromise approach is to settle for a vacuum of about 10^{-7} torr and attempt to measure the species of atoms and molecules near the bombarded surface. In fact, we believe that at this stage the latter scheme is a much more practical and fruitful one to pursue. Consequently a high resolution residual gas analysis system is being designed and constructed for use with the dual ion irradiation system at the HEIBS Facility.

Recently the quadropole mass spectrometer (OMS), turbo pumps, and electronics have been delivered by Extranuclear Laboratories, Inc. Tests run at Extranuclear show that the QMS operates well within specifications. After our next set of implantation experiments we plan to install a new dual-beam sample chamber, a new furnace arrangement, and two turbo-pumps which will permit high resolution residual gas analyses at the reactive/refractory metal target during dual-ion irradiation.

VI. REFERENCES

1. B. Weiss and R. Stickler, Met. Trans., 3, p. 851 (1972).
2. J. Spitznagel and R. Stickler, Met. Trans., 5, p. 1363 (1974).
3. P. J. Maziasz, in "Alloy Development for Irradiation Performance Quarterly Progress Report for Period Ending March 31, 1978", Oak Ridge National Laboratory.
4. M. H. Lewis and B. Hattersley, Acta Met., 13, p. 1159 (1965).
5. L. K. Singhal and J. W. Martin, Acta Met., 16, p. 1159 (1968).
6. A. F. Rowcliffe, "Nickel Ion Irradiation of Neutron Irradiated SA 316 - Some Aspects of the Unified Simulation Program" presented at the Workshop on the Use of Dual-Ion Beams in Basic Radiation Effects Research, Oak Ridge National Laboratory, May 11 (1978).

7. M. I. Baskes and W. D. Wilson, J. Nucl. Mater. 63, p. 126 (1976)

VII. FUTURE WORK

Computer analysis of the microstructural data will be conducted to further compare the effects of helium implantation mode on nucleation and growth processes. TEM observations and measurements will be made on 316 SS targets bombarded at higher appm He/dpa ratios and higher fluences The high resolution residual gas analyzer system will be assembled.

VIII. PUBLICATIONS

None

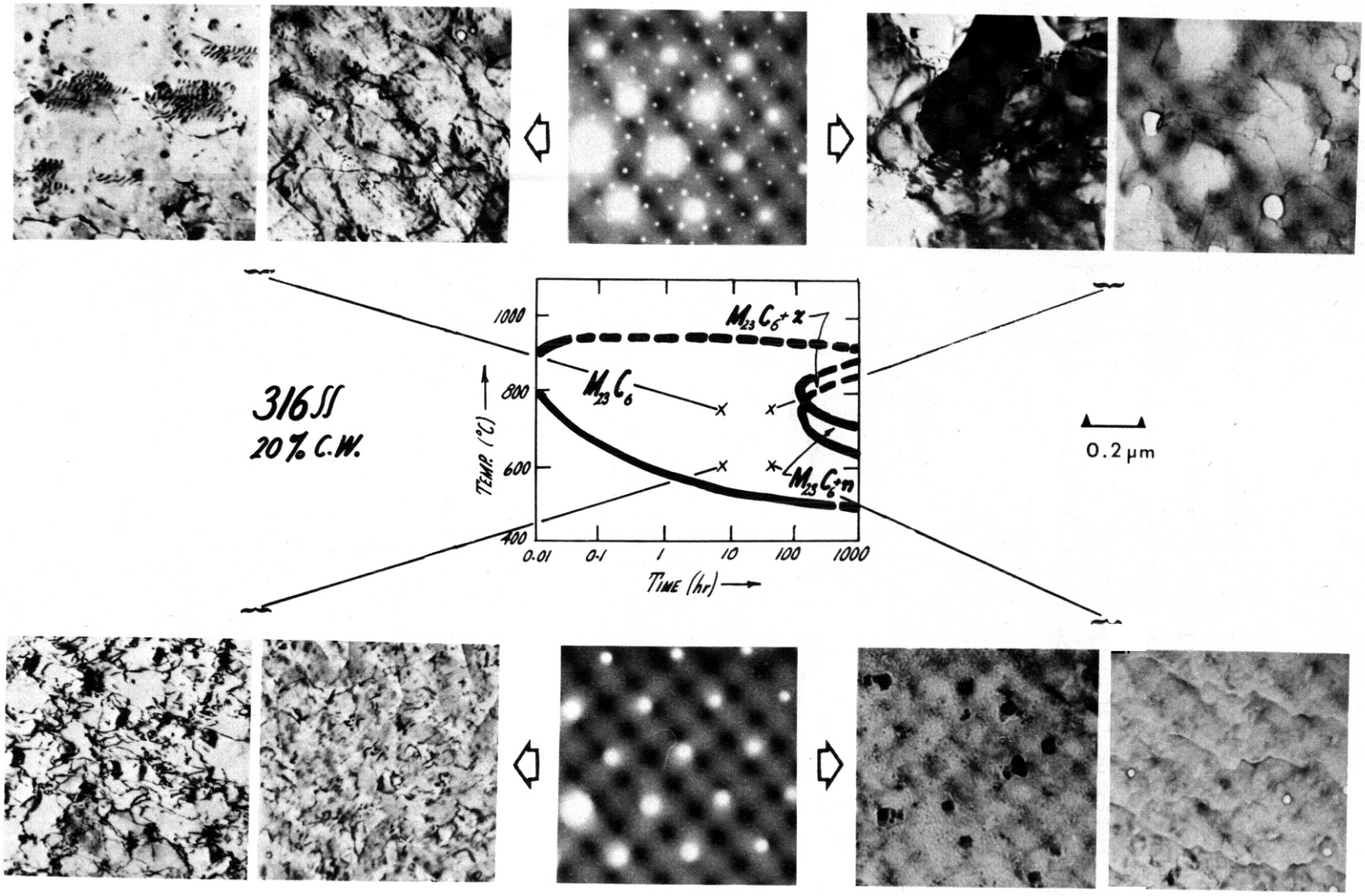

FIGURE 1 The Effect of Time, Temperature and Mode of Helium Implantation on Carbide ($M_{23}C_6$) Precipitation in 20% Cold-Rolled 316 SS. In Each Pair of Micrographs the Thermal Control is on the Left; the Ion Bombarded Specimen is on the Right. For the Short Exposures (9 hours) Helium was Simultaneously Implanted During Bombardment. For the Longer Exposures (18 hours) Helium was First Pre-Implanted at 600°C or 750°C.

FIGURE 2. Changes in Cavity Size and Density Across a Grain Boundary as a Result of Partial Recrystallization. (20% CW 316 SS, Pre-injected with Helium at 750°C and Subsequently Bombarded with Silicon Ions at 750°C.)

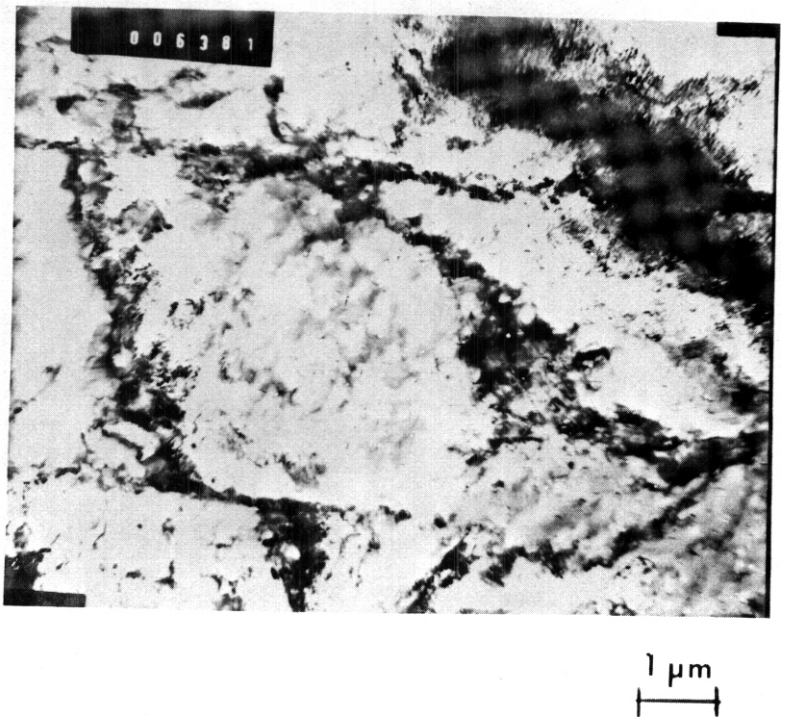

FIGURE 3. **Cavities Appear Mostly in Cell Interiors, Not Associated with Cell Wall Dislocation Tangles.** (20%CW 316 SS, Pre-injected with Helium at 750°C and Subsequently Bombarded with Silicon Ions at 750°C.)

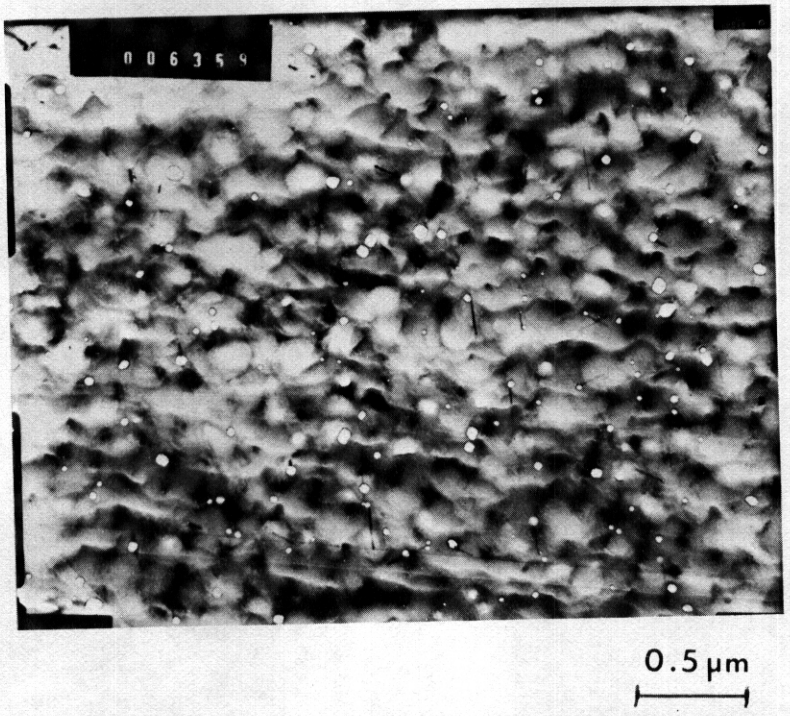

FIGURE 4. Heterogeneous Cavity Formation on Rod-Shaped Precipitates in Grain Interiors. (20% CW 316 SS, Simultaneously Implanted with Helium and Silicon Ions at 750°C.)

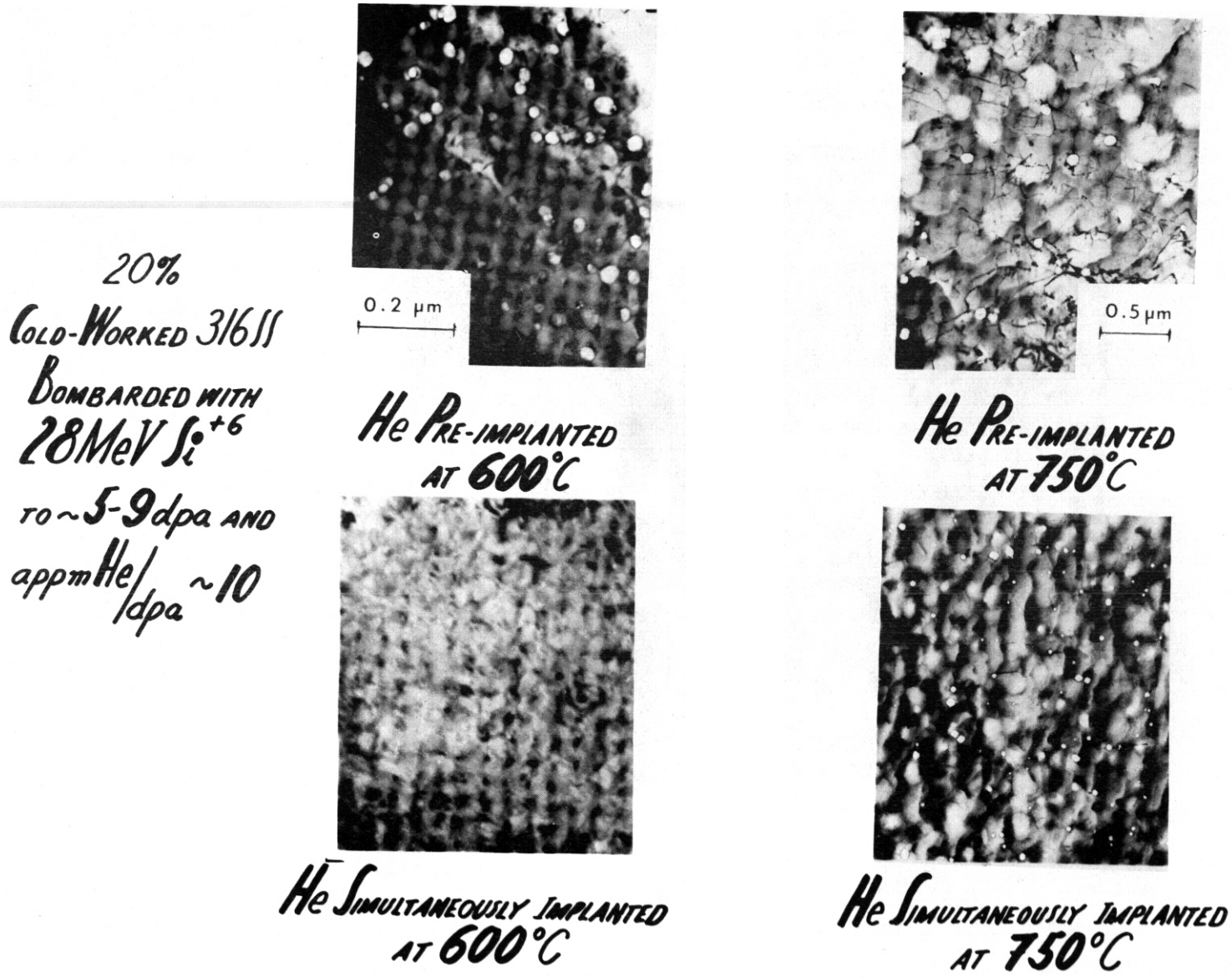

FIGURE 5. Effects of the Mode of Helium Implantation on Cavity Formation in 20% Cold-Worked 316 SS

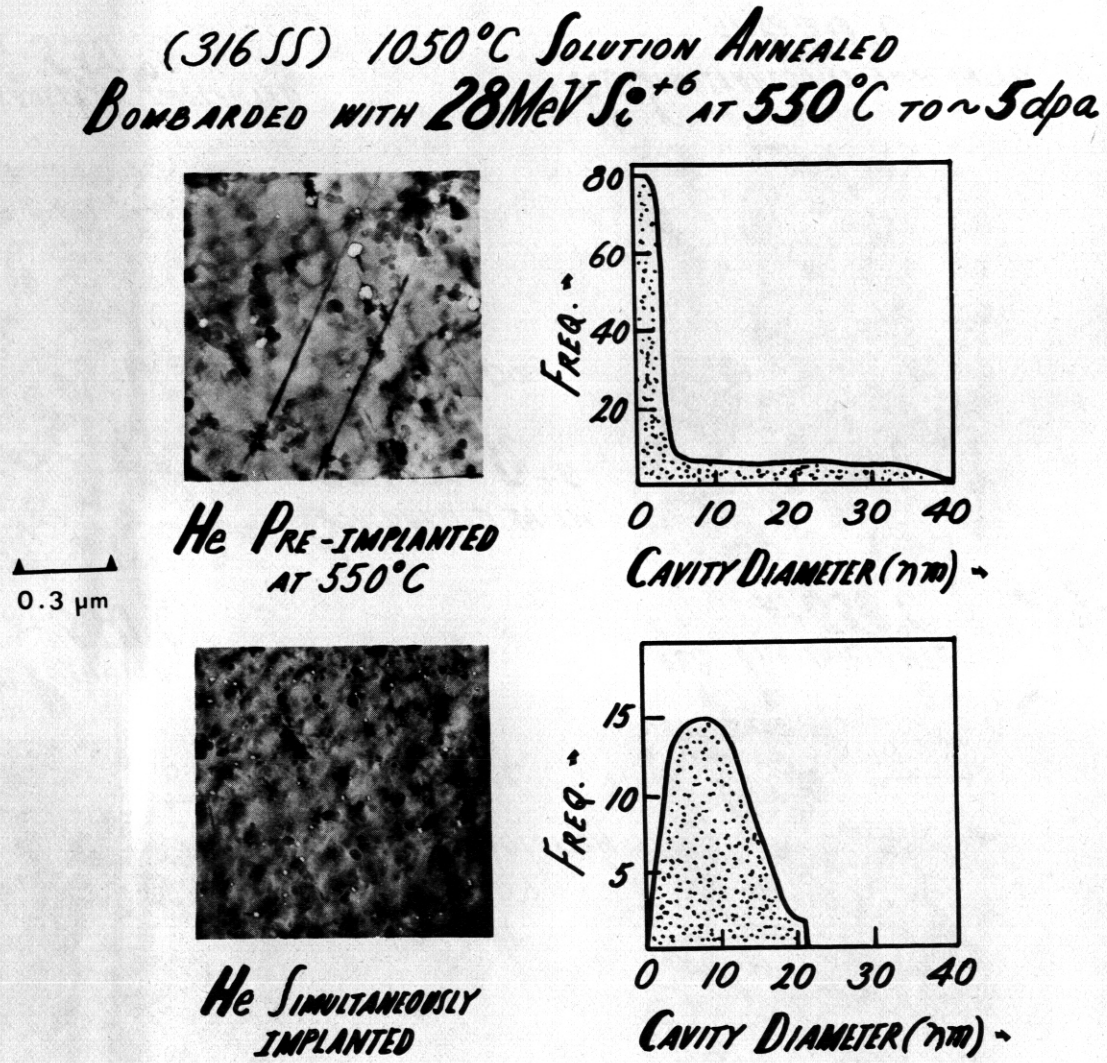

Figure 6. Effects of the Mode of Helium Implantation on Cavity Formation in Solution Annealed 316 SS.

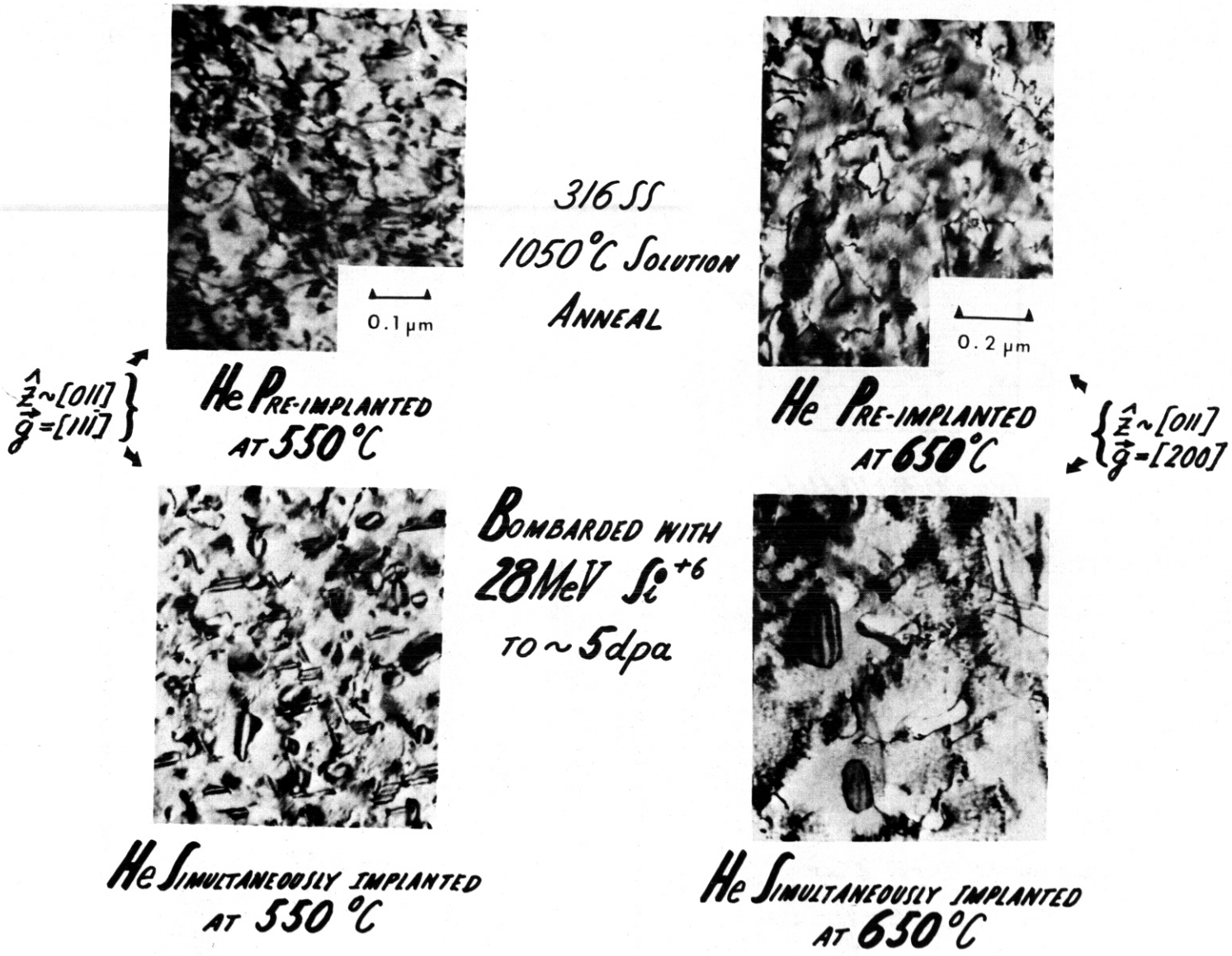

FIGURE 7 Effects of the Mode of Helium Implantation on Interstitial Dislocation Loop Formation in Solution Annealed 316 SS.

DISTRIBUTION FOR DAFS QUARTERLY REPORTS

UC-20 (117)
UC-20c (78)
APPROVED SPECIAL DISTRIBUTION (82)

Argonne National Laboratory (5)
9700 South Cass Avenue
Argonne, Illinois 60439

L. R. Greenwood
S. O. Harkness
V. H. Maroni
F. V. Nolfi, Jr.
H. Wiedersich

Atomics International (1)
Component Engineering and Technology Division
North American Rockwell
8900 DeSoto Avenue
Canoga Park, California 91304

H. Farrar, IV

Battelle-Northwest (5)
P. O. Box 999
Richland, Washington 99352

J. L. Brimhall
A. B. Johnson
R. H. Jones
L. C. Schmid
D. Styris

Brookhaven National Laboratory (2)
Associated Universities
Upton, New York 11973

Chairman, Department of Nuclear Energy
A. N. Goland

DISTRIBUTION (cont'd.)

Department of Energy
Washington, D.C. 20545

Office of Fusion Energy (6)
J. F. Clarke, ETM
F. E. Coffman, ETM
N. A. Davies, ETM
J. F. Decker, ETM
E. E. Kintner, ETM
M. Roberts, ETM

Materials and Radiation Effects Branch, ETM (25)

Assistant Director for Materials Technology, RRT (2)
J. W. Bennett
P. B. Hemmig

General Atomic Company (3)
P. O. Box 81608
San Diego, California 92138

G. R. Hopkins
S. Rosenwasser
L. Rovner

Lawrence Livermore Laboratory (2)
University of California
P. O. Box 808
Livermore, California 94550

M. W. Guinan
C. M. Logan

Los Alamos Scientific Laboratory (3)
University of California
P. O. Box-1663
Los Alamos, New Mexico 87544

D. 3. Dudziak
W. Green
D. M. Parkin

DISTRIBUTION (cont'd)

Massachusetts Institute of Technology (2)
Cambridge, Massachusetts 02139

O. K. Harling
K. C. Russell

McDonnell-Douglas Astronautics (2)
P. O. Box 516
St. Louis, Missouri 63166

J. Davis
D. Kummer

Mound Laboratory (1)
P. O. Box 32
Miamisburg, Ohio 45342

Manager, Technology Applications and Development

Naval Research Laboratory (3)
Metallurgy Division, Code 6390
Washington, D. C. 20375

I. Manning
F. A. Smidt
J. A. Sprague

North Carolina State University (1)
Department of Nuclear Engineering
Raleigh, North Carolina 26707

J. R. Beeler, Jr.

Oak Ridge National Laboratory (6)
P. O. Box Y
Oak Ridge, Tennessee 37830

Director, Thermonuclear Division, Bldg. 9201-2
L. A. Berry
R. J. Colchin, Bldg. 9201-2
F. G. Perey
C. Weisbin

DISTRIBUTION (cont'd)

Plasma Physics Laboratory (3)
Princeton University
P. O. Box 451
Princeton, New Jersey 08540

C. Osgood
W. Price
K. Wakefield

Sandia Laboratories (2)
Albuquerque, New Mexico 87115

F. L. Vook

Sandia Laboratories (3)
Livermore, California 94550

W. Bauer (2)
W. Wilson

University of Michigan (1)
Nuclear Engineering Department
College of-Engineering
Ann Arbor, Michigan 48105

T. Kammash

Westinghouse Electric Corporation (3)
Research and Development Center
Beulah Road
Pittsburgh, Pennsylvania 15234

J. Choyka
H. R. Holland
J. A. Spetznagel

*U.S. GOVERNMENT PRINTING OFFICE : 1979 0-281-704/41